UNIVERSITÄT PADERBORN

Microscopic investigation of light induced harmonic generation: Ultrafast carrier dynamics and excitonic effects

Dissertation

zur
Erlangung des Doktorgrades
der Naturwissenschaften
(Dr. rer. nat.)

der

Naturwissenschaftlichen Fakultät
der Universität Paderborn
vorgelegt von

Ruixin Zuo

Paderborn, 2025

Erklärung der Selbstständigkeit

Hiermit versichere ich, die vorliegende Arbeit selbstständig verfasst und keine anderen als die angegebenen Quellen und Hilfsmittel benutzt sowie die Zitate deutlich kenntlich gemacht zu haben.

Ort, Datum	Unterschrift

Vorsitzender der Prüfungskommission:	Prof. Dr. Thomas Zentgraf
Erstgutachter:	Prof. Dr. Torsten Meier
Zweitgutachter:	Prof. Dr. Jan Sperling
Vertreterin des Mittelbaus:	Dr. Adriana Bocchini
Datum der Abgabe:	28. Januar 2025

Zusammenfassung

In dieser Arbeit haben wir die Erzeugung von hohen Harmonischen in photoangeregten Halbleitermaterialien theoretisch und numerisch untersucht. Zunächst untersuchen wir die nicht-ströungs theoretiche Erzeugung hoher Harmonischen in Volumen-Materialien auf der Grundlage einer quantenmechanischen Theorie und eines semiklassischen Dreistufenmodells. Wir schlagen einen Mechanismus der Kollision mit benachbarten Atomen vor, der möglichist, wenn sich die Wellenlänge der Elektronen der atomaren Größe nähert. Dies führt zu dem einzigartigen Phänomen der orientierungsabhängigen Emission hoher Harmonischer in Festkörpern. Die Kollisionsdynamik steht in engem Zusammenhang mit den Van-Hove-Singularitäten oder kritischen Linien in der Bandstruktur, die Art der Streuung bestimmen. Darüber hinaus entwickeln wir ein Quanten-Trajektorienmodell, in dem die Quantendynamik der Tunnel-Ionisation durch die klassisch verbotene Coulomb-Potentialbarriere berücksichtigt wird, um die Erzeugung hoher Harmonischer in Festkörpern zu analysieren. Wir zeigen, dass die Eigenschaften von Elektronen und Löchern nach dem Tunneln, die mit dem Grad der Adiabatizität des Tunnelns zusammenhängen, mit Hilfe der Hochharmonischen Interferometrie hoher Harmonischer untersucht werden können. Schließlich analysieren wir exzitonische Effekte, bei der Erzeugung der dritten Harmonischen in einem zweidimensionalen Material im Rahmen eines Störungsansatzes. Die Nichtlinearitäten höherer Ordnung, die Übergänge zwischen dem Kontinuum und den gebundenen Exziton-Zuständen beschreiben, sind für die Bestimmung der Effizienz der Erzeugung der dritten Harmonischen bei erhöhter optischer Anregungs-intensität relevant.

Summary

In this thesis, we theoretically and numerically studied harmonic generation in photoexcited semiconductor materials. First, we investigate nonperturbative high harmonic generation from bulk materials based on a quantum mechanical theory and a semiclassical three-step model. We propose a mechanism of the collision with neighboring atoms when the wavelength of electrons approaches atomic sizes which leads to the unique phenomenon of orientation-dependent high harmonic emission from solids. The collision dynamics is closely related to Van Hove singularities or critical lines in the band structure which determine the type of scattering upon collision. In addition, we develop a quantum trajectory model in which the quantum dynamics of tunneling ionization through the classically forbidden Coulomb potential barrier is taken into account for analyzing high harmonic generation in solids. We demonstrate that the properties of electrons and holes at the tunnel exit which are associated with the degree of adiabaticity of the tunneling can be probed via high harmonic interferometry. Finally, we investigate excitonic effects in third harmonic generation from a two-dimensional material by a perturbative approach. Higher-order nonlinearities representing transitions between the continuum and bound exciton states are relevant for determining the efficiency of the third harmonic generation for elevated optical field intensities.

List of Abbreviations

SBE	**s**emiconductor **B**loch **e**quations
TDSE	**t**ime-**d**ependent **S**chrödinger **e**quation
TDDFT	**t**ime-**d**ependent **d**ensity-**f**unctional **t**heory
BSE	**B**ethe-**S**alpeter **e**quation
HHG	**h**igh **h**armonic **g**eneration
EUV	**e**xtreme **u**ltra**v**iolet
TMDC	**t**ransition **m**etal **d**ichal**c**ogenides
SHG	**s**econd **h**armonic **g**eneration
THG	**t**hird **h**armonic **g**eneration
DFT	**d**ensity **f**unctional **t**heory
BZ	**B**rillouin **z**one
PT	**p**arallel **t**ransport
TPT	**t**wisted **p**arallel **t**ransport
FWHM	**f**ull **w**idth at **h**alf **m**aximum
SVD	**s**ingle-**v**alue **d**ecomposition
CB	**c**onduction **b**and
VB	**v**alence **b**and
2D	**t**wo-**d**imensional

List of scientific contributions

Doctorate-related publications

Peer-reviewed publications

- **Ruixin Zuo**, Alexander Trautmann, Guifang Wang, Wolf-Rüdiger Hannes, Shidong Yang, Xiaohong Song, Torsten Meier, Marcelo Ciappina, Thanh Duc Huynh, and Weifeng Yang, Neighboring atom collisions in solid-state high harmonic generation, Ultrafast Science **2021**, 9861923 (2021).
- **Ruixin Zuo**, Xiaohong Song, Shuai Ben, Torsten Meier, and Weifeng Yang, Revealing the nonadiabatic tunneling dynamics in solid-state high harmonic generation, Physical Review Research **5**, L022040 (2023).
- Shidong Yang, Xiwang Liu, Hongdan Zhang, Xiaohong Song, **Ruixin Zuo**, Torsten Meier, and Weifeng Yang, Sub-cycle strong-field tunneling dynamics in solids, Optics Express **32**, 15862-15869 (2024).

Book chapters

- Hongdan Zhang, **Ruixin Zuo**, Shidong Yang, Alexander Trautmann, Xiaohong Song, Torsten Meier and Weifeng Yang, Analyzing High-Order Harmonic Generation in Solids Based on Semi-Classical Recollision Models, in *High-Order Harmonic Generation in Solids*, (World Scientific, Singapore, 2024), pp. 112-138.
- Matthias Reichelt, **Ruixin Zuo**, Xiaohong Song, Weifeng Yang and Torsten Meier, Sub-cycle strong-field tunneling dynamics in solids, in *High-Order Harmonic Generation in Solids* (World Scientific, Singapore, 2024), pp. 225–242.

Conference Proceedings

- Alexander Trautmann, **Ruixin Zuo**, Guifang Wang, Wolf-Rüdiger Hannes, Shidong Yang, Le Huu Thong, Cong Ngo, Johannes Tilman Steiner, Marcelo Ciappina, Matthias Reichelt, Huynh Thanh Duc, Xiaohong Song, Weifeng Yang, and Torsten Meier, Microscopic simulations of high harmonic generation from semiconductors, Proc. SPIE **11999**, 1199909 (2022).

Conference Presentations

- **Ruixin Zuo**, Xiaohong Song, Shuai Ben, Weieng Yang, and Torsten Meier, Characterizing the nonadiabatic tunneling dynamics in solid-state high harmonic generation, Talk at DPG Spring Meeting (SKM) in Dresden (2023).
- **Ruixin Zuo**, Xiaohong Song, Shuai Ben, Weieng Yang, and Torsten Meier, Revealing nonadiabatic tunneling dynamics in solid-state high harmonic generations, Poster presented at the International Summer School on Extreme Nonlinear Optics in Solids in Cork, Ireland (2023).

My contributions

I started my research work on analyzing the nonlinear optical and electronic response of semiconductors by solving the semiconductor Bloch equations (SBE) under the joint supervision of Prof. Dr. Torsten Meier and Prof. Dr. Xiaohong Song (Hainan University, China) in China before moving to Paderborn University in April 2022. Hence, some parts of the results presented in Chapters 3 and 4 were obtained when I was a member of the research group of Prof. Dr. Xiaohong Song. All studies presented in the scope of this thesis are based on frequent and fruitful discussions with my supervisor Prof. Dr. Torsten Meier, my former supervisor Prof. Dr. Xiaohong Song, and my research colleagues. For all results presented in this thesis, I was the main developer of the program codes for numerically solving the SBE and establishing the semiclassical electron-hole trajectory model. I performed the simulations, analyzed the generated data, and obtained physical interpretations. For the results presented in Chapter 3, I performed the numerical simulations of the high harmonic generation in MgO and analyzed the underlying real-space trajectory dynamics using the semiclassical recollision model in collaboration with Dr. Alexander Trautmann and Guifang Wang. For the results presented in Chapter 4, I performed the numerical simulations of the real-time high harmonic emission in ZnO and implemented a complex saddle-point model for analyzing the tunneling dynamics. For the results presented in Chapter 5, I performed the theoretical and numerical calculations of the excitonic third harmonic generation partly in collaboration with Cong Thanh NgO and Dr. Matthias Reichelt. I significantly contributed to obtaining the physical interpretation of the in-plane static field influence on the nonlinear excitonic response.

Contents

Introduction 1

Nonlinear optics is concerned with the analysis and understanding of nonlinear phenomena and the exploration of applications arising from the interactions between high-intensity light and materials [1]. Nonlinear optical phenomena have laid the foundation for a variety of important areas, such as laser technology [2, 3], spectroscopy development [4, 5], and material structure analysis [6–8]. The interaction results in the generation of optical fields at new frequencies, including optical harmonics of the incident light field or sum- or difference-frequency signals. The field of nonlinear optics started with the generation of second-order [9] and third-order [10, 11] harmonics in the context of perturbative nonlinear optics, shortly after the invention of the ruby laser in 1960 [12]. With the advent of ultrashort high-intensity lasers such as mode-locked Ti-doped sapphire (Ti: sapphire) lasers, the regime of extreme nonlinear optics [13] has emerged in which nonperturbative processes are relevant. The frequency of the generated light can be extended to that extreme ultraviolet (EUV) and the hard X-ray range via high harmonic generation (HHG) [14].

One of the most interesting nonlinear optical phenomena is the upconversion of laser light to radiation at multiples of the laser frequency, i.e., harmonic generation. Thanks to the advancement of laser technology [15], the extreme nonlinear optical response of HHG has been observed by illuminating matter with high-power laser fields. HHG was first identified in rare gases [16, 17] irradiated by near-infrared pulses. The emission spectrum is composed of three regions: a linear decline from the first order to higher ones, a plateau, and an abrupt high-energy cutoff. The plateau region in the HHG spectrum forms the basis for creating attosecond ($10^{-18}s$) light bursts in the form of isolated pulses or trains of pulses [18], as celebrated by the 2023 Nobel Prize in Physics [15]. Hence, the area of attosecond science has emerged seeking to generate ultrashort pulses with ultrabroad bandwidth and advancing the applications of attosecond pulses in the fields of nano-, bio-, magnetic-, molecular-, and materials science and technology [18–20]. The physical process underlying HHG from gases can be understood by a three-step recollision picture in the strong-field approximation [21] which neglects the effects of the Coulomb potential on the liberated electrons: (i) an electron tunnels into the continuum (ionization), (ii) the electron is accelerated by the strong field (propagation), and (iii) the electron recombines with its parent ion and emits a high-energy photon (recombination) [21, 22]. The cut-off of the emitted HHG photon energy is explicitly given by $\hbar\omega_{cut-off} = I_p + 3.17U_p$ where I_p is the ionization potential of the gas atom and $U_p = e^2E_0^2\lambda^2/16\pi^2mc^2$ is the ponderomotive energy of a free electron in an intense field (that is, the average energy of an electron with mass m driven by an oscillating electric field of amplitude E_0 and wavelength λ) [21, 23].

Solid-state materials have emerged as a new stage of strong-field physics and attosecond

science. Since the first HHG experiment performed on a bulk crystal of ZnO using a strong mid-infrared laser pulse [24], solid-state HHG has attracted enormous attention. Up to date, using lasers with wavelengths ranging from near-infrared to terahertz (THz), HHG has been widely investigated in solid-state systems ranging from semiconductors [24–32] and dielectrics [30, 33, 34] to two-dimensional semiconductors [35, 36], metasurfaces [37], and nanostructured solids [38, 39]. Because of the higher electronic density, solid-state HHG is a promising tool for compact vacuum ultraviolet [40] and EUV attosecond sources [41]. Unlike in the atomic phase, solid-state HHG relies on the collective response from a periodic array of atoms, leading to interband transitions and coherent transport of charge carriers in their respective bands. Solid-state HHG is sensitive to the electronic band structure, topological properties, and many-body effects of the system [42–44]. Consequently, solid-state high harmonic spectroscopy facilitates a wide range of studies such as all-optical electronic band structure retrieval [45, 46], laser picoscopy of the valence electron structure [47], and probing topological properties of materials [48–50], etc.

Numerical simulations of solid-state HHG are largely based on the single-particle time-dependent Schrödinger equation (TDSE) [51, 52], time-dependent density-functional theory (TDDFT) [53, 54], and semiconductor Bloch equations (SBE) [55, 56]. Several physical mechanisms have been proposed to understand the microscopic dynamics underlying the solid-state HHG, e.g., coupled inter- and intraband dynamics [55], transitions between Wannier–Stark ladder states [57–60], semiclassical electron-hole recollision model [56], and quantum interference between interband transitions [46], etc. The semiclassical transport theory enables us to address the sub-cycle coherent electron-hole dynamics driven by an electric field and has successfully explained the main features of the HHG spectrum [28, 61]. Yet, identifying and characterizing the atomic effects that relate to the quantum process of tunneling ionization and may-body effects in solid-state HHG remains a fundamental challenge.

The optical absorption of layered transition metal dichalcogenides (TMDC) is dominated by tightly Coulomb-bound electron-hole pairs known as excitons. The linear absorption and harmonic generation processes, especially second- (SHG) and third-order (THG) harmonic generation, have been extensively investigated in two-dimensional (2D) TMDC and their stacked structures and show strong excitonic features [62–64]. SHG, as a spectroscopic tool to probe the parity of exciton states, was enhanced by several orders of magnitude when the two-photon laser is tuned in resonance with dark exciton states [63, 65–68]. In the strong-field regime, excitons could survive intense pulses and lead to a significant increase of high harmonic emission [35, 69–72]. Up to date, the role of the excitons played in nonlinear optical phenomena with strong fields has not been comprehensively understood.

This thesis is organized as follows:

In Chapter 2, we review theoretical descriptions of the interaction between classical light and semiconductors, theoretical modeling of HHG within the band theory of solids, and fundamental concepts of excitonic effects.

In Chapter 3, we explore the origin of the anisotropy of HHG from MgO based on a semiclassical trajectory analysis. We demonstrate that different types of collision and scattering with neighboring atoms lead to a field polarization-dependent HHG efficiency and reveal that the real-space collisions are closely linked to singularities in the band structure.

In Chapter 4, we investigate tunneling ionization in solid-state HHG and provide a transparent picture of intensity-dependent nonadiabatic and adiabatic tunneling processes. We show that the characters of electrons at the tunneling exit are important in precisely predicting features of the HHG spectrum.

In Chapter 5, we study the influence of excitonic effects on THG in bilayer TMDC under rather weak optical excitations. We discuss the impact of an in-plane static field, which induces hybridization of exciton states, Stark effect, and exciton ionization, on the THG efficiency. More importantly, we reveal that transitions between the continuum and the exciton states lead to an intensity-dependent THG which surprisingly can be significantly enhanced by the in-plane static field.

In Chapter 6, we give a summary of the results presented in this thesis.

Microscopic theoretical modeling of the light-matter interaction in semiconductors 2

In this chapter, we present an overview of the theoretical background for studying the harmonic generation that is investigated in Chapters 3-5. The SBE form the cornerstone for the microscopic theory of nonlinear optics in semiconductor systems, which systematically describe coherent light-matter coupling effects and the Coulomb-induced many-body interactions in semiconductors. Here, the derivation of the SBE starting from a general many-body Hamiltonian is presented. Since the SBE are formulated within the band theory of crystalline solids, the electronic band structure and wave functions which provide the dipole and Coulomb matrix elements are needed as input to the approach. The ground-state properties can be computed by various approaches, such as $k.p$ theory, tight-binding model, and density functional theory (DFT). For numerically obtained wave functions, proper gauge transformations for the dipole and Coulomb matrix elements are required for a correct numerical analysis. In the strong field regime, sometimes the Coulomb interaction among the photoexcited carriers can be neglected. The reduced SBE in a two-band model are applied in Chapters 3 and 4 for studies of strong-field phenomena of bulk materials. When it comes to layered materials, e.g. mono-/bilayer TMDC which feature a notable exciton binding energy, the optical response is dominated by excitonic effects, and therefore the SBE with Coulomb interaction on the Hartree-Fock level are applied in Chapter 5.

2.1 Many-body Hamiltonian

The Hamiltonian of an electron in a solid is the sum of the kinetic and the interaction energies. In semiconductor optics, the fermionic, second quantized many-body Hamiltonian within the Bloch representation reads

$$\hat{H} = \hat{H}_0 + \hat{H}_{l-m} + \hat{H}_C + \hat{H}_{rest}. \tag{2.1}$$

The first term $\hat{H}_0 = \sum_{\lambda,\mathbf{k}} \epsilon^{\lambda}_{\mathbf{k}} \hat{a}^{\dagger}_{\lambda,\mathbf{k}} \hat{a}_{\lambda,\mathbf{k}}$ describes the band structure where the operator $\hat{a}^{\dagger}_{\lambda,\mathbf{k}}$ ($\hat{a}_{\lambda,\mathbf{k}}$) creates (annihilates) an electron in band λ with crystal momentum $\hbar\mathbf{k}$. The energy of an electron in band λ is denoted as $\epsilon^{\lambda}_{\mathbf{k}}$. The corresponding Bloch state is given by

$\langle \mathbf{r}|\lambda\mathbf{k}\rangle = e^{i\mathbf{k}\cdot\mathbf{r}}u_{\lambda\mathbf{k}}(\mathbf{r})$ with a cell-periodic $u_{\lambda\mathbf{k}}(\mathbf{r})$ and fulfills orthonormality $\langle\lambda\mathbf{k}|\lambda'\mathbf{k}'\rangle = \delta_{\lambda\lambda'}\delta(\mathbf{k}-\mathbf{k}')$.

The second term $\hat{H}_{l-m}$ is the interaction between the system and an external field. In the electromagnetic length gauge, the light-matter interaction takes form $-|e|\mathbf{E}(t)\cdot\mathbf{r}$ within the dipole approximation, where e is the fundamental electron charge and $\mathbf{E}(t)$ is the applied electric field. The position operation in the Bloch basis reads

$$\langle\lambda\mathbf{k}|\hat{\mathbf{r}}|\lambda'\mathbf{k}'\rangle = \delta_{\mathbf{k}\mathbf{k}'}\left[i\delta_{\lambda\lambda'}\nabla_{\mathbf{k}} + \mathbf{d}_{\mathbf{k}}^{\lambda\lambda'}\right], \tag{2.2}$$

where $\mathbf{d}_{\mathbf{k}}^{\lambda\lambda'}$ is the dipole matrix element given by

$$\mathbf{d}_{\mathbf{k}}^{\lambda\lambda'} = i\langle u_{\lambda\mathbf{k}}|\nabla_{\mathbf{k}}|u_{\lambda'\mathbf{k}}\rangle. \tag{2.3}$$

The Berry connection is defined as the diagonal element

$$\vartheta_{\mathbf{k}}^{\lambda} = \mathbf{d}_{\mathbf{k}}^{\lambda\lambda}, \tag{2.4}$$

which is non-vanishing in non-inversion symmetric systems. The light-matter Hamiltonian has the explicit form

$$\hat{H}_{l-m} = -\mathbf{E}(t)\cdot\sum_{\lambda\lambda',\mathbf{k}}\mathbf{d}_{\mathbf{k}}^{\lambda,\lambda'}\hat{a}^{\dagger}_{\lambda,\mathbf{k}}\hat{a}_{\lambda',\mathbf{k}} + i|e|\mathbf{E}(t)\sum_{\lambda,\mathbf{k}}\hat{a}^{\dagger}_{\lambda,\mathbf{k}}\nabla_{\mathbf{k}}\hat{a}_{\lambda',\mathbf{k}}, \tag{2.5}$$

where the first term describes the coupling between bands λ and λ' by the field. The coupling strength is determined by the dipole matrix element $\mathbf{d}_{\mathbf{k}}^{\lambda\lambda'}$. The second term contains the gradient $\nabla_{\mathbf{k}}$ and describes intraband transitions of electrons. It leads to a time-dependent crystal momentum which changes in time according to the acceleration theorem

$$\frac{d}{dt}\mathbf{k}(t) = -\frac{e}{\hbar}\mathbf{E}(t). \tag{2.6}$$

The many-body part of the Hamiltonian $\hat{H}_C$ accounts for the Coulomb interaction among the photoexcited carriers

$$\hat{H}_C = \frac{1}{2}\sum_{\lambda,\lambda',\mu,\mu'}\sum_{\mathbf{k},\mathbf{k}'}\sum_{\mathbf{q}\neq 0}V^{\lambda\mu\mu'\lambda'}_{\mathbf{q},\mathbf{k}',\mathbf{k}}\hat{a}^{\dagger}_{\lambda,\mathbf{k}-\mathbf{q}}\hat{a}^{\dagger}_{\lambda',\mathbf{k}'+\mathbf{q}}\hat{a}_{\lambda',\mathbf{k}'}\hat{a}_{\lambda,\mathbf{k}}. \tag{2.7}$$

The Coulomb matrix element in the Bloch representation has the form

$$V^{\lambda\mu\mu'\lambda'}_{\mathbf{q},\mathbf{k}',\mathbf{k}} = V_{\mathbf{q}}\langle\lambda\mathbf{k}-\mathbf{q}|\lambda'\mathbf{k}\rangle\langle\mu\mathbf{k}'+\mathbf{q}|\mu'\mathbf{k}'\rangle, \tag{2.8}$$

where $V_{\mathbf{q}}$ is the Coulomb interaction potential including the effect of the dielectric environment which is the Fourier transform of the real-space Coulomb potential. $\hat{H}_{rest}$ contains all other interactions including, e.g., the coupling to lattice vibrations (phonons) and other scattering effects [73, 74]. Throughout this thesis, the rest contributions are effectively modeled by phenomenological parameters.

2.2 Semiconductor Bloch equations

The microscopic polarization $p_{\lambda\lambda'}(\mathbf{k},t) = \langle a^{\dagger}_{\lambda,\mathbf{k}}(t)a_{\lambda',\mathbf{k}}(t)\rangle$ $(\lambda \neq \lambda')$ and the carrier density $n_{\lambda}(\mathbf{k},t) = \langle a^{\dagger}_{\lambda,\mathbf{k}}(t)a_{\lambda,\mathbf{k}}(t)\rangle$ determine the electromagnetic response of the semiconductor. The dynamical evolution of these quantities is obtained by evaluating Heisenberg's equation of motion of the operators involved. For a general operator $\hat{O}$ in Heisenberg's representation, the equation of motion of its expectation value is

$$i\hbar\frac{\partial}{\partial t}\langle\hat{O}\rangle = \langle\hat{O},\hat{H}\rangle. \tag{2.9}$$

Using the many-body Hamiltonian defined in Equations (2.1), (2.5), and (2.7) and explicitly evaluating the commutator on the right-hand side of Equation (2. 9), we obtain equations of motion for all operators $\hat{O}$ involved in $p_{\lambda\lambda'}(\mathbf{k},t)$ and $n_{\lambda}(\mathbf{k},t)$. The equations contain the coupling of single-particle expectation values (singlets) with two-particle expectation values (doublets) and so on, which is known as the many-body hierarchy problem. The coupling of singlets to doublets accounts for the Coulomb correlation effects and can be treated by methods such as the cluster expansion or coherent dynamics-controlled truncation scheme [73, 75], which is beyond the scope of the thesis. Here, a systematical hierarchy truncation, i.e., factorizing the four-operator terms into products of two-operator terms, which is known as the Hartree-Fock approximation, is applied. We neglect terms that change the number of electrons in a band. Thus, here Coulomb attractive interaction between electrons and holes, Coulomb repulsive interaction between particles of identical charges are taken into account. The closed set of differential equations that describe dynamics of the microscopic quantities $p_{\lambda\lambda'}(\mathbf{k},t)$ and $n_{\lambda}(\mathbf{k},t)$, i.e., multiband SBE reads

$$\begin{aligned} i\hbar\frac{\partial}{\partial t}p_{\lambda\lambda'}(\mathbf{k},t) &= [\varepsilon_{\lambda}(\mathbf{k}) - \varepsilon_{\lambda'}(\mathbf{k}) + i|e|\mathbf{E}(t)\cdot\nabla_{\mathbf{k}} + \vartheta^{\lambda\lambda'}_{\mathbf{k}}\cdot\mathbf{E}(t)]p_{\lambda\lambda'}(\mathbf{k},t) \\ &\quad - \Omega_{\lambda\lambda'}(\mathbf{k},t)(1 - n_{\lambda}(\mathbf{k},t) - n_{\lambda'}(\mathbf{k},t)) + \\ &\quad \sum_{\mu\neq\lambda,\lambda'}[\Omega_{\lambda\mu}(\mathbf{k},t)p_{\mu\lambda'}(\mathbf{k},t) - \Omega_{\mu\lambda'}(\mathbf{k},t)p_{\lambda\mu}(\mathbf{k},t)] + \Gamma^{\lambda\lambda'}_{\mathbf{k}} \end{aligned} \tag{2.10}$$

$$\hbar\frac{\partial}{\partial t}n_{\lambda}(\mathbf{k},t) = 2Im[\sum_{\nu\neq\lambda}\Omega_{\nu\lambda}(\mathbf{k},t)p_{\lambda\nu}(\mathbf{k},t)] + |e|\mathbf{E}(t)\cdot\nabla_{\mathbf{k}}n_{\lambda}(\mathbf{k},t) + \Gamma^{\lambda}_{\mathbf{k}} \tag{2.11}$$

Here

$$\varepsilon_\lambda(\mathbf{k},t) = \epsilon_\lambda(\mathbf{k}) - \sum_{\lambda',\mathbf{k}'} V^{\lambda\lambda'\lambda'\lambda}_{\mathbf{k}-\mathbf{k}',\mathbf{k},\mathbf{k}'} n_{\lambda'}(\mathbf{k}',t) \tag{2.12}$$

is the Coulomb renormalized energy of band λ and

$$\Omega_{\lambda,\lambda'}(\mathbf{k},t) = \mathbf{E}(t)\cdot\mathbf{d}^{\lambda\lambda'}_{\mathbf{k}} + \sum_{\mu,\mu',\mathbf{k}'} V^{\lambda\mu\mu'\lambda'}_{\mathbf{k}-\mathbf{k}',\mathbf{k},\mathbf{k}'} p_{\mu\mu'}(\mathbf{k}',t) \tag{2.13}$$

is the generalized Rabi frequency that couples bands λ and λ'. $\Gamma^{\lambda\lambda'}_{\mathbf{k}}$ and $\Gamma^{\lambda}_{\mathbf{k}}$ account for the dephasing of optical transitions and the relaxation of carrier densities, respectively, which arise, e.g., from scattering processes due to carrier-carrier Coulomb or carrier-phonon interaction. The terms proportional to $\mathbf{E}(t)\cdot\mathbf{d}^{\lambda\lambda'}_{\mathbf{k}}$ represent optical interband transitions. The intraband excitations are described by the terms proportional to $\mathbf{E}(t)\cdot\nabla_{\mathbf{k}}$ which lead to the acceleration of carriers in their bands. The Berry connection resembles the vector potential in reciprocal space which is an intrinsic geometric property arising from a broken inversion symmetry of the system [76]. It leads to a shift of the wave-packet center and therefore imposes an additional phase onto the polarization [77, 78].

The optical response of a coherently excited semiconductor consists of macroscopic polarization $\mathbf{P}(t)$ due to interband transitions,

$$\mathbf{P}(t) = \sum_{\lambda,\lambda',\mathbf{k}} \mathbf{d}^{\lambda\lambda'}_{\mathbf{k}} p_{\lambda\lambda'}(\mathbf{k},t) \tag{2.14}$$

and a macroscopic change current $\mathbf{J}(t)$ due to the intraband acceleration

$$\mathbf{J}(t) = \sum_{\lambda,\mathbf{k}} \mathbf{v}^{\lambda}_{\mathbf{k}} n_\lambda(\mathbf{k},t), \tag{2.15}$$

with the group velocity $\mathbf{v}^{\lambda}_{\mathbf{k}} = \frac{|e|}{\hbar}\nabla_{\mathbf{k}}\varepsilon_\lambda$.

2.3 Gauge smoothing of matrix elements

When solving the SBE in the length gauge, all quantities in the equations are required to be derivable with respect to $\mathbf{k}$ due to the presence of the $\mathbf{k}$ derivatives. When computing dipole and Coulomb matrix elements with eigenfunctions of the field-free Hamiltonian generated numerically on a discrete mesh grid of $\mathbf{k}$ space from $k.p$ theory or DFT approach, their phases are arbitrary, which makes it problematic to solve the SBE. Such a numerical obstacle is circumvented in the velocity gauge of the SBE in which the interaction with the field in Hamiltonian takes the form $\hat{\mathbf{v}}\cdot\mathbf{A}(t)$ where $\hat{\mathbf{v}}$ is the velocity operator and $\mathbf{A}(t) = -\int_{-\infty}^{t}\mathbf{E}(t')dt'$ is the vector potential of the applied field [77, 79]. In the velocity gauge of the SBE, the quantities at all discrete $\mathbf{k}$ points are not coupled and therefore the matrix elements carrying arbitrary phases would not cause mathematical instability.

However, more bands are needed for numerical convergence [77, 80]. In addition, the dephasing and population decay due to many-body effects are included in the velocity gauge by invoking the transformation between the velocity and the length gauges based on the unitary operator $Q = e^{ie\mathbf{A}\cdot\mathbf{r}/\hbar}$ [80, 81], which increases the computational complexity.

To solve the phase discontinuity problem described above, the construction of a smooth and periodic gauge for the Bloch functions is needed. It has shown that the SBE are gauge invariant, i.e. the resulting macroscopic polarization and occupations are not changed under the gauge transformation of the Bloch functions [77, 78, 80, 82, 83]. In Chapter 5 the band structure of bilayer MoS_2 is calculated using DFT. Due to the symmetry, all bands are spin-degenerate everywhere in $\mathbf{k}$ space and the corresponding eigenfunctions not only carry random phases at each $\mathbf{k}$ point, but the degenerate states are mixed. It is beyond the capability of the single-band gauge transformation method [77] to smoothen eigenfunctions in this situation. Below, we summarize the procedure of the gauge transformation [80, 84], i.e., multiband parallel transport (PT) gauge, which is able to treat general cases.

The idea of the PT gauge originates from Schrödinger perturbation theory [79]. The expansion of a Bloch function to the first order in $\Delta\mathbf{k}$ is

$$|u_{\lambda\mathbf{k}+\Delta\mathbf{k}}\rangle = \sum_{\nu}(e^{-i\Delta\mathbf{k}\cdot\vartheta(\mathbf{k})})_{\nu\lambda} \times [|u_{\nu\mathbf{k}}\rangle - i\sum_{\mu}|u_{\mu\mathbf{k}}\rangle\xi_{\mu\nu}(\mathbf{k})\cdot\Delta\mathbf{k}], \tag{2.16}$$

where the factor $e^{-i\Delta\mathbf{k}\cdot\vartheta(\mathbf{k})}$ is an arbitrary $\mathbf{k}$-dependent phase factor that is introduced to maintain the single-valuedness of the eigenfunctions and $\xi_{\mu\nu}$ is the off-diagonal dipole matrix element. Using the orthonormality of eigenfunctions, one has

$$(e^{-i\Delta\mathbf{k}\cdot\vartheta(\mathbf{k})})_{\nu\mu} = S_{\nu\mu}(\mathbf{k}, \mathbf{k}+\Delta\mathbf{k}), \tag{2.17}$$

where $S_{\nu\mu}(\mathbf{k}, \mathbf{k}+\Delta\mathbf{k}) = \langle u_{\nu\mathbf{k}}|u_{\mu\mathbf{k}+\Delta\mathbf{k}}\rangle$ is the overlap matrix element that is constructed in the subspace of states that are energetically closed at the $\mathbf{k}$ point, i.e., degenerate or connected. The matrix $S(\mathbf{k}, \mathbf{k}+\Delta\mathbf{k})$ is nearly unitary when the $\Delta\mathbf{k}$ is small. To guarantee the exact unitarity of the transformation, a single-value decomposition (SVD) is performed, $S(\mathbf{k}, \mathbf{k}+\Delta\mathbf{k}) = U(\mathbf{k})\sum(\mathbf{k})V^{\dagger}(\mathbf{k})$ to find the unitary operator $Q(\mathbf{k}, \mathbf{k}+\Delta\mathbf{k}) = U(\mathbf{k})V^{\dagger}(\mathbf{k})$. Applying the inverse of the unitary operator to the eigenfunctions,

$$|\tilde{u}_{\lambda\mathbf{k}+\Delta\mathbf{k}}\rangle = \sum_{\mu} Q^{-1}_{\lambda\mu}(\mathbf{k}, \mathbf{k}+\Delta\mathbf{k})|u_{\mu\mathbf{k}+\Delta\mathbf{k}}\rangle, \tag{2.18}$$

the optimal alignment of eigenfunctions at the neighboring $\mathbf{k}$-point (locally smooth gauge) is achieved. This smoothing gauge is known as the PT gauge. The Berry connection $\vartheta(\mathbf{k})$ is gauge-variant and it vanishes in the smoothed Bloch basis. The smoothing gauge can alternatively be constructed by the method of maximally localized Wannier functions [85], which is mathematically equivalent to the PT gauge [80, 82].

Performing the PT gauge transformation along the **k**-path, which is usually a closed loop around the Brillouin zone (BZ), would leave a mismatch in the Bloch functions when the **k**-path wraps from the ending point back to the starting point. In the multi-band formula, the overlap matrix of the eigenfunctions at the first and last **k** points has nonzero values on the diagonal elements. This is similar to the Berry phase in the single-band approximation. In addition, the off-diagonal elements of the overlap matrix involve the mixture of states for degenerate and connected bands. The periodicity of the Bloch functions requires removing this mismatch, otherwise the time-dependent intraband dynamics would suffer a sudden jump at the boundary of the BZ. The smoothing of the eigenfunctions at the boundary of the BZ can be achieved by the twisted parallel transport (TPT) gauge [82]. The overlap matrix constructed between the first and the last points of the **k**-path

$$W_{\lambda\mu} = \langle \tilde{u}_{\lambda \mathbf{k}_N} | u_{\mu \mathbf{k}_0} \rangle \tag{2.19}$$

is the Berry phase matrix. The SVD is applied so that $W = U \sum V^\dagger$ and one gets a unitary matrix $Q = UV^\dagger$. By diagonalizing Q

$$PQP^\dagger = diag(e^{i\phi_{\lambda_1}}, e^{i\phi_{\lambda_2}}, e^{i\phi_{\lambda_3}}, ...), \tag{2.20}$$

one gets the Berry phases of each separate state $\phi_{\lambda_1},\ \phi_{\lambda_2},\ \phi_{\lambda_3}, ...$ All locally smoothed eigenfunctions need to be unitarily transformed and acquire an evenly distributed phase

$$|\bar{u}_{\lambda \mathbf{k}}\rangle = e^{-i\phi_\lambda |\mathbf{k}|/|BZ|} \sum_\mu P^{-1}_{\lambda\mu} |\tilde{u}_{\mu \mathbf{k}}\rangle. \tag{2.21}$$

In a realistic implementation for bulk materials, one needs to perform the TPT gauge transformation with **k**-paths spanning the entire BZ in directions of the orthogonal lattice vector basis to ensure that the resulting eigenfunctions are smooth and periodic everywhere. Then the dipole and Coulomb matrix elements in the new Bloch basis are derivable in the three-dimensional **k** space. An alternative approach of implementing the smooth gauge in combination with the procedure of solving the SBE is provided in Ref. [84]. It demonstrates that the TPT gauge transformation can be applied to the variable $p(\mathbf{k}, t)$, instead of eigenfunctions, at each time step only along the direction of the field polarization. By doing so, the phase discontinuity in $p(\mathbf{k}, t)$ arising from the dipole and Coulomb matrix elements is eliminated which ensures the derivability of $p(\mathbf{k}, t)$ with respect to **k**. This is easier to implement but dramatically increases the computing time.

2.4 Solid-state high harmonic generation

HHG is a nonperturbative process that is induced by strong-intensity laser pulses. The solid-state HHG relies on the collective response from densely arranged atoms, leading to

coupled interband transitions and coherent intraband transport. As illustrated in Figure 2.1, the valence bands are initially occupied with electrons and the conduction bands are empty. An electric field of a frequency much lower than the bandgap non-resonantly drives interband transitions that promote electrons from valence to conduction bands. Dipole-allowed intersubband transitions of charged carriers (electrons and holes) from lower to higher conduction/valence bands occur once an imbalance of the carrier occupation exists. The polarization builds up between electron-hole pairs in the valence and conduction bands. The incident field also induces coherent transport of charged carriers in their respective bands, leading to the generation of intraband currents. When the intraband acceleration drives the carriers to traverse the BZ, Bloch oscillation [25] or Zener tunneling [86] occurs, depending on whether the carriers remain in the same band or transit to a higher-lying band. Relying on the properties of the material and the laser parameters, inter- or intraband emissionS may dominate the HHG and characteristically determine the spectral features such as the width of the plateau and the scaling of the cut-off energy with the incident field.

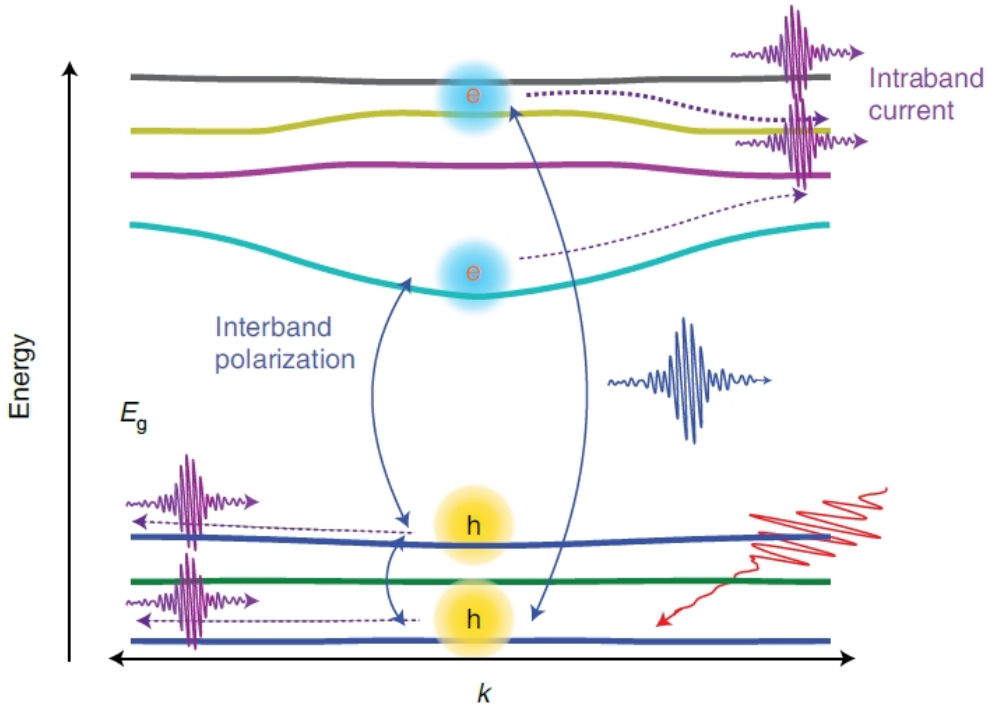

Figure 2.1: Schematic of the microscopic dynamics of the light-solid interaction in a multi-band representation. The interband transition creates electrons (e) in conduction bands with holes (h) left in valence bands, giving rise to the polarization (blue arrowed lines) The intraband currents are induced by the field driven motion of the electrons and the holes in their respective bands (purple dotted arrowed lines). The inter- and intraband dynamics are coupled to determine the high harmonic radiation. Adapted with permission from Ref. [43].

Due to the periodic structure of crystalline solids, a number of intriguing phenomena occur that are absent in atomic gases. In the first experiment of HHG on ZnO induced by an intense mid-infrared laser field, the cut-off energy was measured to scale linearly with the peak field amplitude, which is in contrast to the quadratic scaling law for atomic HHG [24]. As theoretically analyzed, the nonlinear intraband current that arises from Bloch oscillations contributes mainly to the radiation and thus the cut-off energy is proportional to the Bloch frequency $\omega_B = aE_0/\hbar$ and scales linearly with the field. For the intense THz field driven HHG process in GaSe, dynamical Bloch oscillations are identified as the origin which leads to a strong carrier envelope phase dependence of the HHG [25]. For those measurements of HHG dominated by interband polarization, the cut-off energy is limited to the maximum energy difference between bands. Multiple plateaus have been observed in HHG spectra which involve transitions to higher-lying bands [87–90]. Even harmonic generation in GaSe has been observed which is attributed to the multi-band quantum interference effects between interband transitions [46]. Also, a broken inversion symmetry of the crystal structure allows for the generation of even harmonics [27, 35, 48, 91]. The profound dependence on the orientation of the polarization of the field [92] and the ellipticity dependence of HHG have been observed in a variety of materials [36, 92, 93] which originates from the interplay between inter- and intraband effects [36]. It is the unique coherent intraband transport in solids associated with the real-space collision and scattering dynamics that lead to the sensitivity of HHG on the field polarization with respect to the crystal axes.

Solid-state high harmonic spectroscopy has enabled probing the properties of matter in exquisite detail, including probing the electronic structure of solids [45], interband Berry phases [50], intraband Berry curvature [35, 48], topological properties of materials [94], and imaging of valence electrons at the picometre scale [47]. In contrast to atomic HHG, solid-state HHG provides a novel path toward the generation of attosecond pulses as it has a lower prerequisite on the peak intensity of driving lasers and the generated EUV waveform is less affected by the fluctuations in the driving fields [14, 15, 95]. Moreover, the solid-state HHG efficiency can be largely enhanced and the cut-off energy could be remarkably extended by manipulating the high harmonic dynamics which is promising for generating stable pulses with the ultrabroad bandwidth of supercontinuum [96].

2.5 Excitonic effects in two-dimensional transition metal dichalcogenides

Excitons are composite bosons formed by Coulomb-bound electron-hole pairs [97], which have many features analogous to those of atomic hydrogen. Bound excitons give rise to sharp peaks in absorption and photoluminescence spectra and determine the optical properties in the spectral vicinity of the bandgap [62, 73, 97, 98]. The binding energy E_{bind}, defined as the energy difference between the lowest exciton resonance and the band gap (or I_p for atoms), ranges from a few to hundreds of millielectronvolts in semiconductor and

nanostructured materials [99]. This is small compared to the binding energy $E_{bind} = 13.6eV$ of the hydrogen atom due to the facts that the effective electron mass in semiconductors is substantially smaller than the free electron mass and the Coulomb interaction strength of semiconductors is roughly an order of magnitude less than in vacuum because of the background dielectric screening [97].

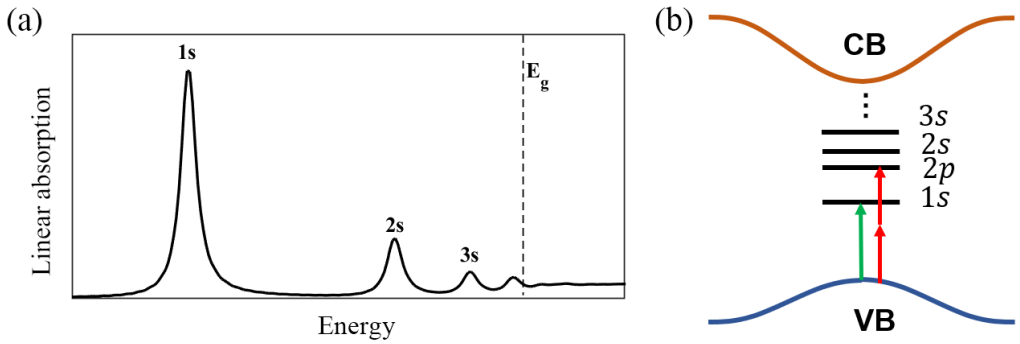

Figure 2.2: (a) Typical linear absorption spectrum of systems dominated by a series of bright excitons. (b) Schematic diagram of excitonic states in semiconductors. The one-photon dipole transition (green arrow) can only reach s exciton states with even parity whereas p exciton states with odd parity are one-photon inactive but can be accessed by two-photon absorption (red arrows). Due to the spatially dependent screening effects in semiconductors, the 2p exciton with a larger electron-hole separation has a weaker screening of Coulomb attraction and therefore features a lower energy level compared to the 2s exciton state.

The exciton envelope wave function describes the spatial separation of the electron and the hole. Due to the similarity with the hydrogen series, the exciton states in semiconductors are labeled with the orbital notation of Rydberg states (n, l), where n and l are the principal $(n = 1, 2, 3, ...)$ and the orbital angular momentum quantum numbers $(l = 0, 1, 2, ...)$, respectively. The radial node structures of exciton envelope wave functions are unique for each exciton state and a higher principal or a higher orbital quantum number indicates a larger average electron-hole separation. In particular, the principal quantum number n is the primary determinant of the binding energy of the respective state [99].

As shown in Figure 2.2(a), the typical linear optical absorption spectrum includes bright exciton transitions below the bandgap. Figure 2.2(b) schematically shows the optical selection rule of the transitions is determined by the symmetry of the exciton envelope wave functions and is physically equivalent to that of a Rydberg series. Specifically, s excitons are accessible by one-photon processes and forbidden in all processes involving an even number of photons. In contrast, p excitons are allowed in two-photon processes and forbidden in one-photon processes. In a hydrogen atom, orbitals with the same principal quantum number are degenerate. Because a relatively small exciton binding energy implies a large Bohr radius with a large spatial separation of electrons and holes, the exciton series in semiconductors is different from the hydrogen atoms. In semiconductors, the screening effect is weaker when the separation between the electron and hole is larger. Exciton

states with the same principle number but higher orbital quantum numbers have a larger average electron-hole separation, which leads to an enhanced Coulomb attraction and lower energy levels [100].

Experimental and theoretical studies have demonstrated that the electronic and excitonic properties are fundamentally modified when the materials are thinned down to atomic-scale thickness [98]. As illustrated in Figure 2.3, in contrast to bulk, the Coulomb interaction is significantly magnified in the monolayer due to the spatial confinement and reduced dielectric screening from the environment. Consequently, repulsive interaction between particles of identical charges leads to a self-energy contribution to the ground-state energy, which increases the quasiparticle band gap [99, 101]. In addition, enhanced attractive interaction increases the exciton binding energy [62, 99].

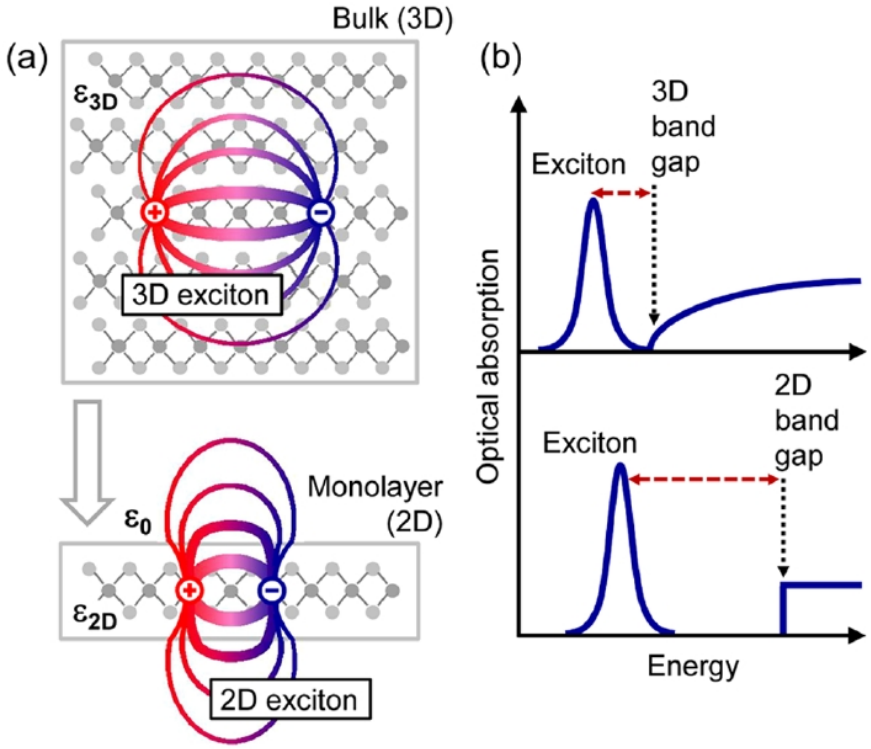

Figure 2.3: (a) An exciton formed by an excited electron and an excited hole with opposite charges, due to the Coulomb attraction between these two quasiparticles for a three-dimensional bulk and a quasi-two-dimensional monolayer. The dielectric environments are characterized by different dielectric constants ε_{3D} and ε_{2D} and by the vacuum permittivity ε_0. (b) Optical absorption spectra showing the influence of the reduced dimensionality. Compared to 3D bulk, both the quasiparticle band gap (black dashed arrows) and the exciton binding energy (red dashed arrows) are increased and the continuum edge appears as a step-like function for the quasi-2D monolayer. Other excitonic states above the lowest one with reduced spectral weights are not shown here. Reproduced with permission from Ref. [98].

TMDC semiconductors have recently emerged as an important class of two-dimensional semiconductors with potential for applications in electronic, optoelectronic, and nanophotonics [102, 103]. More interestingly, when thinned down to a monolayer, TMDC transform from indirect- to direct-bandgap semiconductors and feature strong spin-orbit coupling and valley degree of freedom, which lead to intriguing optical phenomena such as valley-selective circular dichroism [104, 105] and optical valley and spin Hall effects [106–108]. In layered TMDC, the spatial confinement and the reduced dielectric screening lead to exceptionally strong electron-hole Coulomb interaction. As determined by the experimental measurements such as one-photon absorption and two-photon excitation luminescence [63, 100], and theoretical predictions based on Bethe–Salpeter equation (BSE) and Wannnier equation [73, 98], the exciton binding energies of layered TMDC are on the order of hundreds of meV, which makes them robust enough to survive thermal fluctuations at room temperature [109–111]. Layered TMDC therefore form an excellent platform for fundamental studies of exciton physics.

Influence of collisions at neighboring atoms on solid-state high harmonic generation

3

HHG is an important nonlinear phenomenon in the strong field physics of atoms, molecules, and solids. The recombination upon the collision of an electron liberated by a strong electric field with its parent ion is the key step in the process of HHG [21, 22]. Compared to atoms and molecules, in solid-state HHG, the microscopic collision and scattering dynamics of an electron-hole pair before the recombination are much more complex due to the periodically arranged atoms in crystalline solids. The symmetry of the crystal structures governs physical and chemical processes. For example, the formation of a symmetric band structure results from time-reversal symmetry [112]. The selection rules of optical excitations are a direct consequence of the structural symmetries [48, 113–115]. Unlike atomic HHG, even harmonics can be generated from solids when the crystal structure is not inversion symmetric [35, 91]. Furthermore, solid-state HHG investigated over a variety of materials exhibits diverse field polarization and ellipticity dependences [26, 32, 36, 92, 93, 114, 116–118]. Intuitively, all these unique behaviors of HHG from solids are correlated with the constituents and arrangement of the atoms that form solids. High harmonic spectroscopy has thus developed which provides a powerful platform for studying the structure and dynamics of condensed matter all-optically [30, 45, 48, 116].

In this chapter, we theoretically and numerically investigate the orientation dependence of HHG from MgO [92] using an electron-hole recollision model. We show that the photoexcited electrons and holes may undergo head-on or side collisions with neighboring atoms and be elastically scattered when their wavelengths approach the length of the unit cell. Consequently, the recollision of the electron and the hole is facilitated or suppressed. Our findings link the electron/hole backward scattering with Van Hove singularities and forward scattering upon the collisions with critical lines in the band structure and thus establish a connection between the band structure and the HHG spectrum. The proposed mechanism of the collision with neighboring atoms offers a unifying picture for several experimental observations and theoretical predictions, including the anisotropic harmonic emission in MgO, the atomic-like recollision underlying the solid-state HHG, and the delocalization of HHG in ZnO. The results presented in this chapter were already published in Ref. [119].

3.1 The two-band semiconductor Bloch equations

HHG is a nonlinear and non-perturbative process, which requires high field strengths. When investigating the HHG process theoretically, the strong-field approximation is applied and in this chapter, the Coulomb interaction among photoexcited carriers is neglected. Thus, here we describe HHG in bulk materials by the SBE without Coulomb-reduced renormalization terms [25, 55, 56, 73]. For deriving the electron-hole recollision model from the SBE, it is advantageous to transform the equations into a time-dependent frame by introducing $\hbar\mathbf{k}(t) = \hbar\mathbf{k}_0 + e\mathbf{A}(t)$, in which $\mathbf{k}_0$ is the crystal momentum in the absence of an electric field and $\mathbf{A}(t) = -\int_{-\infty}^{t} dt'\mathbf{E}(t')$ is the vector potential. In the length gauge, the two-band SBE considering one conduction band and one valence band read

$$\begin{aligned}\frac{\partial}{\partial t}p(\mathbf{k}_0,t) = &-\frac{i}{\hbar}(\varepsilon_c(\mathbf{k}(t)) - \varepsilon_v(\mathbf{k}(t)))p(\mathbf{k}_0,t)) - \frac{1}{T_2}p(\mathbf{k}_0,t)\\ &+ \frac{i}{\hbar}\mathbf{E}(t)\cdot\mathbf{d}(\mathbf{k}(t))(n_v(\mathbf{k}_0,t) - n_c(\mathbf{k}_0,t)),\end{aligned} \tag{3.1}$$

$$\frac{\partial}{\partial t}n_\lambda(\mathbf{k}_0,t) = \frac{2}{\hbar}s_\lambda Im[\mathbf{E}(t)\cdot\mathbf{d}(\mathbf{k}(t))p(\mathbf{k}_0,t)]. \tag{3.2}$$

In these equations, $p(\mathbf{k}_0,t)$ is the microscopic polarization between the conduction and valence bands and $n_\lambda(\mathbf{k}_0,t)$ is the population of electrons in the conduction (valence) band for $\lambda = c(v)$. $s_\lambda = 1,-1$ for $\lambda = c,v$, respectively. Initially, the valence band is fully occupied and the conduction band is empty, i.e., $n_{v(c)}(\mathbf{k}_0, t = -\infty) = 1(0)$. The dephasing time T_2 describes the timescale on which the coherence decays, e.g., due to electron-phonon and electron-electron scattering processes. It is taken as a parameter that is usually assumed to be shorter than an optical cycle of the excitation field. The relaxation time for populations T_1 is neglected here since it is typically much longer than the dephasing time, i.e., $T_1 \gg T_2$. The field-induced dynamics of the polarization and the transport within bands lead to the generation of high harmonics via two sources, i.e., the interband polarization $\mathbf{P}(t)$ and the intraband current $\mathbf{J}(t)$.

$$\mathbf{P}(t) = \int_{BZ} d\mathbf{k}_0\mathbf{d}^*(\mathbf{k}_0 + \mathbf{A}(t))p(\mathbf{k}_0,t) + c.c., \tag{3.3}$$

$$\mathbf{J}(t) = \sum_{\lambda=c,v}\int_{BZ} d\mathbf{k}_0\mathbf{v}_\lambda(\mathbf{k}_0 + \mathbf{A}(t))n_\lambda(\mathbf{k}_0,t), \tag{3.4}$$

in which the integration of crystal momenta runs over the first BZ and $v_\lambda(\mathbf{k}) = \nabla_\mathbf{k}\varepsilon_\lambda(\mathbf{k})$ is the group velocity of band λ. The emitted electric field is proportional to $\mathbf{E}_{out}(t) =$

$\frac{\partial}{\partial t}\mathbf{P}(t) + \mathbf{J}(t)$. From the Fourier transform of $\mathbf{E}_{out}(t)$ we obtain the spectrum of the high harmonic emission

$$I_{out}(\omega) \propto |\omega\mathbf{P}(\omega) + \mathbf{J}(\omega)|^2. \tag{3.5}$$

3.2 The electron-hole recollision picture

For far off-resonant excitations, the electron population in the conduction band is rather low and one can assume $n_v(\mathbf{k}_0, t) - n_c(\mathbf{k}_0, t) \approx 1$. With this approximation, Equations (3.1) and (3.2) are decoupled so that $p(\mathbf{k}_0, t)$ and $n_\lambda(\mathbf{k}_0, t)$ can be formally integrated [56, 120]. For HHG spectra that are dominated by the interband contribution above the bandgap, it is sufficient to focus only on the spectrum of the integrated interband polarization:

$$\mathbf{P}(\omega) = \omega \int_{-\infty}^{\infty} dt e^{i\omega t} \int_{BZ} d\mathbf{k}_0 \underbrace{\mathbf{d}^*(\mathbf{k}_0 + \mathbf{A}(t))}_{Recombination} \int_{-\infty}^{t} dt' \underbrace{e^{-iS(\mathbf{k}_0,t,t') - \frac{t-t'}{T_2}}}_{Propagation} \underbrace{\mathbf{E}(t') \cdot \mathbf{d}(\mathbf{k}_0 + \mathbf{A}(t'))}_{Ionization} + c.c., \tag{3.6}$$

where

$$S(\mathbf{k}_0, t, t') = \frac{1}{\hbar} \int_{t'}^{t} d\tau \epsilon_g(\mathbf{k}_0 + \mathbf{A}(\tau)), \tag{3.7}$$

is the quasiclassical action with the energy difference $\epsilon_g(\mathbf{k}) = \epsilon_c(\mathbf{k}) - \epsilon_v(\mathbf{k})$. Physically, Equation (3.6), analogous to the "Lewenstein integral" for atomic HHG [121], can be interpreted as the coherent sum of contributions to the field-induced dipole. The term $\mathbf{E}(t') \cdot \mathbf{d}(\mathbf{k}_0 + \mathbf{A}(t'))$ is the probability amplitude of an electron excited to the conduction band at time t' with canonical crystal momentum $\mathbf{k}_0$. The wave function of the electron-hole pair is then propagated until time t and acquires a phase factor equal to $exp[-iS(\mathbf{k}_0, t, t') - \frac{t-t'}{T_2}]$, where $S(\mathbf{k}_0, t, t')$ is the quasiclassical action. The electron recombines with its associated hole at time t with an amplitude equal to $\mathbf{d}^*(\mathbf{k}_0 + \mathbf{A}(t))$. The properties of HHG rely on the probability of ionization, quantum interference of these electron-hole trajectories (time evolution of electron and hole wave packets), and the probability of recombination.

In strong field physics, the saddle-point approach is a powerful technique that not only provides semi-quantitative solutions but also offers intuitive physical insights into the three-step process that underlies HHG [21, 22, 122]. In Equation (3.6) the exponential term $exp(-i\phi)$ with the phase $\phi(\mathbf{k}_0, t, t') = S(\mathbf{k}_0, t, t') - \omega t + \frac{i(t-t')}{T_2}$ oscillates much faster than the electric field $\mathbf{E}(t')$. For highly oscillatory integrals, the major contribution comes from

stationary phase points (saddle points) where the first derivatives of the phase with respect to t', t, and $\mathbf{k}$ vanish. Thus, the saddle-point equations are given by

$$\frac{\partial}{\partial t'}\phi(\mathbf{k}_0, t, t') = \frac{1}{\hbar}\epsilon_g(\mathbf{k}_0 + \mathbf{A}(t')) - \frac{i}{T_2} = 0, \tag{3.8a}$$

$$\nabla_{\mathbf{k}}\phi(\mathbf{k}_0, t, t') = \frac{1}{\hbar}\int_{t'}^{t} d\tau \Delta\mathbf{v}(\mathbf{k}_0 + \mathbf{A}(\tau)) = \mathbf{0}, \tag{3.8b}$$

$$\frac{\partial}{\partial t}\phi(\mathbf{k}_0, t, t') = \frac{1}{\hbar}\epsilon_g(\mathbf{k}_0 + \mathbf{A}(t)) - \omega + \frac{i}{T_2} = 0, \tag{3.8c}$$

where $\Delta\mathbf{v}(\mathbf{k}) = \nabla_{\mathbf{k}}\epsilon_g(\mathbf{k}) = \mathbf{v}_c(\mathbf{k}) - \mathbf{v}_v(\mathbf{k})$ is the difference between the velocities of the electron and the hole in their respective bands. To simplify the analysis, we consider the limit $T_2 = \infty$ which does not alter the physical picture [61]. Analogous to atomic HHG, an electron-hole recollision model for HHG from solids is established based on Equations (3.8a-c). Since these three equations are coupled and $\epsilon_g(\mathbf{k}_0 + \mathbf{A}(t')) > E_g$ in Equation (3.8a), the exact solutions are complex-valued with imaginary parts related to the quantum mechanical nature of the ionization and recombination processes [123–125]. In such a model, an electron-hole pair is created near the band edge where the ionization probability is the highest. The laser field subsequently accelerates the electron and the hole within their respective bands, which governs the real-space trajectory. It should be noted that the electron-hole momentum-space trajectory cannot exactly define a real-space trajectory due to the quantum-mechanical uncertainty principle. Strictly, a full description of the real-space evolution requires taking crystal momenta in the full BZ into account. Here, the trajectory launched at only one particular crystal momentum point is considered from a classical perspective which traces the peak of the wave packet [120].

Equation (3.8a) describes the energy conversion during the interband transition which occurs at time t' and at $\mathbf{k}_0 + \mathbf{A}(t')$ in the momentum space. The promotion of an electron from the valence band to the conduction band (red arrowed line in Figure 3.1) is realized by multiphoton absorption or tunneling through the Coulomb potential barrier, i.e., the classically forbidden region. Subsequently, the electron and the hole are accelerated in their respective bands, respectively (green and magenta arrowed curves for electron and hole in Figure 3.1). The classical excursion of the electron (hole) in real space for any $\mathbf{k}_0$ is given by $\Delta\mathbf{r}_{c(v)}(\mathbf{k}_0) = \int_{t'}^{t} d\tau \mathbf{v}_{c(v)}(\mathbf{k}_0 + \mathbf{A}(\tau))$. In the atomic counterpart, the parent ion is unmoved and the electron is free once liberated with its kinetic energy described by a parabolic dispersion, $E = I_p + \frac{1}{2}m\mathbf{p}^2$ where m is the mass of electron and momentum $\mathbf{p}(t) \propto \mathbf{A}(t)$. Therefore the corresponding moving distance is $\Delta\mathbf{r}(t) = \int_{t'}^{t} d\tau \mathbf{A}(\tau)$. The difference between atoms and solids arises from the energy-momentum relation as the bands are formed by the quantum-mechanical electron's delocalization over the lattice of the crystal. Equation (3.8b), $\Delta\mathbf{r}_c(\mathbf{k}_0) - \Delta\mathbf{r}_v(\mathbf{k}_0) = \mathbf{0}$ means that the distances traveled by the electron and its associated hole are equal. Since the electron and hole are born at the same position, this equation implies that high harmonic radiation only occurs upon the electron-hole's reencounter. Eq. (3.8c) determines that the energy of the emitted harmonics

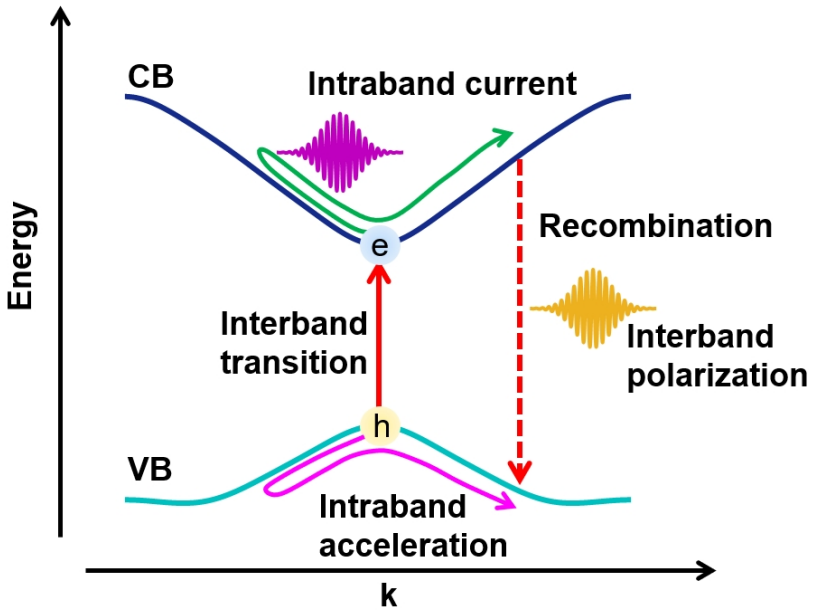

Figure 3.1: Schematical illustration of the three-step process of solid-state HHG in momentum space.

$\hbar\omega$ is equal to the interband transition energy at recombination time t and at the shifted crystal momentum $\mathbf{k}_0 + \mathbf{A}(t)$ (red dashed arrowed line in Figure 3.1). This electron-hole recollision model has revealed fundamental mechanisms of solid-state HHG [56].

A strict solution of the saddle-point equations would fully trace the electron dynamics in the classically forbidden and allowed regions. When beginning to investigate solid-state HHG based on the saddle-point analysis, the classical approximation was used which sets $E_g = 0$ when solving Eq. (3.8a), implying that the dynamics of the ionization process are discarded. Under this approximation, the electron and the hole are assumed to be created at the minimum of the transition energy with zero initial velocities and the real-space classical propagation starts with zero displacement between the electron and the hole. Thereby approximated real-valued solutions of the saddle point equations are obtained. In this chapter, we utilize the simplified saddle-point approach, in which the dynamics of the ionization process are ignored, to reveal the subcycle collision dynamics in the propagation step that is strongly related to the crystal structure. In the next chapter, the focus is put on the quantum mechanical aspects of the HHG process based on an improved semiclassical trajectory analysis.

3.3 Anisotropy of high harmonic generation from MgO

In contrast to atomic HHG which exhibits no dependence on the laser polarization direction and a monotonic decrease with the ellipticity degree of the incident field, solid-state HHG features rich orientation and ellipticity dependences that vary with the material. In this section, we focus on the anisotropy of HHG from inversion symmetric crystals [92]. As intuitively and generally understood, the orientation dependence of the emitted high harmonics is strongly related to the geometry of the crystal structure. To qualitatively describe this relation on a microscopic level, one needs to clarify: Can the electron recombine with the parent ion at nearby atomic sites when they meet, or does a collision with neighboring atoms scatter it away? Under what circumstances can such collisions occur and how do they affect the recombination of the electron and hole? In the following, we will theoretically investigate the anisotropic HHG emission by solving the SBE and analyze the underlying microscopic dynamics based on a semiclassical electron-hole recollision model.

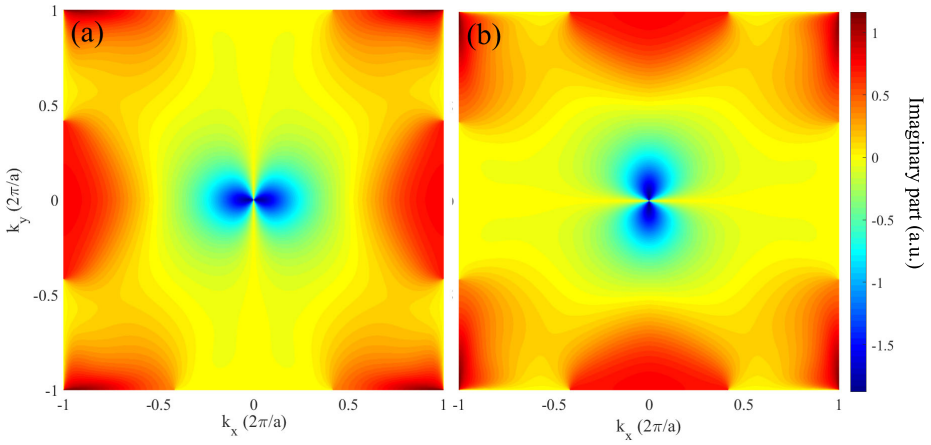

Figure 3.2: The imaginary part of (a) x component and (b) y component of the dipole matrix element shown in the first BZ for the transition from the valence to the conduction bands. The real part is nearly zero and not shown here. Taken from Ref. [119].

In the experiment that measured the angular distribution of the HHG yield from bulk MgO [92], the plane composed of magnesium (Mg) and oxygen (O) atoms is rotated with respect to a linearly polarized field with θ defined as the angle between the field polarization direction and the crystal axis of $\Gamma - X$ (Mg-O bonding). The electric field energy is 0.78 eV (corresponding to a wavelength of 1.3 μm) which is around 1/10 of the bandgap of the bulk MgO (7.8 eV). For the field amplitude 1 $V/\mathring{A}$, a clear four-fold symmetry for the HHG in the plateau region is observed. The angular distribution of the HHG exhibits sharp maxima for $\theta = 0°$, $90°$, $180°$, and $270°$ where the field is polarized along $\Gamma - X$ direction and second maxima for $\theta = 45°$, $135°$, $215°$, and $305°$ where the field is polarized along $\Gamma - L$ direction (Mg-Mg and O-O bondings). To explain the experimental observation, a simple real-space trajectory analysis is present in Ref. [92], in which the enhancement

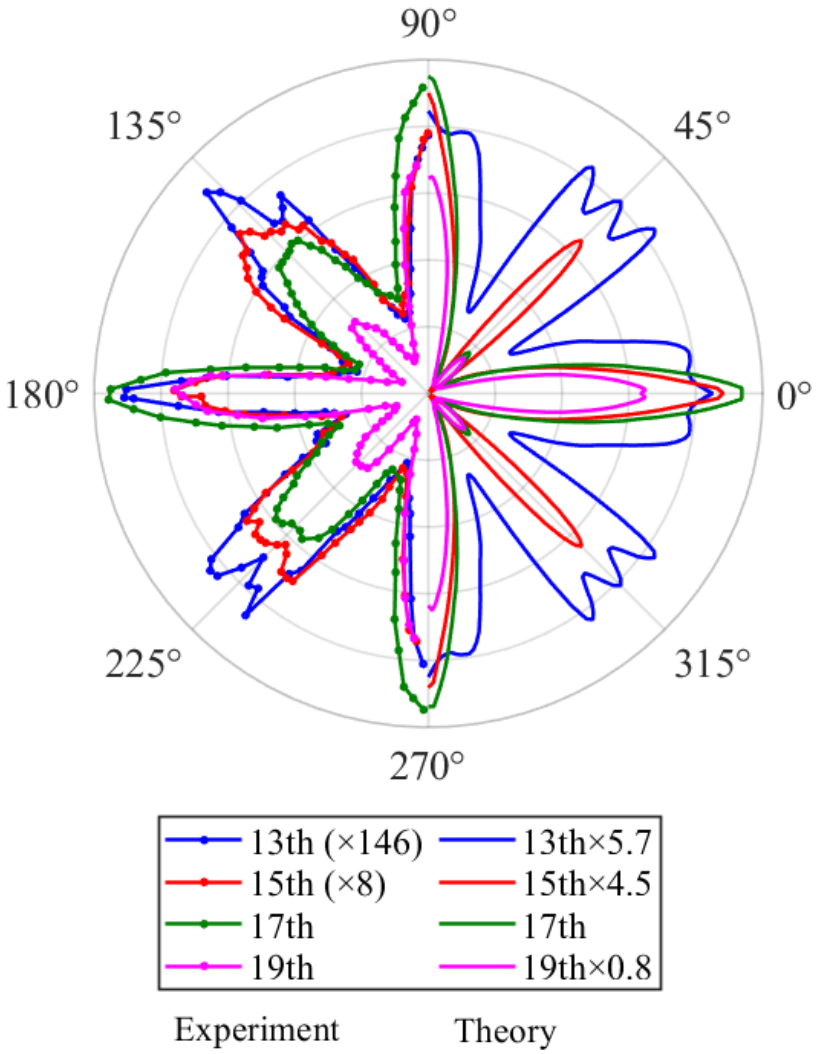

Figure 3.3: Orientation dependence of 13th-19th harmonics from MgO. Left: experimental results (curves with dots) which are reproduced with permission from Ref.[92]. Right: Results of SBE simulations (solid curves). Taken from Ref.[119].

(suppression) of HHG is attributed to the connection (disconnection) of electron trajectories with nearby atomic sites. The electron trajectory along $\Gamma - X$ direction experiences the largest electronegativity gradient between Mg^+ and O^- and therefore the probability of charge transfer is the highest. The electron trajectory along $\Gamma - L$ direction travels across atoms of the same type which reduces the probability of charge transfer and thus the radiation is relatively lower. When the electron trajectory does not cross nearby atoms, the radiation is the least probable. However, in this analysis, no closed electron-hole trajectory is displayed and how the charge transfer influences the classical motion and the recollision

is not explicitly shown.

Our work aims to further investigate the underlying mechanism of the orientation dependence of HHG based on a semiclassical electron-hole recollision model. Since the field is linearly polarized in the plane of (001)-cut of the MgO crystal in the experiment, electrons and holes are constrained to move in the plane [92]. Therefore, 2D calculations are sufficient to capture the main dynamics. We carry out the band structure calculation of MgO using a DFT package ELK [126]. The TPT gauge [77, 78, 80, 82, 83] is implemented for the eigenfunctions to ensure the smoothness of the phase of the dipole matrix element. MgO has an inversion symmetric crystal structure, therefore the Berry connection is zero and the phase of the dipole matrix element is 0 or $\pi/2$. The interband dipole moment is shown in Figure 3.2, which is imaginary-valued. We perform a quantum theoretical simulation of the orientation dependence of the HHG emitted from MgO by solving the SBE. In the simulation, the laser field frequency is the same as in the experiment and the full-width at half maximum (FWHM) of the temporal envelope of the pulse is ten optical cycles. The comparison of the $13th$, $15th$, $17th$, and $19th$ harmonics as functions of θ between the experiment data and our simulation results are shown in Figure 3.3. The main features that the HHG is maximum (second maximum) along $\Gamma - X$ ($\Gamma - L$) direction and sharply decreases away from these directions are reproduced. For harmonics above the band gap, the resulting interband polarization dominates over the intraband current by several orders of magnitude, which indicates that the recollision model is proper to analyze the obtained HHG spectra.

3.4 Scattering upon collision with atoms

To investigate the subcycle dynamics of HHG from MgO that underlies the orientation dependence, we consider an extremely short pulse consisting of nearly one optical cycle at 1.3 μm as is used in experiment [92]. Thus the excitation and emission dynamics are confined within a single optical cycle. Single-cycle pulses have been successfully synthesized in the terahertz, mid-infrared, visible, and EUV spectral ranges [127–129]. We choose three representative directions: $\theta = 0°$, $27°$, and $45°$, and the time-energy distributions of the interband polarizations covering almost the entire plateau energy region are shown in Figure 3.4. By calculating the interband polarization via the integral given by Equation (3.6), contributions from particular trajectories can be separated out. In Figure 3.4, the spectra obtained by solving the two-band SBE (color map in the left panel) and artificially extracting the contributions from the trajectories with interband transitions through the Γ point, i.e., $\mathbf{k}_0 + \mathbf{A}(t') = 0$ (color map in the right panel) are displayed for the three polarization directions. The temporal structures are basically the same in these two calculations, suggesting that the main contributions come from ionization near the band edge. The relative intensities of the spectra in these three directions are consistent with those measured in the experiment [92] as well as with the quantum simulations shown in Figure 3.3.

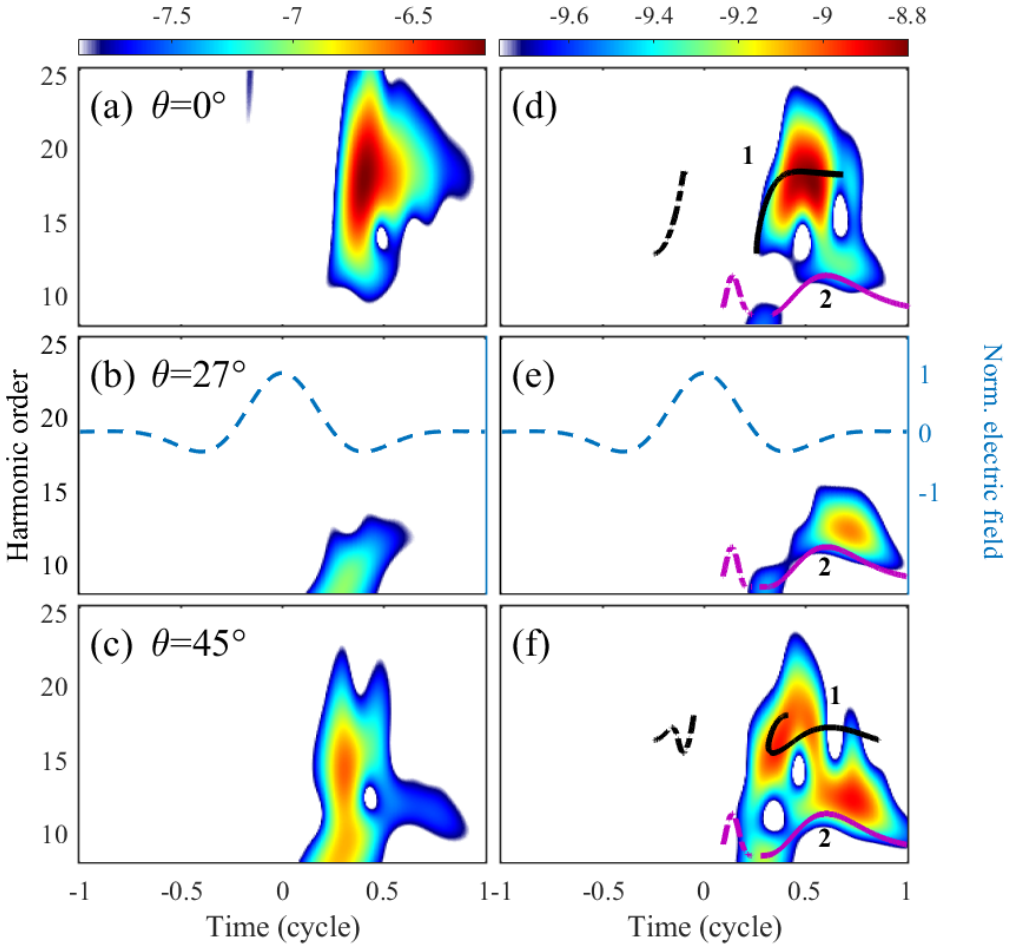

Figure 3.4: Comparison between the SBE Simulation and the classical trajectory analysis for HHG from MgO. (a–c) High harmonic spectra versus time obtained from solving the SBE. (d–f) Color maps: Spectra of high harmonics versus time computed with only contribution from interband transition at around the Γ point; Curves: emitted harmonic energies as a function of ionization (dashed curves) and recombination (solid curves) times predicted by the semiclassical model. All spectral intensities in the color maps are on a logarithmic scale. The waveform of the incident laser electric field is shown by the blue dashed curves in (b) and (e). Taken from Ref. [119].

We calculate the real-space electron and hole trajectories and obtain the harmonic energy as a function of both the ionization (dashed lines in Figures 3.4(d-f)) and the recombination (solid lines in Figures 3.4(d-f)) times. Here we consider an electron-hole pair created at the Γ point. The ionization time is scanned over a half cycle including before and after the crest of the field. A good agreement is achieved between the quantum results and the classical trajectory predictions of the emission time of HHG. This confirms the validity of the recollision model in which a high-energy photon is emitted when the electron recombines with its associate hole. The simple trajectory analysis presented in Ref. [92] is

based on the recombination of the electron with any arbitrary ion nearby which has no correspondence to the saddle-point equations Equations 3.8(a-c).

In Figure 3.4, the temporal structure of the emission is remarkably separated into two parts, corresponding to two sets of electron-hole recombination trajectories in the higher and lower energy regions, respectively. Both of them occur for the laser polarizations along $\theta = 0^\circ$ and $\theta = 45^\circ$, which are referred to as "1" and "2" in Figures 3.4(d) and (f). However, the trajectory set "1" disappears for $\theta = 27^\circ$ (see Figure 3.4(e)). As demonstrated by the classical analysis, the trajectory sets "1" and "2" are different in the ionization time, which is before and after the crest of the field, respectively. It has been noted that in atomic HHG, ionization before the crest of the field does not generate high harmonics [22]. On the contrary, electron-hole pairs created by such an ionization in solids can recombine to emit high harmonics.

To find out what leads to such a recombination associated with the trajectory set "1", an electron/hole trajectory for a laser polarization of $\theta = 0^\circ$ with the ionization instant $-0.13T_0$ is analyzed with its real-time evolution in the momentum space (see the magenta dashed arrowed lines in Figure 3.5 (a-b)) and real space (see Figures 3.5 (c)) shown in Figures 3.5. The corresponding real-time trajectory evolution can be found [130]. It is shown that the electron/hole in real space collides with an atom after passing through several unit cells. This collision leads to a backward scattering of the electron-hole pair and a reversion of the travel direction, as marked by "P1" and "P1'" in Figures 3.5 (a-c). This collision occurs at around $0.08T_0$ when the electric field's polarity has not yet changed, which implies that the direction reversion of the trajectory is not directly determined by the field as is the case in atoms. We find that this spatial collision happens when the momentum-space trajectory reaches the critical points where $\nabla_{\mathbf{k}} E_{c/v}(\mathbf{k}) = 0$ (see black dots in Figures 3.5 (a) and (b)). These critical points are known as Van Hove singularities [131, 132]. Since the velocity of the electron/hole decreases to zero and then increases in an opposite direction when the momentum-space trajectory travels across a Van Hove singularity, the direction of the real-space trajectory is reversed and the recombination of the electron-hole pair is possible.

Along the classical evolution of an electron/hole, it behaves dynamically as a wave or a particle, depending on its wavelength. The concept of collision in strong-field physics is applied when the particle nature of the electron/hole is dominant. For an electron/hole moving in a periodic lattice, the collision with other atoms can occur only when the wavelength of the electron/hole is small enough to be comparable to the length of the unit cell. In the classical motion of solid-state HHG, the variation of the excited electron/hole's wavelength with time can be traced by the trajectory in momentum space. The electron-hole pair created around the Γ point with a small wave number behaves as a wave with a wavelength much larger than the length of the unit cell. So that the electron/hole in the low-momentum region will pass across atoms as if they were absent and therefore the electron/hole is not scattered by them. When the electron/hole is driven to the high-momentum region, e.g., around the edge of BZ, the wavelength of the electron/hole is reduced to be comparable with the length of the unit cell. Our results reveal that the

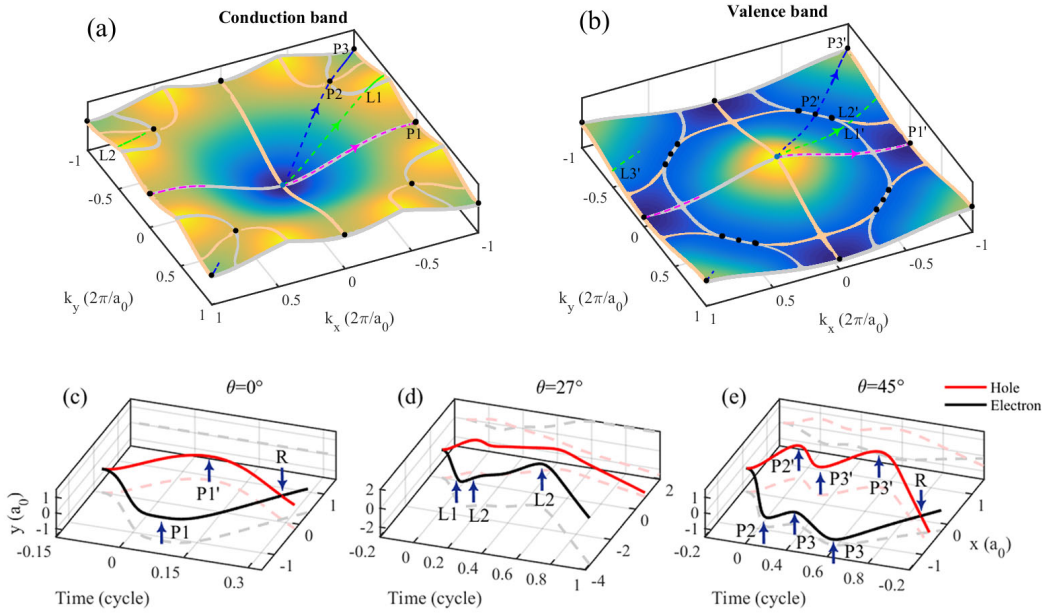

Figure 3.5: Mapping between the band structure and the collision dynamics. (a, b) Two-dimensional conduction and valence band structures of MgO. The black dots are Van Hove singularities where $\nabla_{\mathbf{k}} E_{c/v}(\mathbf{k}) = 0$. The light yellow (grey) solid curves are critical lines where $\nabla_{k_x(k_y)} E_{c/v}(\mathbf{k}) = 0$. (c–e) The evolution of electron (black) and hole (red) trajectories selected with an ionization time before the field crest for (c) $\theta = 0°$, (d) $\theta = 27°$, and (e) $\theta = 45°$. The deep pink, green, and yellow dashed curves in (a) and (b) show the momentum-space trajectories for $\theta = 0°$, $\theta = 27°$, and $\theta = 45°$, respectively. Taken from Ref. [119].

occurrence of collision with neighboring atoms and back scattering-assisted recombination requires that the ionization happens before the crest of the field. With increasing time-dependent field amplitude, the electron-hole pair is possibly driven to high-momentum regions. This type of recombination can only be observed in solids.

For the case of $\theta = 27°$ in which the ionization happens before the crest of the field, as shown in Figure 3.5(a) and (b) (light yellow and grey lines in the band structure), the momentum-space trajectory never travels across critical points (black dots) but across critical lines. The critical lines are distinguished from critical points by that only the derivative with respect to one direction vanishes, i.e., $\nabla_{k_x} E_{c/v} = 0$ ($\nabla_{k_y} E_{c/v} = 0$) at light yellow (grey) lines. It implies that the trajectory is impossible to fully reverse its direction but partly deviates from its original direction. It is shown in Figure 3.5(d) and [133] that the real-space trajectory with the ionization at $-0.13T_0$ experiences a forward scattering by a side collision with neighboring atoms. After experiencing several such side collisions which are marked by $L1$, $L2$, and $L3$, the electron gets more and more apart from its associate hole which makes the recombination hard to happen. Therefore, in Figure 3.4, the trajectory set "1" and also the emission in the high energy part are absent in this direction.

For the case of $\theta = 45°$, there are two Van Hove singularities in the high-momentum region marked by "P2" and "P3" in the conduction band and "P2'" and "P3'" in the valence band in Figures 3.5(a) and (b). As shown in Figure 3.5 (f) and [134] with the ionization at $-0.18T_0$, multiple backward scatterings by neighboring atoms occur during the trajectory evolution which originates from the momentum-space trajectory passing through two Van Hove singularities in respective bands. As a result, it takes a longer travel time before the electron recombines with its associated hole. In the classical trajectory simulation, the dephasing rate of the polarization is not considered and thus the changing of the quantum trajectory coherence over time is not described. The longer excursion time for this trajectory implies that the probability amplitude of recombination is more attenuated. This explains why in Figure 3.4 the emission is weaker and the recombination time is later for $\theta = 45°$ than for $\theta = 0°$.

The important role of Van Hove singularities of band structures played in the high harmonic emission has been noticed in Ref. [87]. In that paper, it has been revealed that for recombination occurring at those singularities where $\nabla_{\mathbf{k}} E_c = \nabla_{\mathbf{k}} E_v = 0$, the amplitude of the trajectory is infinite, rendering the semiclassical model unable to analyze the dynamics. Actually, in a quantum description, recombination at these singular points leads to spectral caustics and a resulting enhancement of the emission. Note that in the semiclassical trajectory model, the collision of an electron/hole with atoms when the relative velocity reaches zero is not the termination of a trajectory. Instead, it leads to backward scattering, and then the electron and the hole move in reversed directions until they reencounter each other with a different momentum. Looking closer to the experimental results shown in Figure 2 of Ref. [87] where the enhanced harmonics are indeed near but not exactly at the singular points for excitations along $0°$ ($\Gamma - X$) and $45°$ ($\Gamma - K$) directions. Our results shown in Figure 3.5 unambiguously illustrate that the representative trajectories go beyond the edge of the first BZ and terminate due to recombination which occurs close to critical points for $\theta = 0°$ and $\theta = 45°$. This is compatible with the experimental observation of Figure 2 of Ref. [87].

The trajectory set "2" shown in Figure 3.4(d), (e), and (f) which corresponds to ionization after the crest of the field is driven by the field with a time-dependent amplitude that drops to zero soon and then increases in the opposite direction. Consequently, the electron/hole moves only within a small fraction of the BZ near the Γ point. Due to the long wavelength of the electron/hole, the real-space trajectory, e.g., starting at $0.13T_0$ for $\theta = 0°$ (see [135]), evolves freely and its moving direction is inverted when the sign of the field is changed. This is similar to the atomic scenario in which the recombination is realized only by the driving electric field. Since the energy dispersion is isotropic in the low-momentum region, the high harmonic emission originated from trajectories set "2", which dominates in the low-energy region of the plateau, exhibits a weak anisotropy.

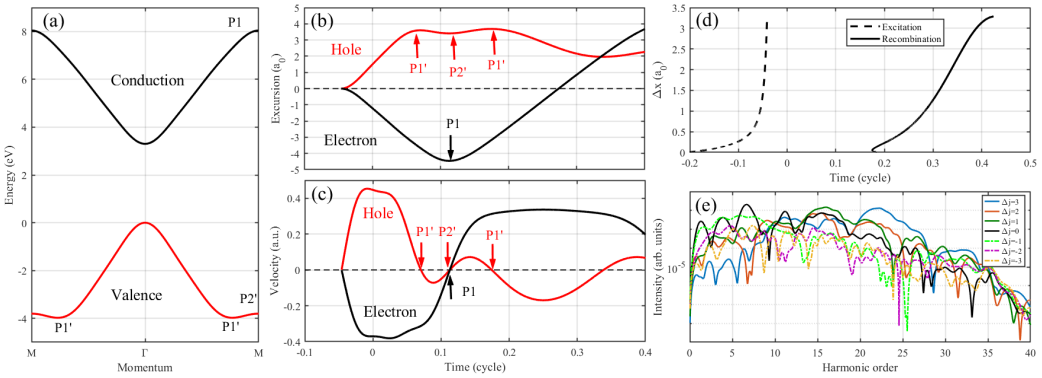

Figure 3.6: Combined semiclassical trajectory and Wannier expansion analyses of the HHG delocalization from ZnO. (a) One-dimensional conduction and valence band structures along the $\Gamma - M$ direction in ZnO adopted from Ref. [58]. The selected trajectory evolution of (b) position and (c) velocity for the electron (black) and hole (red) with ionization time at $-0.046T_0$. (d) The positions of the electron and hole upon recombination for that of ionization as a function of both ionization (dashed curve) and recombination (solid curves) instants, respectively. (e) The displacement between recombination and ionization positions in real space obtained from site-resolved polarization with the same laser and material parameters as in (d). Taken from Ref. [119].

3.5 Multiple scatterings and delocalization

It has been demonstrated in Ref. [58] that in the process of HHG from ZnO, the electron may recombine with the hole at an atomic site in the periodic lattice which is different from the original site where the electron-hole pair is born. This feature is called delocalization of harmonic emission, which is revealed by a Wannier-Bloch transition analysis [58]. Our proposed neighboring atom scattering-assisted electron-hole recombination mechanism enables us to get further insight into this phenomenon of delocalization. Figure 3.6 (a) shows the band structure along the $\Gamma - M$ direction of ZnO that is adopted in Ref. [58]. There exists only one Van Hove singularity in the conduction band (indicated by "P1"), whereas two are presented in the valence band (indicated by "P1'" and "P2'") in the high-momentum region. We perform a simulation of HHG using a single-cycle pulse with a photon energy of 0.38 eV. As shown in Figure 3.6(b) and the real-time evolution of the real- and momentum-space trajectories [136] that starts at $-0.046T_0$, the electron experiences one and the hole three backward scatterings due to the different number of critical points in the conduction and valence bands. The multiple scattering makes the average velocity of the hole lower than that of the electron because the velocity direction of the hole is changed more than once (see Figure 3.6(c)). Thus, when the electron returns to the parent atomic site where it was born, the hole does not yet reach. Then the electron continues to move toward the hole until they reencounter one another near another atomic site.

Figure 3.6(d) shows the displacement between the creation and the recombination positions

of an electron-hole pair $|\Delta j|$ as a function of both the ionization and recombination instants. With increasing ionization and recombination instants, $|\Delta j|$ for the corresponding trajectory grows from 0 to 3. Since the process of HHG is dominated by short trajectories, the slope of the function of the energy-time relation is positive (which is not shown here and is similar to the results of MgO shown in Figure 3.4(a)). By mapping this relation onto the curves shown in Figure 3.6(d), one can know that $|\Delta j|$ increases with the harmonic energy. Figure 3.6(e) shows the spectra of the interband polarizations (the bandgap corresponds to the harmonic order of 8.66 and the cutoff energy 31) for Δj which varies from -3 to 3, which are obtained by an approach of Wannier expansion [58]. For the harmonic above the band gap, the spectrum of HHG is dominated by the contributions from $|\Delta j| \geq 0$. The dominant $|\Delta j|$ near the bandgap is around 0. With increasing harmonic energy, $|\Delta j|$ of the strongest contribution gets larger. Remarkably, the contribution from $|\Delta j| = 3$ dominates largely over others for a wide spectrum below and near the cutoff. This is consistent with the feature shown in Figure 3.6(d). Our results reveal that the delocalization in the HHG process, i.e., the shift of the recombination site with respect to the position of creation is closely related to the different numbers of scatterings of the electron and the hole during the classical motion, which is determined by the Van Hove singularities in the band structure.

3.6 Ellipticity dependence of high harmonic generation

As discussed above, the forward scattering caused by side collisions with neighboring atoms suppresses the high harmonic emission in directions where the trajectories pass through critical lines when driven by a linearly polarized electric field. One can expect that such side collisions would be the primary collision when driven by an elliptically polarized field. Different from the dynamics in the linearly polarized case, side collision can happen multiple times in the elliptically polarized case which, however, facilitates the recombination of the electron and the hole. The experimental measurement of HHG excited by an elliptically polarized field [92] exhibits a nonmonotonic dependence of the $19th$ order harmonic yield on the ellipticity. There is a notable enhancement of the yield at high ellipticities. To understand this behavior, we perform semiclassical trajectory simulations for the particular ellipticities where the experimentally measured $19th$-order harmonic yields are locally maximal [92], i.e., $|\varepsilon| = 1$ (which is actually a circular polarization) with a major axis along the Mg-O boding direction and $|\varepsilon| = 0.65$ for which the major axis is along O-O (also Mg-Mg) direction. The real-space trajectories for these two laser conditions are shown in Figure 3.7 and the corresponding real-time evolutions can be found in [137, 138]. The results clearly show that the recombination of the electron and the hole is possible after a complex propagation. During the propagation, side collisions that correspond to traveling across critical lines in momentum space are the key process to drive them back to each other.

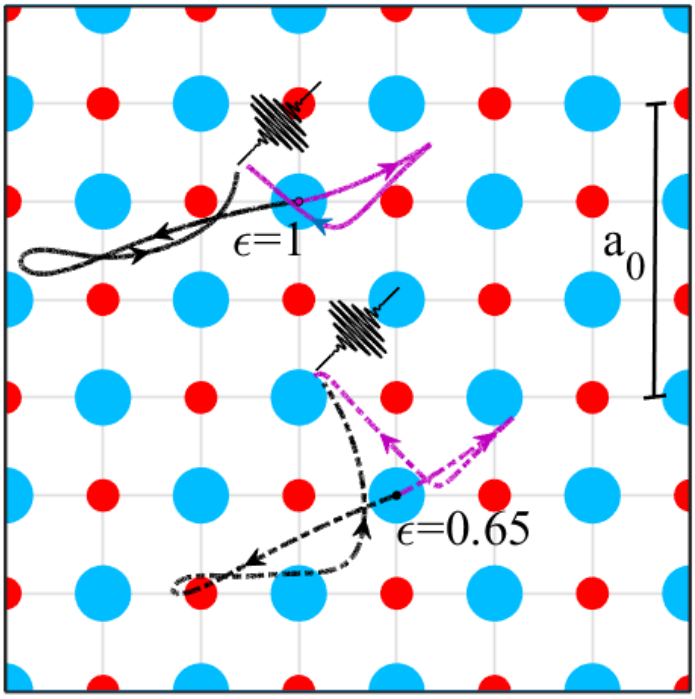

Figure 3.7: Electron (black) and hole (magenta) trajectories for circular $|\varepsilon| = 1$ (solid curves) and elliptical polarization $|\varepsilon| = 0.65$ (dot-dashed curves). Taken from Ref. [119].

3.7 Conclusions

In this chapter, we highlight the crucial role of electron/hole collisions with neighboring atoms for solid-state HHG. This process is associated with the band structure of the system and has been analyzed within the semiclassical electron-hole recombination picture. We uncover two distinct electron-hole dynamics in solids, one of which is similar to that for atomic HHG and the other one is exclusive for solids. The latter is closely linked to the structure of the system and leads to the unique features in the HHG spectrum. Electrons and holes are usually generated around the band edge with the lowest crystal momentum (Γ point in k space), implying that their wavelengths are much larger than the atomic scale. Along the subsequent field-driven dynamics, the wavelength of the electron and hole changes due to the motion in momentum space. If the electron and hole travel over a small fraction of the BZ near the Γ point, no scattering with atoms they pass by occurs. In this case, similar to the behavior in atomic HHG, the recombination of the electron and its associated hole is only possible when a sign-flipped field drives them back. Consequently, the HHG spectrum in the low energy region above the band gap resulting from such

dynamics exhibits only a weak anisotropy.

When the ionization happens before the crest of the field and the field strength is strong enough, the electron-hole trajectory can reach the edge of the BZ and experience Van Hove singularities (where $\nabla_{\mathbf{k}} E_{c/v}(\mathbf{k}) = 0$) and critical lines (where $\nabla_{k_x} E_{c/v}(\mathbf{k}) = 0$ or $\nabla_{k_y} E_{c/v}(\mathbf{k}) = 0$). In this regime, the wavelength of the electron and the hole is reduced to the order of the atomic scale, i.e., the unit cell, making collisions with atoms possible. Passing across Van Hove singularities of the band structure gives rise to head-on collisions and backward scattering. This is the main cause for reversing the direction of the trajectory and consequently leading to the recombination of the electron-hole pair with no need for a sign change of the electric field. In addition, passing through critical lines results in side collisions, and forward scatterings suppress the recombination for linear polarized light, but are the main origin of the harmonic yield enhancement for an elliptically polarized field. Thus, different collisions and scattering processes are responsible for the orientation-dependent high harmonic yield.

The presented theoretical study reveals a fundamental difference in the recombination mechanism between atomic and solid-state HHG and paves the way toward a more complete understanding of the underlying collision dynamics in solids. Furthermore, it promises to control the high harmonic emission by manipulating the subcycle collision dynamics via all-optical approaches.

Characterizing the tunneling dynamics in solid-state high harmonic generation

4

In strong-field light-matter interaction, photo-ionization is a fundamental and ubiquitous quantum process that triggers many attosecond-scale phenomena, such as HHG, photo-electron holography, electron diffraction, and molecular orbital tomography [139–144]. Tunneling ionization is a process of an electron overcoming a potential barrier which is induced by an oscillating electric field. The properties of electronic wave packets in the barrier region are subject to the rapid modulation of the barrier. On the subcycle timescale, the tunneling probability and the tunneling exit change with the instantaneous field amplitude. The characters of the liberated electrons are determined by the tunneling dynamics and strongly dictate the subsequent dynamics. To resolve the fingerprint of the tunneling ionization on the liberated electrons, a couple of spectroscopic schemes have been proposed that can experimentally access the attosecond timescale and the angstrom lengthscale of electron dynamics, such as HHG measurement for subcycle temporal gating [123] and multi-color interferometry [125, 145–147]. These measurements have been mainly conducted in atomic gases and provide significant insights into the tunneling ionization process. However, so far, only few such studies for solid-state HHG exist.

The Keldysh approach [148] defines a Keldysh parameter $\gamma_K = \sqrt{\frac{I_p}{2U_p}}$ where I_p is the ionization potential (bandgap for solids) and $U_p = \frac{E^2}{4\omega^2}$ is the ponderomotive energy. γ_K classifies photoionization into adiabatic tunneling for $\gamma_K \ll 1$, diabatic tunneling for $\gamma_k \sim 1$, and multiphoton ionization for $\gamma_K \gg 1$ [149–151] and treats ionization in gases and solids on equal footing. Figure 4.1 illustrates these regimes for periodic lattice potentials with an applied electric field. In the adiabatic tunneling regime, the external field acts quasistatically and the electron penetrates the potential barrier "horizontally" without changing its total energy (denoted by the solid black arrow in Figure 4.1). In contrast, in the multiphoton regime, optical transitions occur along the "vertical" channel without passing through the potential barrier, i.e., the bandgap, as shown by the red arrows in Figure 4.1. Nonadiabatic tunneling (denoted by the dashed purple line in Figure 4.1) is an intermediate regime between these two opposite limits which is applied to most of the real tunneling process. In this regime, the electron acquires some energy during the passage of the classically forbidden region.

The results presented in this chapter were already published in [152].

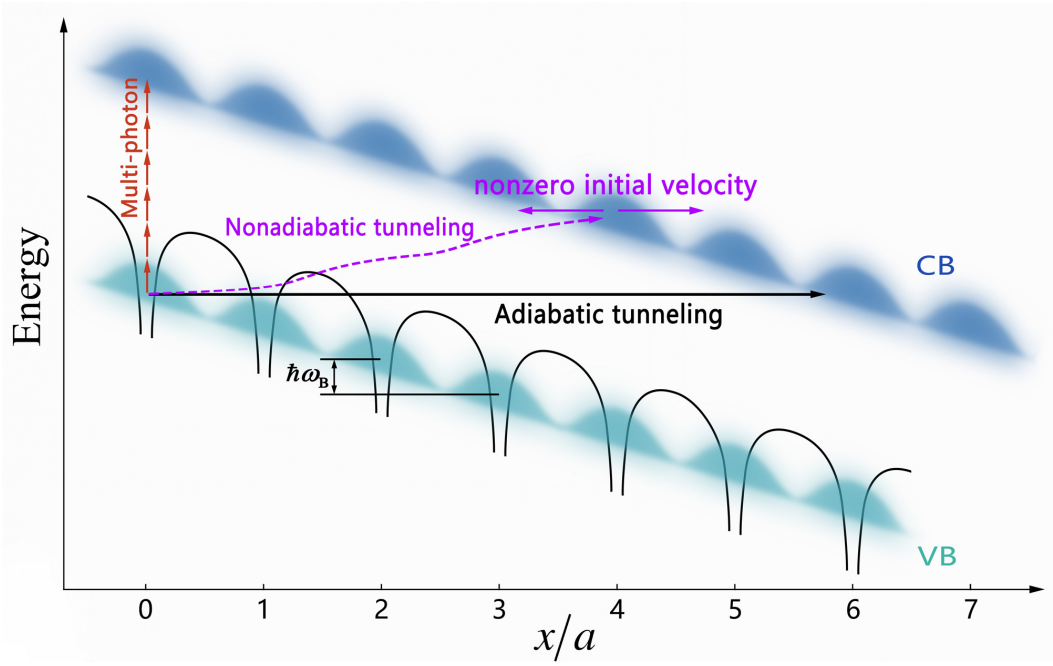

Figure 4.1: Schematic real-space representation of multiphoton ionization (red arrowed line), adiabatic tunneling (black solid arrowed line), and nonadiabatic tunneling (dashed purple arrowed line) in crystalline solids. Taken from Ref. [152].

4.1 Resolving tunneling processes by the semiclassical trajectory model

In the attosecond-scale control scheme of atomic HHG measurements aiming to probe the tunneling dynamics, experimental observations are often analyzed within a framework of the semi-classical trajectory model based on the saddle-point approach [123, 125, 153–157]. The quantum tunneling, classical propagation, and quantum recombination steps of HHG in an atom are implicitly included in the quantum description, i.e., the time-dependent Schrödinger equation (TDSE). The high harmonic spectrum is determined by the coherent sum of all possible quantum trajectories that are characterized by a quasiclassical action [121]. By means of the saddle-point analysis based on the quasiclassical action, one is allowed to isolate the tunneling process from the subsequent dynamics, resolve the tunneling exit shift and the coherent properties of quantum trajectories at the tunneling exit, i.e., relative phase and amplitude, and identify the non-adiabaticity of the tunneling in atoms [123, 125]. The semiclassical trajectory model used for atoms has been generalized to solids, however, it has not yet been combined with experiments to provide more insights into the tunneling physics underlying the solid-state HHG.

In Chapter 3, it has been pointed out that an approximation zeroing the band gap is applied when solving saddle-point equations to ensure real-valued solutions. By doing so, quantum

aspects of the processes leading to HHG are omitted. In the purely classical model with this approximation, the initial electron-hole separation of the classical motion is assumed to be zero. Recently the validity of the electron-hole recombination mechanism based on the purely classical trajectory analysis has been questioned by several studies because it fails to reproduce some features of HHG in solids [91, 158]. An argument has been proposed that wavelike electrons and holes partially, not necessarily fully, overlap before and/or after the classical propagation [91, 158]. A recent study has shown that interband dipole transition in real space can happen between distant lattices via analysis of the Wannier function expanded high harmonic emission[60]. These considerations seem to account for the separation between electron and hole (parent ion) which arises from moving through the potential barrier. It has been predicted in the Wannier-Stark ladder formed by a static field, that the hopping distance among lattices in the purely adiabatic tunneling regime can be approximated as $N = E_g/aF(t)$, where E_g is the band gap, a the lattice constant, and $F(t)$ the electric [86], which resembles the adiabatic tunneling exit point in the atomic phase, i.e., $z_{exit} = I_p/F(t)$.

Following the full procedure of correctly solving the saddle-point equations that is used for atomic HHG [122, 159, 160], we solve the solid-state saddle-point equations rigorously and the resulting ionization time t', recombination time t, and canonical momentum $\mathbf{k}_0$ are complex-valued. The complex solutions of the saddle-point equations provide a three-step picture that includes quantum processes of tunneling and recombination which occur along the imaginary time axis and a classical propagation along the real-time axis, as schematically illustrated in Figure 4.2. The physical interpretation of these quantities is as follows. The real part of $\mathbf{k}_0$ is the crystal momentum of an electron-hole pair in the absence of an electric field and the imaginary part is associated with the quantum properties of the electronic wave function [125]. The ionization time $t' = t'_r + it'_i$ is the starting point of a quantum trajectory upon the creation of an electron-hole pair. The real part t'_r denotes the instant when the electron reaches the tunneling exit point and also the starting point of the classical motion. The imaginary part t'_i represents the duration of the tunneling which is associated with the weight of the quantum trajectory [125]. The recombination time $t = t_r + it_i$ is understood in the same sense as the ionization time with t_r denoting the end time point of the classical motion and t_i being the time that the electron needs to cross the potential barrier for the recombination with the hole. The electron-hole separation after the tunneling ionization is obtained by evaluating the travel distance of the electron through the classically forbidden region $\Delta\mathbf{r} = \int_{t'}^{t'_r} d\tau \Delta\mathbf{v}(\mathbf{k}(\tau))$ where $\Delta\mathbf{v}$ is the velocity difference between the considered conduction and valence bands and $\mathbf{k}(\tau) = \mathbf{k}_0 + \mathbf{A}(\tau)$ the time-dependent crystal momentum. To distinguish it from the traditional purely classical trajectory analysis, the trajectory analysis based on the complex-valued solutions of the saddle-point equations discussed below is referred to as quantum trajectory analysis.

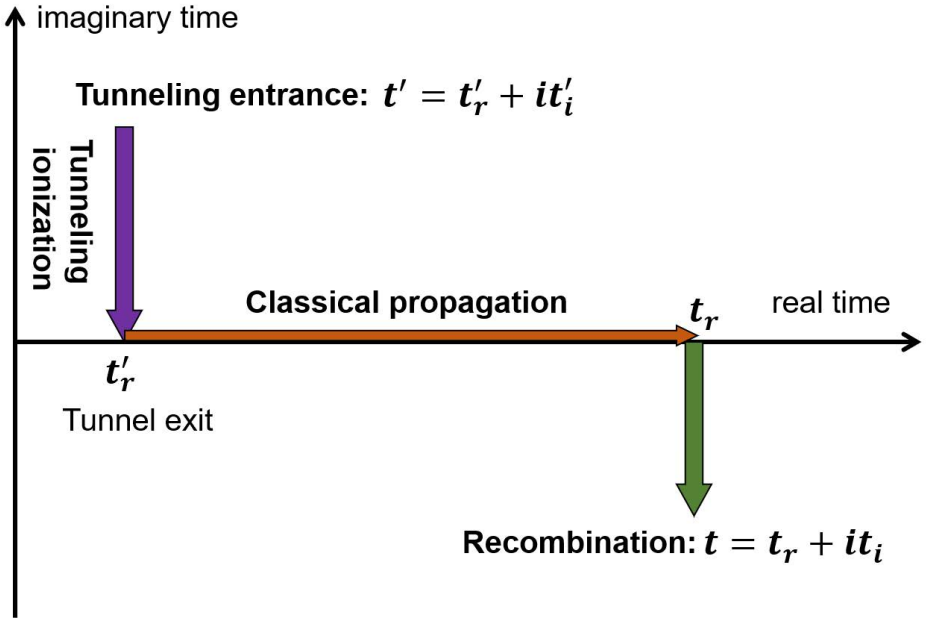

Figure 4.2: Path of the time integration in the quasiclassical action S. The tunneling ionization and the recombination occur along the imaginary time axis and the classical propagation along the real-time axis. Adapted from Ref.[160].

4.2 Comparison of the classical and quantum trajectory analyses

To reveal the effects of the tunneling dynamics in the high harmonic emission, we focus on the HHG measurement on ZnO crystals that was carried out in Refs. [28, 61]. When using the classical recollision model to predict the emission time of the harmonics obtained by the SBE simulations, it has been demonstrated that the classical model seems to work well for weak field amplitudes, whereas it fails to agree with the experiment for the strong-field excitations [61]. It is explicitly shown that the SBE simulations agree well with the attosecond interferometry experiment on ZnO [28]. Therefore the SBE simulation results are taken as a benchmark to test the accuracy of our quantum trajectory-based analysis. In our calculations, the one-dimensional band structure of the valence and the conduction bands along the $\Gamma - M$ direction is expanded as [28, 56, 61]

$$E_v(k) = \sum_{j=0}^{5} \alpha_v^j cos(jka), \tag{4.1}$$

$$E_c(k) = E_g + \sum_{j=0}^{5} \alpha_c^j cos(jka), \tag{4.2}$$

where $a = 0.2814\ nm$ is the lattice constant along the $\Gamma - M$ direction, $E_g = 3.3\ eV$ is the band gap of the ZnO crystal, and $\alpha^j_{c(v)}$ $(j = 0, 1, ..., 5)$ are the expansion coefficients of the conduction (valence) band which are provided in Ref. [56]. The dipole matrix element is simply approximated as a constant $d = 0.183\ e\ nm$. To check whether the theoretical issue left in Ref. [61] can be resolved by the quantum trajectory analysis, the same laser parameters are applied in our simulations, i.e., the electric field is linearly polarized along the $\Gamma - M$ direction with a wavelength of 3.25 μm. The resulting high harmonic emission in the plateau region is dominated by interband polarization.

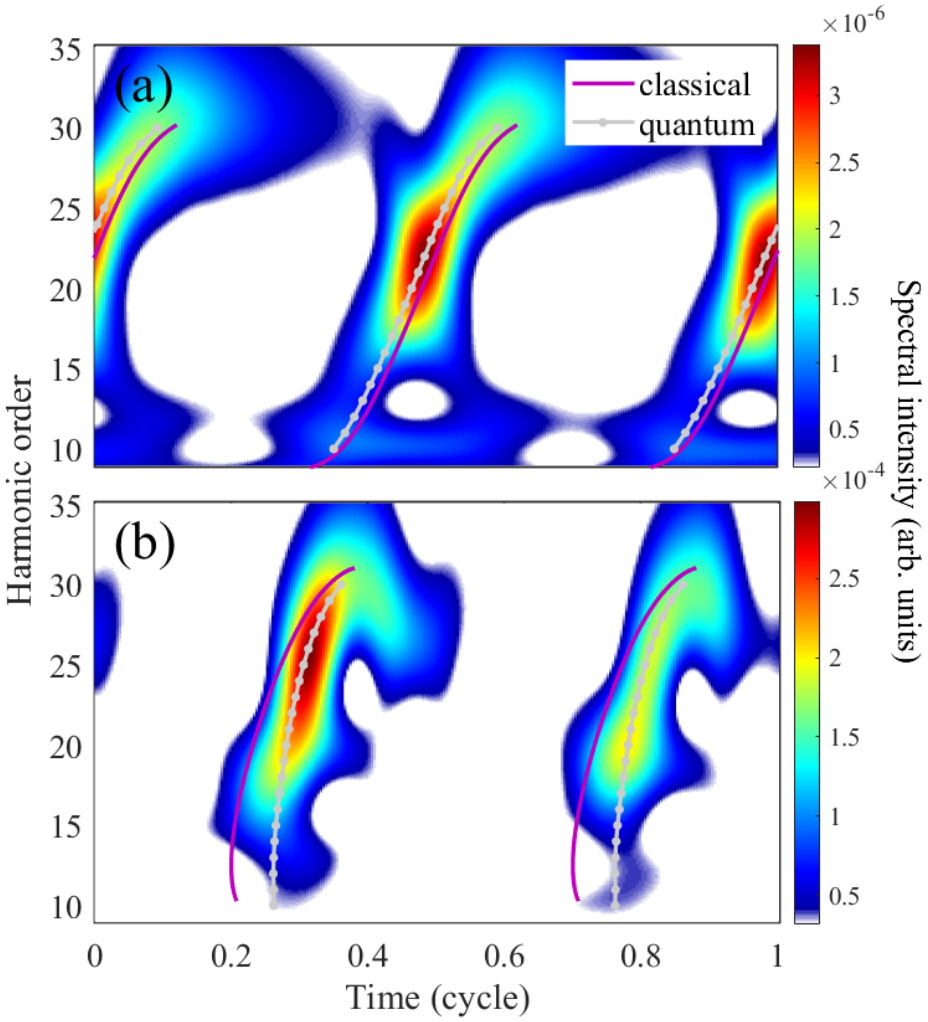

Figure 4.3: The color-coded contours show HHG as a function of the time obtained from the SBE simulations for ZnO in (a) lower- and (b) higher-field cases discussed in the main text, respectively. The dotted grey and purple solid curves are the predictions of the emission time based on the quantum and the classical trajectory analyses, respectively. Taken from Ref.[152].

The results of the emitted high harmonics in the plateau region as a function of the time obtained from the SBE simulations (color maps) for excitation field amplitudes of $E_0 = 2.52V/nm$ (left panel) and $E_0 = 4.1V/nm$ (right panel) are displayed in Figure 4.3. The applied field amplitudes are representative of the weak and the strong field regimes. The high harmonic emission in the plateau region is dominated by the interband polarization, and therefore the electron-hole collision model is suitable for analyzing the underlying electron dynamics. The purple and dotted grey lines in Figure 4.3 are the predictions of the emission time by the classical and quantum trajectory analyses, respectively. In our analysis, only short trajectories with positive chirps are considered since they are responsible for the main emissions in the SBE results.

It is clearly shown that the quantum trajectory results coincide excellently with the SBE results for both the lower- and higher-field cases. In contrast, the prediction by the classical trajectory analysis deviates severely from the SBE results in the higher-field case, as is already pointed out in Ref. [61]. We find that in both cases, the distance accumulated along the imaginary part of the recombination time is nearly zero (shown in Figures 4.5(e) and (f) below), which implies that the center of the electron wave packet spatially overlaps with that of the associated hole at the end of the classical evolution. This feature is different from the argument that the electron and hole wave packets do not have to fully overlap spatially with each other for recombination [91]. Therefore, the deviation of the classical trajectory analysis from the SBE results lies predominantly in the tunneling ionization process.

Figure 4.4 shows the tunneling characters at the tunneling exit for the lower (left column) and higher (right column) excitation fields as quantified by the quantum trajectory analysis. The dotted red curves in Figures 4. 4(a) and (b) denote the spatial separation between the electron and the hole arising from the tunneling ionization. The separation is surprisingly large, which makes the subsequent classical propagation significantly different from that given by the purely classical trajectory analysis where the electron and hole are assumed to move classically starting from the same position. The ratio $\frac{E_g}{\tilde{\omega}_B(t)}$ ($\tilde{\omega}_B(t) = aF(t)$ is the instantaneous Bloch frequency) defines the distance (in units of the lattice constant) required for an electron tunneling along a horizontal pathway to a state in the conduction band, which is actually the adiabatic tunneling. The dotted blue curves in Figures 4.4(a) and (b) for this ratio are obtained with the instantaneous field amplitude extracted from the quantum trajectory-based results. In the lower-field case, the electron-hole separation before the classical motion is about five to six lattice constants, which is one to two lattice constants smaller than the corresponding unrealistic adiabatic tunneling distance (blue curve). This indicates that the tunneling ionization in this case is nonadiabatic. In the higher-field case, as the potential barrier is bent more significantly than that by the lower field, the tunneling distance is shorter. The electron-hole separation is smaller by less than one lattice constant compared to the adiabatic scenario for harmonic energies near the band gap. With increasing harmonic energy, the difference between the two curves approaches zero, suggesting that the tunneling ionization is nearly adiabatic in this case.

The electron acquires energy during the nonadiabatic tunneling and therefore a nonvan-

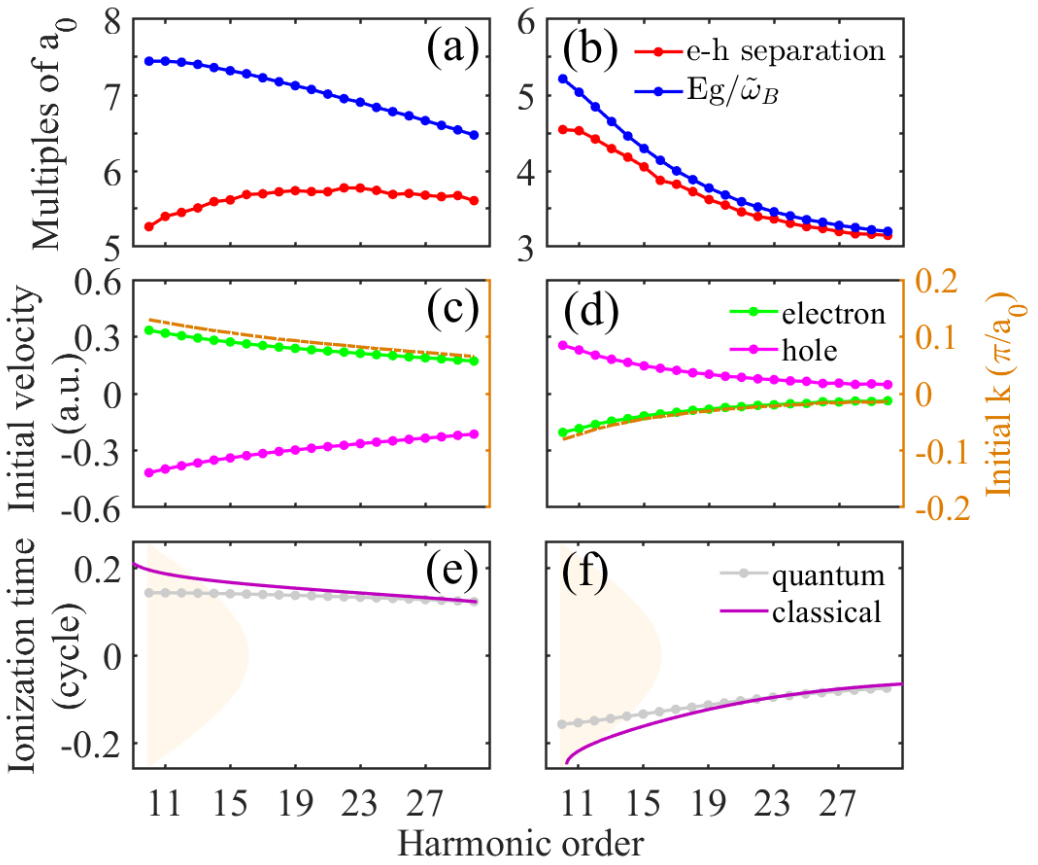

Figure 4.4: Characters of electron and its associated hole after tunneling through the potential barrier in the lower- (left column) and higher-field (right column) cases. (a) and (b) show the electron-hole separation in units of lattice constant within the quantum (red curves with dots) and the purely adiabatic (blue curves with dots) analyses, respectively. (c) and (d) show the initial velocities of the electron (green curves with dots) and the hole (magenta curves with dots) and the crystal momenta where the electron emerges in the conduction band with a hole left in the valence band (orange dash-dotted curves). (e) and (f) show the real part of the ionization time obtained within the quantum (grey dotted line) and classical (purple solid) trajectory analyses. The filled yellow areas in (e) and (f) show the half-cycle wave shape of the electric field. Taken from Ref. [152].

ishing velocity of the electron at the tunneling exit is expected, as has been quantified in atomic HHG [125]. Figures 4.4(c) and (d) display the initial velocities of the electron (dotted green curves) and the hole (dotted magenta curves) in the direction of the field polarization. The exact position where the electron emerges in the conduction band in momentum space is shown by the dashed yellow curves. In the lower-field case, the nonadiabatic tunneling induces a nonzero initial velocity for the electron and hole which are created noticeably away from the band edge (Γ point in momentum space). Closer to the adiabatic regime, e.g., the higher-field case, the initial velocity of the electron and hole decreases to nearly

zero and the corresponding interband transition gets close to the Γ point with increasing harmonic energy. Figures 4.4(e) and (f) show the starting instant of the classical evolution (the real part of the ionization time) as a function of the harmonic energy. The ionization predominantly occurs after and before the crest of the field in the lower- and higher-field cases, respectively.

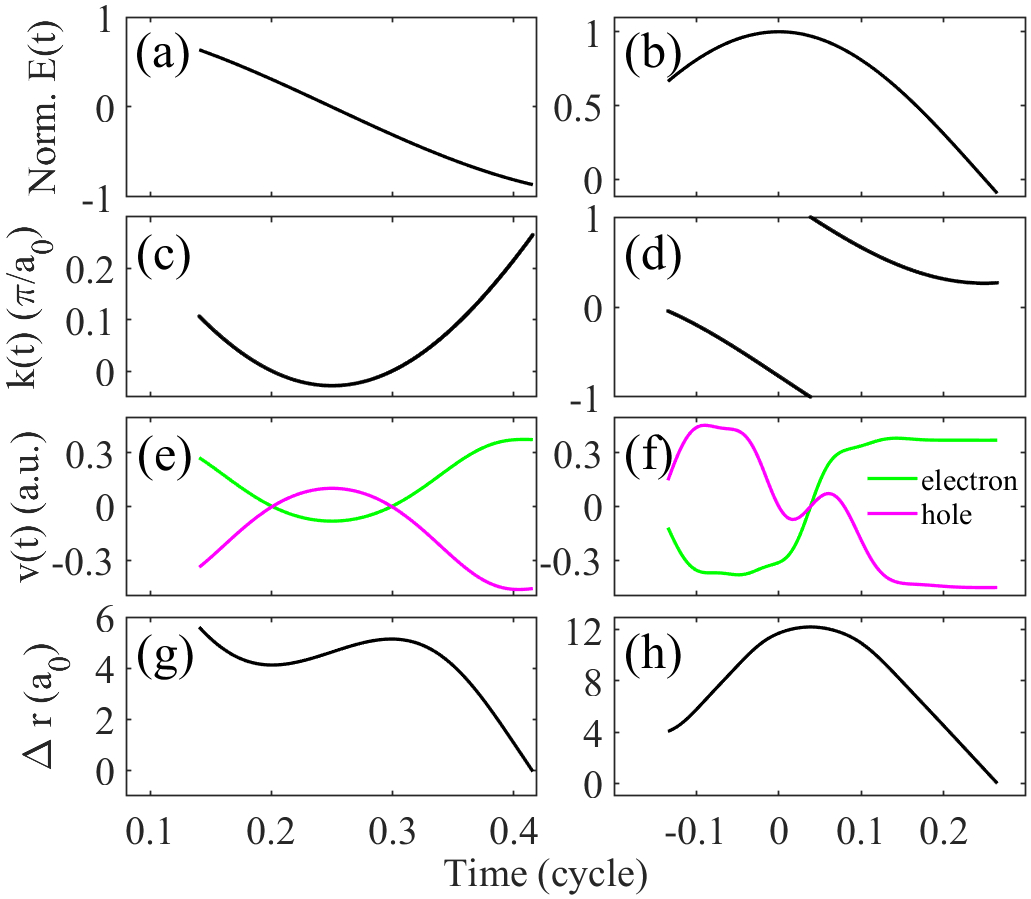

Figure 4.5: Real-time evolution of the trajectories responsible for the 15th harmonic for the lower- (left column) and the higher-field (right column) cases, as discussed in the main text, respectively. (a) and (b) show the waveform of electric fields in the time window of the entire classical motion, (c) and (d) show the time-dependent crystal momenta $k(t)$, (e) and (f) show the time-dependent velocities of the electron (green) and the hole (magenta), and (g) and (h) show the time-dependent electron-hole displacements. Taken from Ref. [152].

Figure 4.5 displays the evolution of the trajectory associated with the 15th harmonic emission along the real axis of time, specifically the crystal momentum $k(t)$, the velocities of the electron and hole $v_{e/h}(t)$, and the spatial displacement between the electron and hole $\Delta r(t)$. In the lower-field case, as the sign of the initial velocity of the electron is opposite to that of the instantaneous vector potential, the electron and hole are decelerated with a

relative distance reduced at the beginning of the classical motion. The electron and the hole then move backward and toward each other under the action of the field until they spatially overlap. In the higher-field case, the electron and the hole speed up away from each other just after the tunneling and they can reach the edge of the first BZ where Bragg scattering happens. As studied in the previous chapter, the collision of the electron and hole with neighboring atoms upon the Bragg scattering leads to the reversion of their moving directions such that they can eventually meet each other [152].

4.3 Probing the tunneling dynamics by high harmonic interferometry

In atomic HHG, extracting the coherent properties of electron wave packets under the potential barrier is achieved via sub-cycle temporal gating and extreme-ultraviolet (XUV) interferometry [123, 125]. Such a spectroscopic scheme combines a fundamental and a relatively weak second harmonic probing fields. An experiment following this scheme has also been conducted in a solid-state system [28]. The emitted harmonic radiation from consecutive half cycles constitutes a temporal interferometer. The probing field induces a phase shift between the two arms of the interferometer and therefore gives rise to the generation of even harmonics [28, 159]. The yield of even harmonics depends sensitively on the phase delay between the probing and the fundamental fields. Varying the phase delay, the yield of each harmonic is modulated, as is observed in the experiment and SBE simulations [28]. The color maps in Figure 4.6 show the harmonic spectra up to the cut-off energy versus the relative time delay of the two color fields for the lower and higher fundamental field cases discussed above by solving the SBE. The field amplitude ratio of the second harmonic field to the fundamental is $\frac{E_{2\omega}}{E_{\omega}} = 0.01$. To get a clearer spectrum with discrete harmonics, a long pulse duration of ten cycles is used, and the other parameters are the same as the simulations in Figures 4.3 and 4.4. Our SBE simulations perfectly reproduce the experiment [28], especially the most important features such as the positions of maxima or minima of all even-order harmonics up to the $18th$ order which are resolved in the experiment. The modulation depth of the even harmonics is much larger than that of the odd harmonics. To retrieve the tunneling dynamics from the spectra, it is required to elucidate the phase delay dependence of the even harmonics within the framework of the quantum trajectory analysis.

The generation of even harmonics originates from the phase shift of the HHG interferometer induced by the probing field, which can be quantitatively analyzed within the framework of the saddle-point approach. The modification of the action resulting from the probing field can be addressed by a perturbation expansion. We expand $S(\mathbf{k}_0, t', t) = \sum_{n=0}^{\infty} \lambda^n S^{(n)}(\mathbf{k}_0, t', t)$ with $\mathbf{k}(t) = \sum_{n=0}^{\infty} \lambda^n \mathbf{k}^{(n)}(t)$ where the zeroth order is considered as the unperturbed situation that is generated by the fundamental field alone. The $\mathbf{k}(t)$ is separated into $\mathbf{k}^{(0)}(t) = \mathbf{k}_0 + \mathbf{A}_{\omega}(t)$ and $\lambda \mathbf{k}^{(1)}(t) = \mathbf{A}_{2\omega}(t)$. The term $\lambda \mathbf{k}^{(1)}(t)$ is relatively small and can be neglected when expanding $S(\mathbf{k}_0, t', t)$. Taking advantage of the harmonic

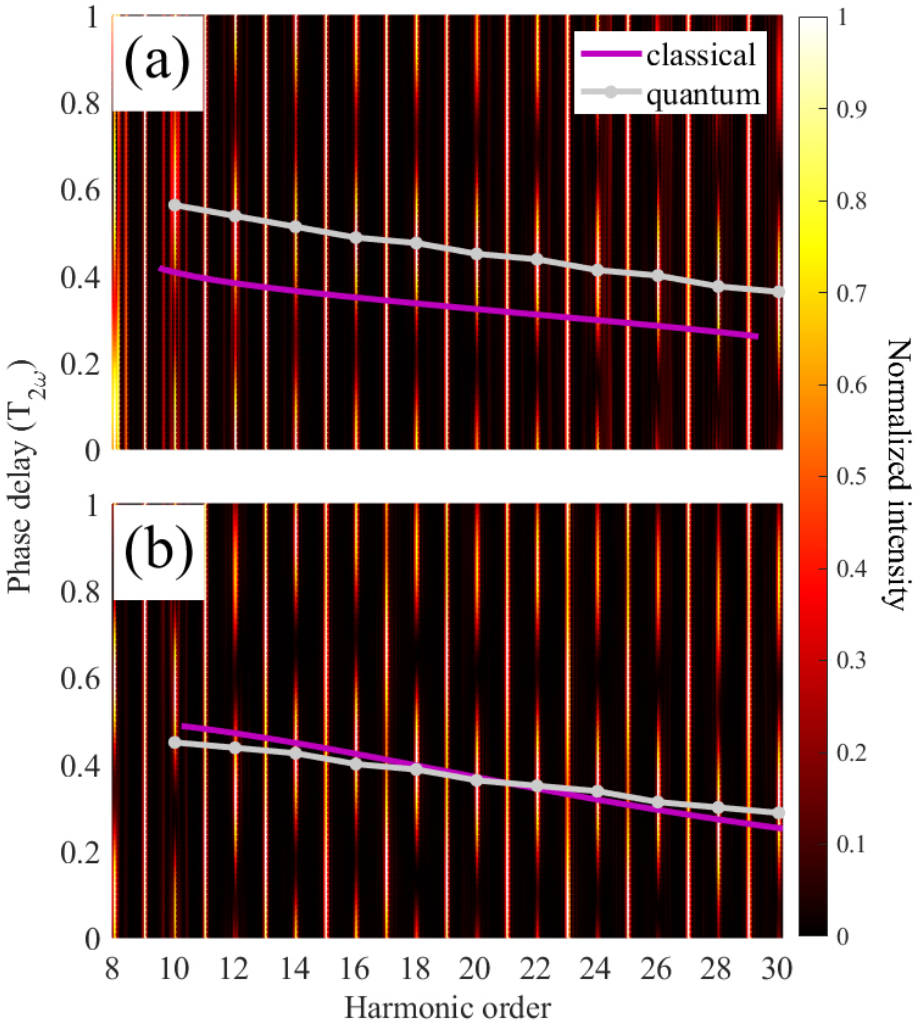

Figure 4.6: High harmonic spectra versus the phase delay between the two color fields for (a) the lower-field and (b) the higher-field cases. The color contours are obtained from solving the SBE and the curves are the predictions of Φ_{max} based on the classical (purple solid) and the quantum (white dotted) trajectory analyses, respectively. The pulse duration is 10 optical cycles, and the other parameters are the same as those in Fig. 4.3 and Fig. 4.4. Taken from [152].

cosine function expansion of the energy dispersion $\varepsilon_g(\mathbf{k}) = \sum_{j=0}^{N} \alpha_j cos(j\mathbf{k}a)$ where α_j are the expanding coefficients and a is the lattice constant, the quasiclassical action in terms of $\mathbf{k}(t)$ is expressed as

$$S(\mathbf{k}_0, t', t) = \int_{t'}^{t} d\tau \sum_{j=0}^{N} \alpha_j cos[j\mathbf{k}(\tau)a], \tag{4.3}$$

which is split into

$$S^{(0)}(\mathbf{k}_0, t', t) = \int_{t'}^{t} d\tau \sum_{j=0}^{N} \alpha_j cos[j\mathbf{k}^{(0)}(\tau)a], \tag{4.4}$$

and

$$S^{(1)}(\mathbf{k}_0, t', t) = -\int_{t'}^{t} d\tau \sum_{j=0}^{N} \alpha_j j\mathbf{k}^{(1)}(\tau) sin[j\mathbf{k}^{(0)}(\tau)a]. \tag{4.5}$$

The perturbative term of the action, i.e., $S^{(1)}(\mathbf{k}_0, t', t)$ is denoted as $\sigma(\mathbf{k}_0, t', t, \phi)$ in which the phase delay of the second harmonic field is included. It was found to be related to the unperturbed group velocity difference and the second harmonic vector potential by

$$\sigma(\mathbf{k}_0, t', t, \phi) = -\int_{t'}^{t} d\tau \mathbf{A}_{2\omega}(\tau, \phi) \nabla_{\mathbf{k}} \varepsilon_g(\mathbf{k}^{(0)}(\tau)). \tag{4.6}$$

The perturbation associated with two consecutive half cycles is identical but occurs with opposite signs, i.e., $\sigma(\mathbf{k}_0, t' + \frac{T_0}{2}, t + \frac{T_0}{2}, \phi) = -\sigma(\mathbf{k}_0, t', t, \phi)$ where T_0 is the optical cycle of the fundamental field. The unperturbed signal has the same amplitude but opposite signs in two consecutive half cycles $\mathbf{E}_{out}(t + \frac{T_0}{2}) = -\mathbf{E}_{out}(t)$. The perturbation breaks the symmetry between half cycles by

$$\begin{aligned} \mathbf{E}_{total}(t) &= \sum_{cycle} \mathbf{E}_{out}(t) e^{i\sigma(t)} + \mathbf{E}_{out}(t + \frac{T_0}{2}) e^{i\sigma(t + \frac{T_0}{2})} \\ &= \sum_{cycle} \mathbf{E}_{out}(t) e^{i\sigma(t)} - \mathbf{E}_{out}(t) e^{-i\sigma(t)}, \end{aligned} \tag{4.7}$$

and the high harmonic spectrum is

$$E_{total}(n\omega_0) = \sum_{cycle} E_{out}(n\omega_0)(e^{i\sigma} - e^{in\pi - i\sigma}), \tag{4.8}$$

from which one obtains the phase delay modulation of odd and even harmonics:

$$I_{2N+1} \propto |cos[\sigma(\mathbf{k}_0, t', t, \phi)]|^2, \tag{4.9}$$

$$I_{2N} \propto |sin[\sigma(\mathbf{k}_0, t', t, \phi)]|^2. \tag{4.10}$$

It has been proven that in the scheme of high harmonic interferometry, the weak second harmonic field hardly modifies the dynamics induced by the fundamental field and therefore quantities $\mathbf{k}_0$, t', and t in Equation 4.6 are the solutions of the unperturbed saddle-point equations. The modulation of each harmonic can be calculated according to Equation 4.6 within the trajectory analysis and we use Φ_{max} which is the phase delay that maximizes the intensity of even harmonics to represent the feature of the modulation. In Figure 4.6, the dotted grey lines and purple solid lines are the predictions based on the quantum and the classical trajectory analyses, respectively. The Φ_{max} predicted by the classical trajectory analysis deviates substantially from the SBE result in the lower-field case. In contrast, the predictions based on the quantum trajectories agree excellently with the SBE results for both the lower- and the higher-field cases. As for the inaccurate prediction for lower harmonics ($10th$ and $12th$), we speculate that this might be related to near-band gap resonance effects [161] as resonant sidebands can be seen around these harmonics in Figure 4.6. Our results provide evidence that the quantum trajectory analysis is indeed valid and the tunneling dynamics are correctly described.

4.4 Linking the tunneling characteristics to high harmonic emission

Using the physically transparent quantum trajectory recollision model, the tunneling dynamics can be revealed by the experimentally measured modulation of the even harmonics in the high harmonic interferometric measurements [159]. Within the quantum trajectory analysis, the calculated Φ_{max} for the two-color excitation scheme can be linked to the electron-hole characters after the tunneling ionization, such as the initial electron-hole separations and the initial velocities of the electron and hole. The relations of Φ_{max} and these tunneling characters are shown in Figures 4.7-10 (a). Figures 4.7-10 (b) is the SBE results of Φ_{max} versus even harmonic orders for the high harmonic interferometric measurements. Mapping (a) and (b) allows one to construct a relation between the even harmonic orders and the tunneling characteristics associated with the even harmonic emission, which are shown in Figures 4.7-10 (c). As the tunneling characters continuously vary with the high harmonic emission energy, the constructed relation including odd harmonic orders can be obtained by interpolating these points.

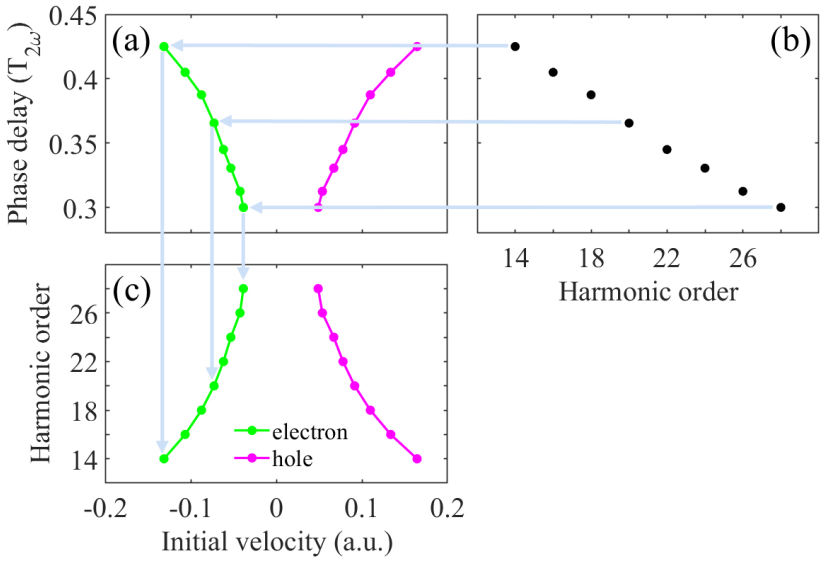

Figure 4.7: (a) The prediction of the relation between Φ_{max} and the initial velocities of the electron and hole before the classical motion based on the quantum trajectory analysis. (b) Φ_{max} versus the even harmonic orders of the high harmonic interferometry from solving SBE. (c) The reconstructed initial velocities for each harmonic obtained by mapping the data in (b) to (a). Taken from Ref. [152].

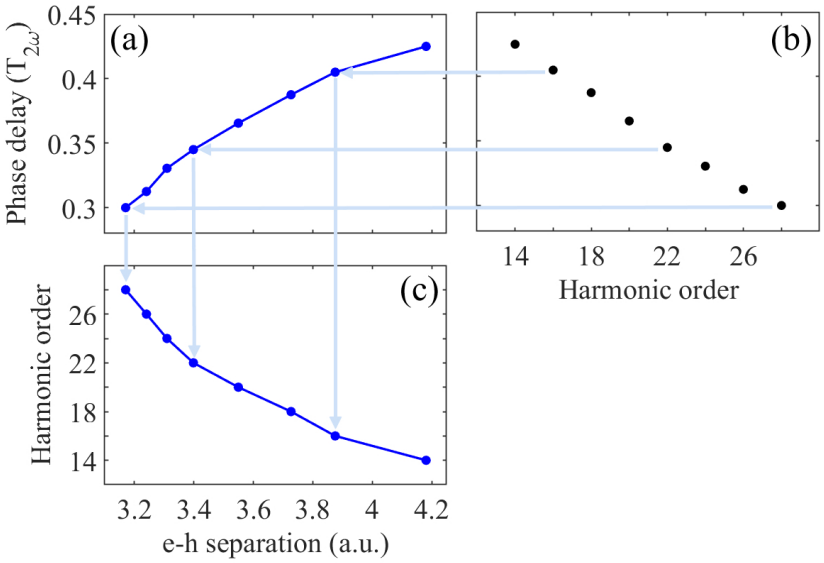

Figure 4.8: (a) The prediction of the relation between Φ_{max} and the initial relative distance between the electron and hole before the classical motion based on the quantum trajectory analysis. (b) Φ_{max} versus the even harmonic orders of the high harmonic interferometry from solving SBE. (c) The reconstructed initial displacement for each harmonic obtained by mapping the data in (b) to (a). Taken from Ref. [152].

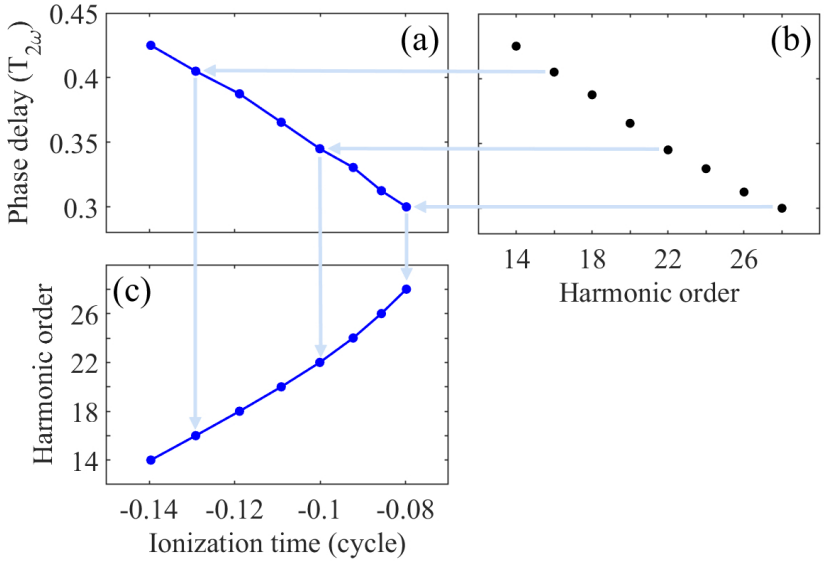

Figure 4.9: (a) The prediction of the relation between Φ_{max} and the real part of the ionization time based on the quantum trajectory analysis. (b) Φ_{max} versus the even harmonic orders of the high harmonic interferometry from solving SBE. (c) The reconstructed ionization time for each harmonic obtained by mapping the data in (b) to (a). Taken from Ref.[152].

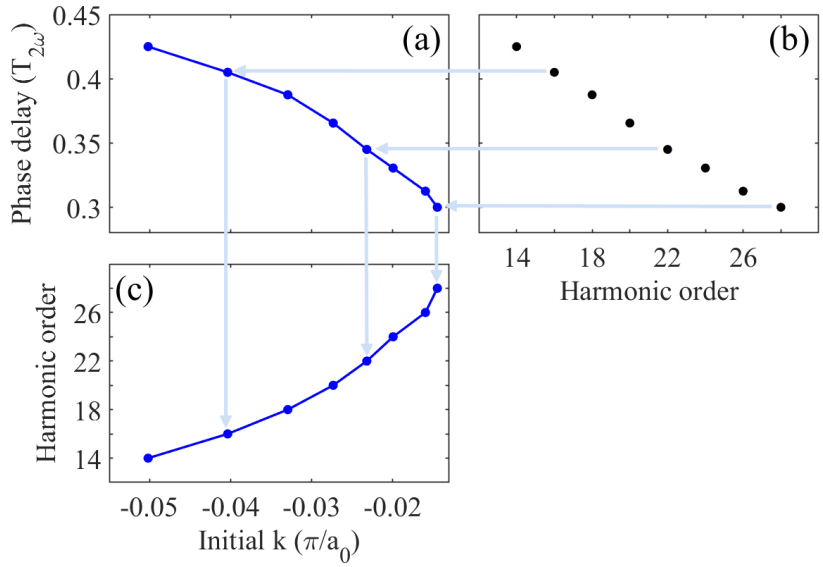

Figure 4.10: (a) The prediction of the relation between Φ_{max} and the crystal momentum where the interband transition happens based on the quantum trajectory analysis. (b) Φ_{max} versus the even harmonic orders of the high harmonic interferometry from solving SBE. (c) The reconstructed initial k point of the classical motion for each harmonic obtained by mapping the data in (b) to (a). Taken from Ref. [152].

4.5 Conclusions

In this chapter, the tunneling dynamics underlying HHG from ZnO have been revealed based on quantum trajectory analysis. We pushed the limits of the traditional solid-state electron-hole recollision model which omits the initial conditions present after the tunneling ionization for the classical motion. We proposed a refined recollision model which fully includes quantum aspects of ionization and recombination. It is demonstrated that this refined model based on quantum trajectory analysis perfectly predicts several features of the high harmonic spectrum in agreement with the SBE simulations. The quantum trajectory analysis naturally allows us to obtain a picture of nonadiabatic tunneling ionization in solid-state HHG. Within this analysis, the dynamical tunneling exit positions and the initial velocities of electron and hole changing with harmonic energy can be quantified. It is found that the reduced tunneling exit coordinate with respect to the adiabatic case is associated with a nonzero initial velocity, consistent with the nonadiabatic picture. According to the Keldysh parameter, adiabatic tunneling can be achieved by varying laser parameters, such that the initial velocities are close to zero. The most interesting finding is that the initial velocities can be inward or outward with respect to the field polarization direction which makes the electron and the hole experience deceleration or acceleration at the beginning of the classical motion. The quantitative agreement between the quantum trajectory analysis and the SBE simulations of attosecond tunneling interferometry enables us to establish a direct mapping between experimental measurements and tunneling characteristics. Our study demonstrates the feasibility of extending attosecond spectroscopic schemes from atomic systems to much more complex solid-state systems which provides a promising platform to uncover quantum behaviors of ultrafast electron dynamics in solids.

Intensity-dependence of excitonic third harmonic generation in bilayer MoS_2

5

The family of 2D TMDC semiconductors shows fascinating physical properties resulting from their reduced dimensionality and crystal symmetry, which are distinct from their bulk counterparts [102]. In the monolayer limit, the inversion symmetry breaking together with strong spin-orbit coupling governs the spin-valley properties and optical selection rules [99, 106]. Stacking hetero/homo single layers of TMDC on top of one another with a twist angle gives rise to tunable properties and may generate Moiré patterns, along with which novel quantum phenomena emerge [162]. Consequently, 2D TMDC form a basis for exotic spintronics [163], valleytronics [110, 164], and twistronics [165]. 2D TMDC also provide a platform to study many-body interactions, as an excited electron and hole forming an exciton is strongly confined in the plane and experiences decreased screening of the Coulomb interaction from the dielectric environment. The Coulomb attraction between the electron and the hole in 2D TMDC is one or two orders of magnitude stronger than in traditional quasi-2D systems such as GaAs or GaN quantum wells [166]. This leads to gigantic exciton binding energies E_{bind}, of typically a few hundred of meV [63, 64]. In contrast to the bulk counterpart, the excitons are observable even at room temperature and the excitonic effects are essential for the optical properties of 2D TMDC.

It is thus of fundamental importance to characterize the excitonic properties. First-principle calculations have predicted a diversity of strongly bound excitonic states [167]. A series of seminal experiments via linear one-photon absorption [63, 98], two-photon photoluminescence excitation [100, 168], and nonlinear wave-mixing spectroscopy [66] have revealed the characters of (s-like) bright and (p-like) dark excitons in layered TMDC. The reported E_{bind} of 2D TMDC via experimental measurements and theoretical predictions [98, 101, 167] are in the range of 200 - 500 meV and are sensitive to dielectric screening by the substrates. Also, dark excitons can be probed by various spectroscopic tools including two-photon excitation [66, 68, 100], magnetic brightening [169], and pump-probe measurements of intraexcitonic transitions [170, 171]. Presently, the attention paid to the many-body effects in the nonlinear optical response beyond the perturbative limit is growing [26, 72, 172–176]. It has been demonstrated that many-body effects can prominently enhance certain harmonics of HHG spectra in the extreme nonlinear regime [35, 69–72]. Furthermore, interactions of strong THz fields with excitons induce high-order sideband (HSB) emission [26, 172, 173], which results from subcycle ionization, acceleration, and recollision of excitonic electron-hole pairs. The weak intensity decay with increasing

sideband order confirms the nonperturbative nature of HSB. To date, the fundamental mechanism underlying the light-matter interaction with excitonic many-body effects is still under intensive investigation.

In this chapter, we consider the commonly fabricated 2H type of homobilayer TMDC and investigate excitonic third harmonic generation (THG) under rather weak excitations. Applying an in-plane static electric field has multiple effects on the excitonic properties which are only partly revealed by the linear absorption spectrum. On the one hand, an in-plane field breaks the in-plane symmetry of the exciton wave functions and induces hybridization of excitons of different orbitals [177] and a dc Stark shift of exciton energies [178, 179]. On the other hand, an in-plane field induces ionization of excitons into unbound electrons and holes [180, 181]. The static field induced exciton ionization is expected to decrease the THG yield. However, we observed a quite unusual field dependence of the THG yield in bilayer TMDC, i.e., the THG is enhanced by the static field when the exciton ionization is not yet significant. In the extremely weak optical excitation regime, the field dependence is similar to a previous experimental measurement of THG in bulk *GaAs* which has a small exciton binding energy [182]. Based on the perturbative expansion of the SBE in the optical field up to the third order, we clarify that the hybridization of exciton states and the Stark effects induced by the static field account for the slight increase of the THG yield. With increasing optical excitation intensity, an increasingly notable discrepancy between the computed THG and the perturbative third-order results indicates that higher-order effects influence the THG. In the perturbative approximation considering higher-order corrections and neglecting nonperturbative effects which are reasonable for moderate excitation intensities, we demonstrate that the fourth-, fifth-, and higher-order nonlinearities representing the bound-to-continuum-to-bound transitions are highly involved to determine the efficiency of the excitonic THG. Intraband excitations are found to play an important role in connecting the continuum and bound exciton states and provide significant modifications of the nonlinear optical response near the excitonic resonance in the presence of a static field.

5.1 Inter- and intraband excitations in the excitonic optical response

Working in the length gauge allows one to investigate the interplay between the inter- and intraband mechanisms underlying nonlinear optical phenomena [55]. As shown in the theoretical basis, see Chapter 2, the interband (intraband) excitations originate from the off-diagonal (diagonal) matrix elements of the position operator, and the macroscopic susceptibility is composed of the interband polarization and the intraband current. The intraband transition induces a temporal change of the electron wave vector $\mathbf{k}(t)$, which plays a significant role in the extreme nonlinear regime. An intense field with a frequency much smaller than the bandgap energy accelerates electrons in their bands over a wide range of $\mathbf{k}$ space, which prominently modifies the optical properties and the dynamics

on ultrafast timescales [25, 55, 56, 183, 184]. Moreover, for systems with strong excitonic effects, the intraband transition is a key mechanism that accounts for the optical response originating from intraexcitonic transitions [185, 186] and transitions between the bound and the continuum of unbound excitonic states [187, 188].

To elucidate the roles of inter- and intraband transitions in the optical response near the excitonic resonance under weak excitations, we make use of the perturbative expansion of the SBE [189, 190] including the Coulomb interaction on a Hartree-Fock level. For a system with inversion symmetry excited by a combination of optical $E_{opt}(t)$ and static E_{dc} fields, the optical response can be obtained by expanding microscopic quantities $X(\mathbf{k},t)$=$p(\mathbf{k},t)$, $n_{e/h}(\mathbf{k},t)$ in powers of the optical field as $X(\mathbf{k},t) = \sum_{m=0}^{\infty} X^{(m)}(\mathbf{k},t)$ with $X^{(m)} \propto {E_{opt}}^m$. The initial conditions are $p^{(0)}(\mathbf{k}, t = -\infty) = 0$ and ${n_{e/h}}^{(0)}(\mathbf{k}, t = -\infty) = 0$. In a two-band model with the interband polarization (electron-hole coherence) $p(\mathbf{k},t)$ and the electron/hole density $n(\mathbf{k},t) = n_e(\mathbf{k},t) = n_h(\mathbf{k},t)$, the perturbative expansion of the SBE in the optical field reads

$$\begin{aligned}
\frac{\partial}{\partial t}p^{(1)}(\mathbf{k},t) &= (-\frac{i}{\hbar}\omega(\mathbf{k}) - \frac{1}{T_2} + \frac{e}{\hbar}\mathbf{E}_{dc}\cdot\nabla_{\mathbf{k}})p^{(1)}(\mathbf{k},t) - 2\frac{i}{\hbar}\mathbf{d}(\mathbf{k})\cdot\mathbf{E}_{dc}n^{(1)}(\mathbf{k},t) \\
&\quad + \frac{i}{\hbar}\mathbf{d}(\mathbf{k})\cdot\mathbf{E}_{opt}(t) + \frac{i}{\hbar}\sum_{\mathbf{k}'} V_{\mathbf{k}-\mathbf{k}'}p^{(1)}(\mathbf{k}',t), \qquad (5.1)\\
\frac{\partial}{\partial t}n^{(1)}(\mathbf{k},t) &= \frac{i}{\hbar}\mathbf{d}(\mathbf{k})\cdot\mathbf{E}_{dc}(p^{*(1)}(\mathbf{k},t) - p^{(1)}(\mathbf{k},t)) + \frac{e}{\hbar}\mathbf{E}_{dc}\cdot\nabla_{\mathbf{k}}n^{(1)}(\mathbf{k},t), \qquad (5.2)
\end{aligned}$$

$$\begin{aligned}
\frac{\partial}{\partial t}p^{(m)}(\mathbf{k},t) &= (-\frac{i}{\hbar}\omega(\mathbf{k}) - \frac{1}{T_2} + \frac{e}{\hbar}\mathbf{E}_{dc}\cdot\nabla_{\mathbf{k}})p^{(m)}(\mathbf{k},t) - 2\frac{i}{\hbar}\mathbf{d}(\mathbf{k})\cdot\mathbf{E}_{dc}n^{(m)}(\mathbf{k},t) \\
&\quad + \frac{e}{\hbar}\mathbf{E}_{opt}(t)\cdot\nabla_{\mathbf{k}}p^{(m-1)}(\mathbf{k},t) - 2\frac{i}{\hbar}\mathbf{d}(\mathbf{k})\cdot\mathbf{E}_{opt}(t)n^{(m-1)}(\mathbf{k},t) \\
&\quad + \frac{i}{\hbar}\sum_{\mathbf{k}'} V_{\mathbf{k}-\mathbf{k}'}p^{(m)}(\mathbf{k}',t) - 2\frac{i}{\hbar}\sum_{j\le m} n^{(j)}(\mathbf{k},t)\sum_{\mathbf{k}'} V_{\mathbf{k}-\mathbf{k}'}p^{(m-j)}(\mathbf{k}',t), \qquad (5.3)\\
\frac{\partial}{\partial t}n^{(m)}(\mathbf{k},t) &= \frac{i}{\hbar}\mathbf{d}(\mathbf{k})\cdot\mathbf{E}_{dc}(p^{*(m)}(\mathbf{k},t) - p^{(m)}(\mathbf{k},t)) + \frac{e}{\hbar}\mathbf{E}_{dc}\cdot\nabla_{\mathbf{k}}n^{(m)}(\mathbf{k},t) \\
&\quad + \frac{i}{\hbar}\mathbf{d}(\mathbf{k})\cdot\mathbf{E}_{opt}(t)(p^{*(m-1)}(\mathbf{k},t) - p^{(m-1)}(\mathbf{k},t)) + \frac{e}{\hbar}\mathbf{E}_{opt}(t)\cdot\nabla_{\mathbf{k}}n^{(m-1)}(\mathbf{k},t) \\
&\quad + \frac{i}{\hbar}\sum_{j\le m}(p^{*(j)}(\mathbf{k},t) - p^{j)}(\mathbf{k},t))\sum_{\mathbf{k}'} V_{\mathbf{k}-\mathbf{k}'}p^{(m-j)}(\mathbf{k}',t). \qquad (5.4)
\end{aligned}$$

The static electric field appears in the first line of each equation and does not couple different orders in the optical field. It leads to temporal change in the wave vector $\hbar\dot{\mathbf{k}}(t) = -e\mathbf{E}_{dc}$ and couples $p^{(m)}(\mathbf{k},t)$ and $n^{(m)}(\mathbf{k},t)$ ($m \geq 1$). $n^{(1)}(\mathbf{k},t)$ is non-vanishing only in the presence of the static electric field which results from the symmetry breaking in the time-dependent dynamics. In first order in the optical field, the interband excitation induced by the optical field initiates the entire dynamics. For higher orders of $p^{(m)}(\mathbf{k},t)$ ($m > 1$), the

intraband excitation is built up with the source term proportional to $p^{(m-1)}(\mathbf{k}, t)$ and the interband excitation proportional to $n^{(m-1)}(\mathbf{k}, t)$. The perturbative expansion of the SBE is an effective approach to quantitatively distinguish the inter- and intraband excitation pathways when the excitation intensity is sufficiently weak [189, 190]. With increasing excitation intensity, higher-order nonlinearities may increasingly contribute to the signal of harmonic generation provided by lower orders. The differences of the computed signals between solving the full equations and solving the perturbative expansion with considering higher-order corrections are known as nonperturbative effects.

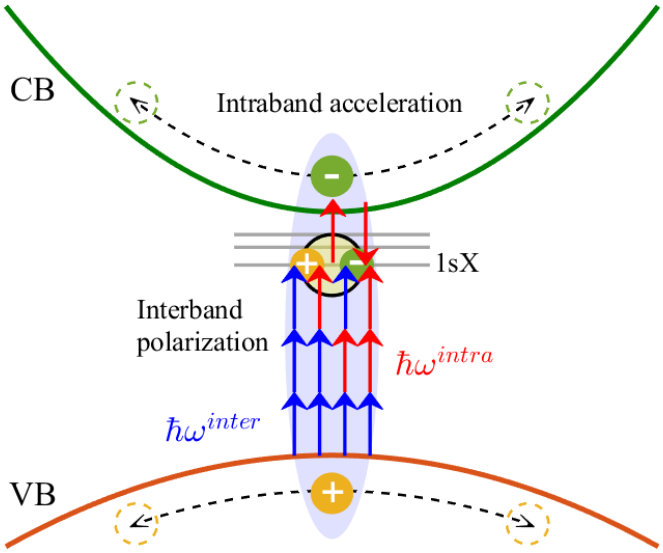

Figure 5.1: Schematic illustration of the multiphoton transition for excitonic systems considering a resonant three-photon excitation of the 1s exciton. The interband excitation initiates the first-order polarization and the coupled interband and intraband excitations contribute to the second- and third-order polarizations. In higher orders, the intraband transitions connect the bound exciton and the unbound continuum states.

Figure 5.1 depicts the excitation pathways for a system driven by an oscillating field that is three-photon resonant with the 1s exciton state. According to the perturbative expansion of the SBE, in the process of a three-photon transition from the ground state to the 1s exciton state, the interband excitation contributes to all three orders and the intraband excitation contributes in the second and third orders of $p_{\mathbf{k}}^{(m)}$ and $n_{\mathbf{k}}^{(m)}$ $(m > 1)$. The transitions between the exciton and the continuum states are possible via higher orders of intraband excitation [187, 188]. The intraband acceleration in the continuum gives rise to the modifications in the $\mathbf{k}$-resolved $p_{\mathbf{k}}^{(m)}$ $(m \geq 4)$ and consequently influences the intraband transitions from the continuum to the exciton states. The process of the bound-to-continuum-to-bound intraband transitions is analogous to the picture underlying the excitonic high-order sideband generation, i.e., an electron is ripped from an exciton and recollides with the left-behind hole driven by an intense THz field [26, 172, 173].

5.2 Exciton landscape of bilayer MoS_2

This homobilayer TMDC consists of two monolayers van der Waals bonded and stacked by rotating 180° with respect to one another and is centrosymmetric. The unit cell of the monolayer is a X-M-X covalently bonded hexagonal lattice with the chemical composition of MX_2, where M stands for the metal atom W or Mo and X is S or Se. The intrinsic in-plane optical properties of such monolayers arising from the inversion symmetry breaking are not present in the homobilayer. The homobilayer TMDC features layer degree of freedom and layer-spin polarization [164] and are thus often chosen to study topological valley transport [107, 191] and magnetoelectric effects [192, 193] by applying a perpendicular electric field. We concentrate on the excitonic effects in homobilayer MoS_2 excited by in-plane polarized fields. The homobilayer MoS_2 possesses a direct bandgap with both the conduction band minimum and the valence band maximum located at the corners of the **k** space (K points), which is as in a monolayer. In contrast to the non-equivalence of two valleys K/K' points and an amount of band splitting resulting from the lifted spin degeneracy in a monolayer, the bands of a MoS_2 bilayer are spin-degenerate throughout the entire **k** space with equivalent K valleys. We perform the band structure calculation based on DFT with generalized gradient approximations (GGA) and implement the multiband TPT gauge in the zigzag direction which ensures smoothness of the eigenfunctions along the direction of the linearly polarized optical and static electric fields in the following calculations. The resulting **k**-dependent transition energy between the uppermost valence band and the bottommost conduction band is shown in Figure 5.2. The peak value of the interband dipole matrix element at valley K is 0.153 *e nm*.

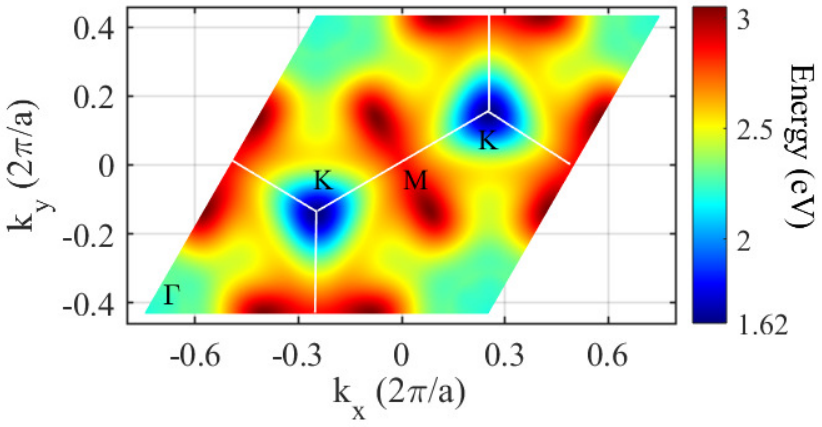

Figure 5.2: Interband transition energy of the bilayer MoS_2 between the uppermost valence and bottommost conduction bands. The white lines denote the boundary of the hexagonal BZ and high symmetry k points are labeled with Γ, *K*, and *M*. The minimum transition energy, i.e., the band gap, 1.62 *eV* is located at K.

The exciton properties of a material strongly depend on the dielectric environment. A dielectric model for the determination of the effective Coulomb interaction and screening

has been developed [194]. Using this dielectric model, we compute the Coulomb matrix elements of a freestanding bilayer MoS_2 with the Coulomb potential considering the background dielectric parameter of the vacuum. The exciton dephasing time in semiconductors is associated with the dynamics of electron-phonon scattering and Coulomb scattering for higher excitation intensities [195]. Thus, the exciton dephasing rate depends on temperature and the excitation regime [196]. To determine the linear absorption, we solve the SBE using an in-plane polarized field with an extremely short duration and the dephasing time in the SBE is assumed as 100 fs which provides a good spectral resolution of the bright excitons. The spectral absorption is proportional to the imaginary part of the ratio between the Fourier-transformed macroscopic polarization and the optical electric field [73], i.e.,

$$\alpha(\omega) \propto Im[\frac{\mathbf{e} \cdot \mathbf{P}(\omega)}{E(\omega)}] \tag{5.5}$$

where **e** denotes the polarization direction of the optical pulse and the pulse spectrum $E(\omega)$ is broad enough to cover the exciton and continuum energies. The resulting linear absorption spectra for the freestanding bilayer MoS_2 with and without the Coulomb interaction are displayed in Figure 5.3. The linear absorption provides the landscape of excitons, resembling the Rydberg series in hydrogen atoms. For bilayer MoS_2, we get $E_{1s} = 1.258\ eV$ and $E_{bind} = 362\ meV$. The obtained binding energy is in reasonable agreement with various reported experimental and theoretical data for layered TMDC [101]. The energies of the bandgap and the excitons are underestimated due to the GGA of exchange-correlation functional in DFT calculations [197] and they are shifted by constant energy, known as the scissors correction [198], to match experimental measurements.

An in-plane static electric field breaks the symmetry of the system and induces hybridization of exciton wave functions with different symmetries. As a result, new exciton states are formed which are superpositions of the original bright and dark exciton states [177, 199]. Different excitons react differently to the static fields which depends on the exciton energy and the spatial extent. It has shown that for a monolayer TMDC, 2s, 2p, and higher exciton orbitals are efficiently hybridized while the 1s exciton is preserved with slight changes in a low static field regime [177]. The energies and wave functions of the mixed excitons can be evaluated by diagonalizing the Hamiltonian including the electric field in the basis of unperturbed exciton states. The resulting exciton energies are shifted compared to the original ones, which is known as the dc Stark shift [200–202]. The dc Stark shift depends on the dipole moments between different states and can be expanded in powers of the applied electric field [178, 179]. In the weak field limit, the dc Stark shift for the excited states which primarily possess s symmetry of hydrogen- and helium-like atoms is proportional to ${E_{dc}}^2$ [200, 201]. For monolayer TMDC, the Stark shift of the 1s exciton shows a quadratic behavior for fields up to 0.1 MV/cm, but it exceeds the quadratic scaling for larger electric field amplitudes [203]. Here, we investigate the excitonic Stark effect in bilayer TMDC induced by an in-plane static electric field. Figure 5.3 displays the

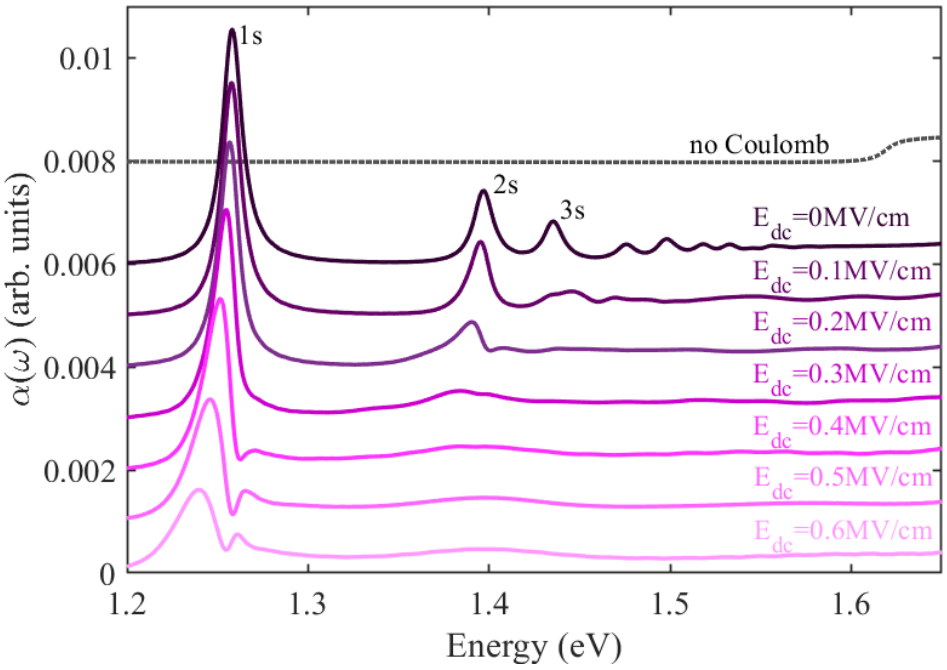

Figure 5.3: Calculated linear absorption spectra for the freestanding bilayer MoS_2. The dashed curve is the result obtained without including Coulomb interaction and no static field showing a step-like absorption starting at the band edge (1.62 eV). The solid curves are the results obtained with Coulomb interaction for various static electric field amplitudes showing strongly absorbing discrete excitonic peaks below the band edge. The lowest peak with the strongest absorption is the 1s exciton which exhibits a redshift, a reduced absorption, and a spectral broadening due to exciton ionization with increasing static electric field strength. The 2s and 3s exciton states show the same behaviors as the 1s exciton state but with increased strengths. All curves are shifted vertically for clarity.

linear absorption spectra for several static electric field amplitudes where all exciton peaks exhibit redshifts which are dependent on the field amplitude. The energy shift of the 1s exciton (actually the newly formed exciton with the lowest energy which inherits mostly the characters of the unperturbed 1s exciton) peak as a function of the static electric field amplitude is shown in Figure 5.4 which can be fitted by the sum of a quadratic dependence and hyperpolarizability corrections, i.e.,

$$\delta E_{1s} = \alpha {E_{dc}}^2 + \beta {E_{dc}}^4 + \gamma {E_{dc}}^6, \tag{5.6}$$

with the fitting parameters $\alpha = 34.4\ meV(cm/MV)^2$, $\beta = 0.4472\ meV(cm/MV)^4$, and $\gamma = 0.00172 meV(cm/MV)^6$, where due to symmetry only even-order corrections in field appear. The quadratic dependence is sufficient to describe the dc Stark shift at low static

fields, which is consistent with the perturbative regime [203]. The non-vanishing factors of the hyperpolarizabilities are related to higher-order dipole moments [178, 204].

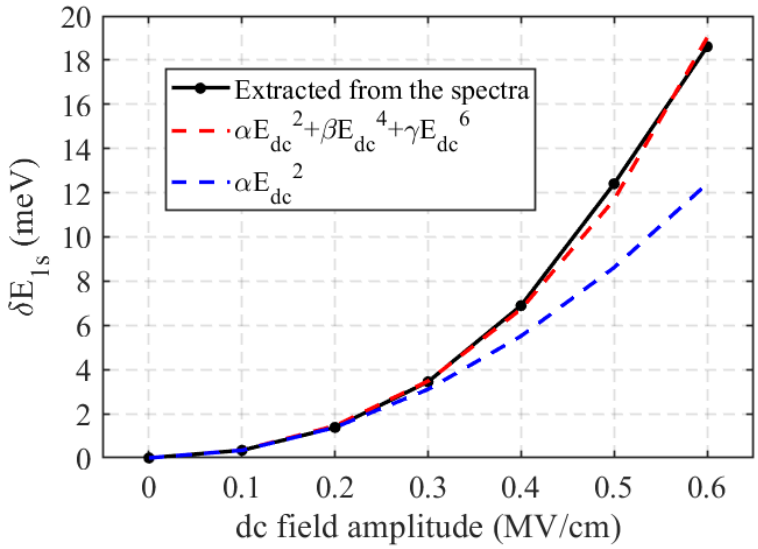

Figure 5.4: Static electric field dependence of the Stark shift δE_{1s}. The solid curve represents computed data extracted from the linear absorption spectra of Figure 5.3, whereas the dashed lines denote the fitting functions with the coefficients given in the main text.

In addition, an electric field tears the electron and hole apart, leading to the ionization of excitons into unbound electrons and holes which reduces the lifetime of the excitons [180, 181]. As a result, the linear absorption spectrum is modified as the exciton peaks are spectrally broadened and the absorption peak of the excitons is suppressed. In our results, the spectral width increases and the peak absorption decreases monotonically with increasing static fields for all excitons. In the low field range, due to their smaller energy differences, the absorption peaks of the 2s and higher exciton orbitals are significantly broadened and almost merge at $E_{dc} = 0.3\ MV/cm$ due to the ionization together with the hybridization. At higher static fields, a new peak near the 1s exciton is formed which is a signature of the field-dependent excitonic absorption in the Wannier-Stark regime [205, 206].

The in-plane static field induced hybridization of the excitons brightens p-like exciton states which are forbidden without a symmetry-breaking static field. To resolve the p-like exciton states, a longer dephasing time of $400 fs$ is used in the simulations. It should be noted that the dephasing rate can be adjusted in calculations to reach a desired spectral resolution. Figure 5.5 shows the resulting linear absorption spectra around the 2s exciton resonance. The graphic is split into two parts to show different regions of the absorption intensity for clarity. Due to the large energy differences, 1s and 3s exciton states are the

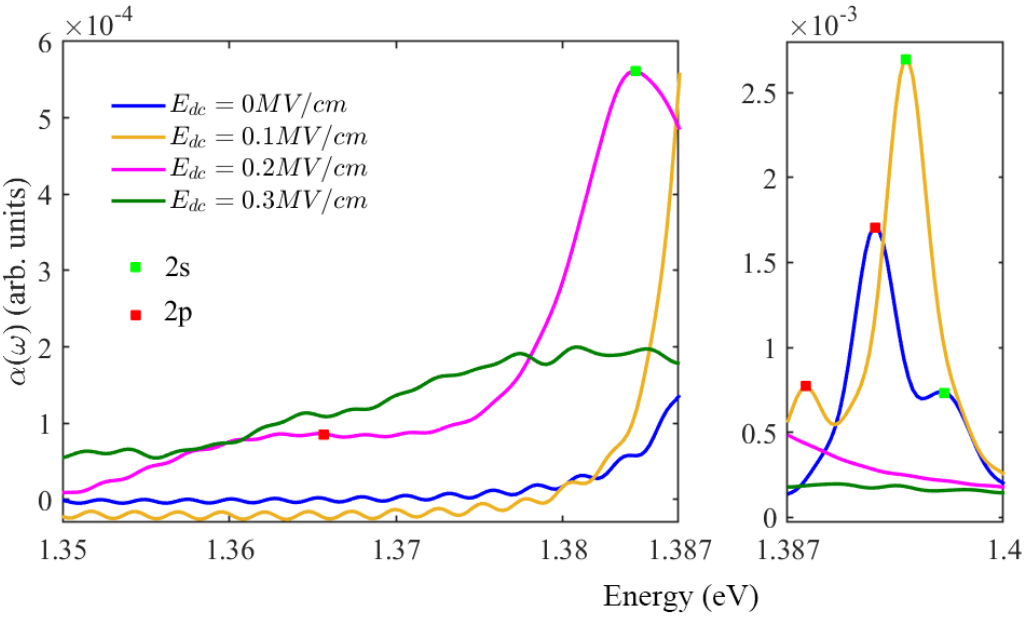

Figure 5.5: Linear absorption spectra around the 2s exciton state for different static field amplitudes. The green (red) rectangles denote the absorption peaks of hybridized 2s (2p) exciton peaks. In the case of $E_{dc} = 0\ MV/cm$, the symmetry of the dipole matrix element is artificially broken in the simulation so that the absorption of the 2p state appears stronger than that of the 2s state.

least involved in the hybridization for the chosen static field amplitude. The result for $E_{dc} = 0$ is artificial as the dipole matrix element is partially zeroed near the K point in the calculation, but this allows for the identification of the 2p resonance without dc Stark effects. The green (red) rectangles denote the peaks of the hybridized exciton states which are evolved from the 2s (2p) state. In the presence of the static field, the discrete mixed exciton state with the stronger peak and higher energy emerges with the largest projection coefficient on the basis of the 2s state up to $E_{dc} = 0.2\ MV/cm$. The weaker exciton state with lower energy is mainly composed of the 2p state which has a higher ionization rate as it is broadened to a plateau at $E_{dc} = 0.2\ MV/cm$. At $E_{dc} = 0.3\ MV/cm$, the efficient hybridization of the 2s and 2p exciton states and the exciton ionization leads to the weak merged absorption.

5.3 Excitonic third harmonic generation

In linear optics, the interband dipole transition is responsible for a series of exciton peaks and the constant absorption in the continuum range. In the non-resonant excitation regime, the coupling of inter- and intraband transitions significantly influences the nonlinear

optical response [183, 184]. Without considering excitonic effects, the below-gap harmonic generation is Kerr-type which is quantitatively perturbative [34] even in the strong field regime. It is associated with the buildup of a quasi-instantaneous interband polarization which comprises two steps of the photon absorption and the immediate transition to the ground state [34, 207]. In low-dimensional materials, the strong electron-hole Coulomb attraction which forms stable excitonic levels below the band edge is expected to lead to a distinctive influence on the low-order harmonics. However, the underlying mechanism has so far not well been studied.

To analyze excitonic effects on harmonic generation below the band edge based on microscopic theory, we perform simulations of THG from bilayer MoS_2. We apply an optical field linearly polarized along the zigzag direction which is three-photon resonant with the 1s exciton, i.e., $3\hbar\omega_0 = E_{1s}$. The pulse has a Gaussian envelope with a FWHM of 100 fs. An additional in-plane static electric field is applied parallel to the optical field to investigate the effect of symmetry breaking and exciton ionization on the THG. The comparison of the THG yield between solving the full SBE and the perturbative expansion of the SBE as a function of the static electric field amplitude with the optical field amplitude varied from $E_{opt} = 0.6\ MV/cm$ to $2.5\ MV/cm$ are presented in Figure 5.6 where $|P_{3\omega_0}|$ is the excitonic THG peak. Remarkably, with increasing optical field amplitude, the difference between the perturbative expansion up to the third order and the full calculation gets more pronounced, suggesting that higher-order corrections are increasingly relevant. For all considered optical field amplitudes, the THG yield depends non-monotonically on the static electric field in both approaches of the calculations. As evident by the spectral broadening and the suppression of the linear excitonic absorption peaks starting from very weak field amplitudes shown in Figure 5.3, the exciton ionization occurs once a static electric field is present. Unexpectedly, the THG yield increases with the amplitude of the static electric field for weak static electric fields. This indicates that other effects may occur in the process of THG and dominate over exciton ionization in this field range. In the full calculation, the increase grows and the static field where the THG yield is maximal shifts to higher values with increasing optical field amplitude (see the comparison of the normalized THG yield in Figure 5.7(a)). In contrast, the static field dependence of the perturbative third-order results is independent on the optical field amplitude and the maximum at $E_{dc} = 0.2\ MV/cm$ is increased by only 0.738% (see Figure 5.7(b)). At high static field amplitudes, the THG yield steeply declines as the exciton ionization dominates. The ionization rate is identical for all considered optical field amplitudes in both calculations (all lines in the declining regions in Figures 5.6 and 5.7 have the same slope).

First of all, we verified that under the considered excitation conditions, the density is always low. Therefore, the contribution of interband excitations proportional to $\mathbf{d}(\mathbf{k}) \cdot \mathbf{E}_{opt}(t)n(\mathbf{k})$ is insignificant and the THG is dominated by the interband polarization $P(3\omega_0)$ as the intraband current is extremely weak. Figure 5.8 shows the comparison between the full calculation and the pure interband model for $E_{opt} = 1.5\ MV/cm$. In the pure interband model, the optical field induced intraband excitations proportional to $\mathbf{E}_{opt}(t)\nabla_{\mathbf{k}}$ are switched off in the SBE. The THG yield induced by the pure interband excitation is much lower than that generated by the coupled inter- and intraband excitations and it

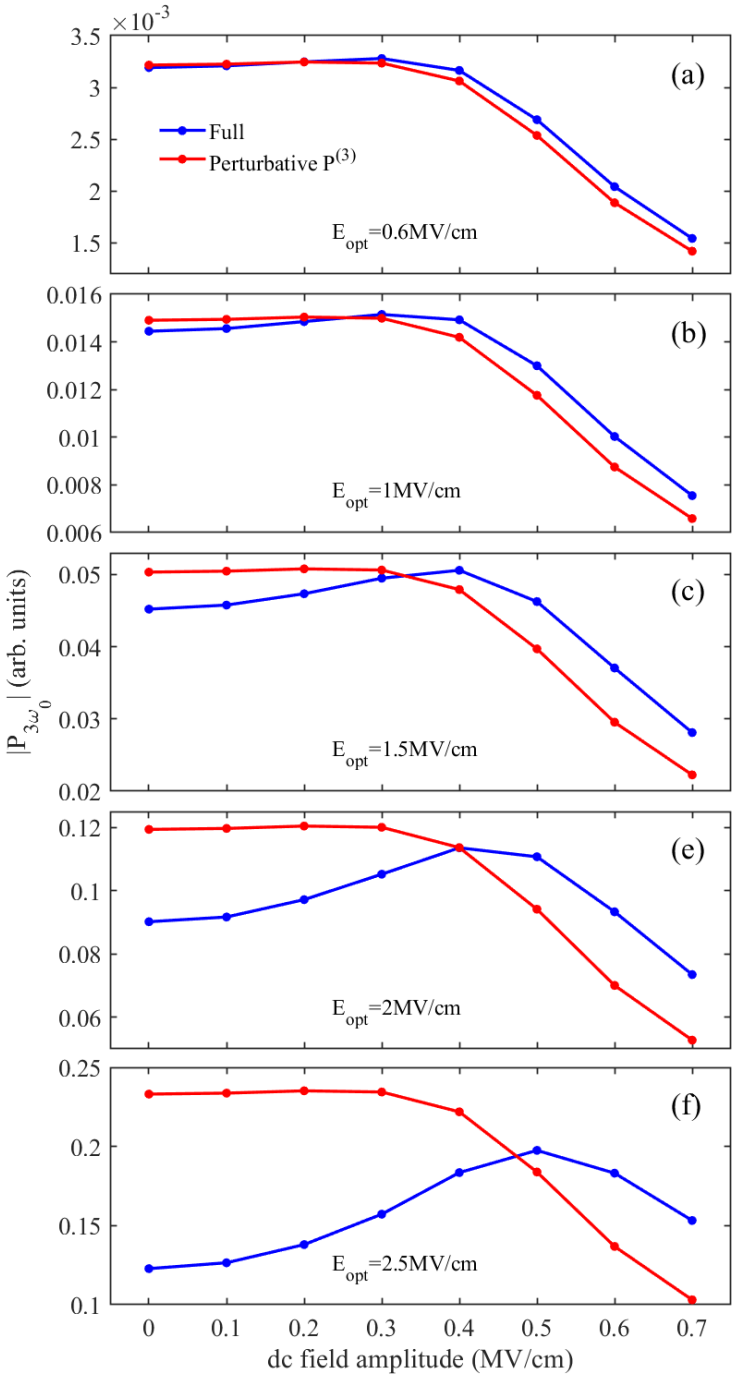

Figure 5.6: Static electric field dependence of the THG peak obtained from fully solving the SBE (blue curves) and performing a perturbative expansion up to the third order (red curves) for optical field amplitudes (a) $E_{opt} = 0.6\ MV/cm$, (b) $E_{opt} = 1\ MV/cm$, (c) $E_{opt} = 1.5\ MV/cm$, (d) $E_{opt} = 2\ MV/cm$, and (e) $E_{opt} = 2.5\ MV/cm$.

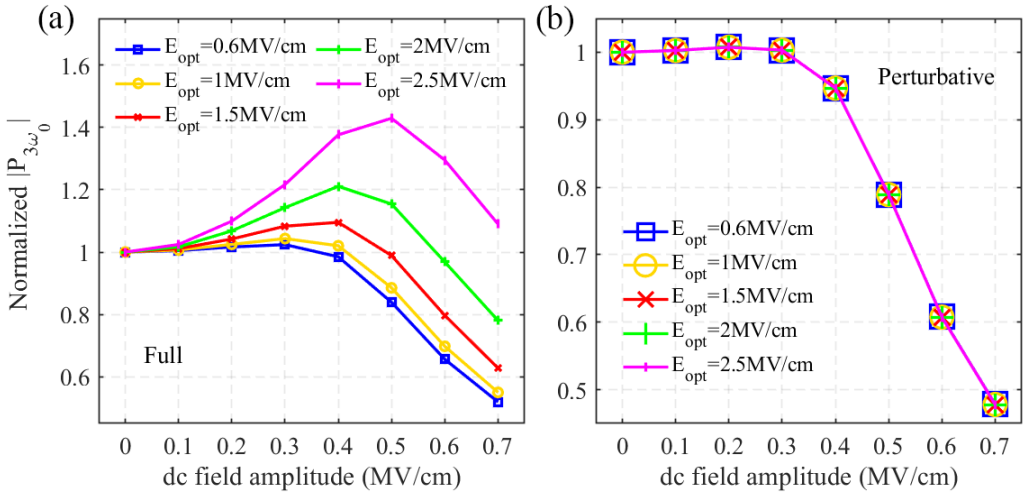

Figure 5.7: Normalized THG yield as a function of the static electric field amplitude obtained from (a) the full calculation and (b) the perturbative expansion of the SBE up to the third-order for optical field amplitudes shown in Figure 5.6. In the full calculation, the increase of the THG yield at low static fields grows with the optical field. For the perturbative third-order results, the increase is independent on the optical field amplitude. All lines in (b) are identical with the maxima 1.00738 at $E_{opt} = 0.2\ MV/cm$.

decreases monotonically with the static electric field. This suggests that the intraband excitation largely dominates over the interband excitation beyond the linear order. Besides, we verified that the coupling between $p^{(m)}(\mathbf{k})$ and $n^{(m)}(\mathbf{k})$ $(m \geq 1)$ by the static electric field is negligible as the results are nearly unchanged when switching off this coupling in the SBE.

In the third-order results, the THG exhibits a rather delicate increase at low static electric fields, hiding the feature of exciton ionization which decreases the THG for higher fields. A similar behavior has been observed for the THG generated in *GaAs* where the nonlinearity of the 1s exciton resonance is modified by the electric field [182]. This change is attributed to the electric field induced Stark effect which mixes the 1s and 2p exciton states of different parity. In our case, we speculate that the increase of the THG below $E_{dc} = 0.3\ MV/cm$ in the third-order results may originate from the dc Stark shifts of the excitons. As given by the analytical expression for the second-order susceptibility in terms of generalized derivatives of the exciton Green's function [208], the resulting nonlinearities of each order are inversely proportional to the detuning of the excitation energy with respect to the exciton energy. In the low static field range, the dc Stark shift of the excitons is very small compared to the detunings and therefore impacts the optical response only weakly. For static electric fields that do not fully ionize the hybridized excitons, the second-order excitation

$$p^{(2)}(\mathbf{k}) \propto \sum_{m,n} \frac{1}{E_m(\hbar\omega_0 - E_m)(2\hbar\omega_0 - E_n)} \tag{5.7}$$

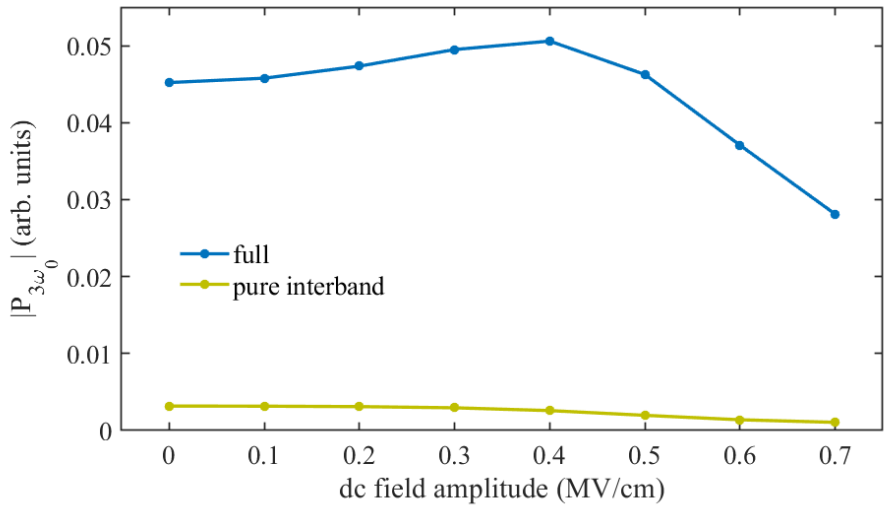

Figure 5.8: Comparison of the static electric field dependence of the THG yield between the full calculation (blue curve) and the pure interband model in which the **k**-gradient terms in the SBE are turned off (yellow curve) for an optical field amplitude $E_{opt} = 1.5\ MV/cm$.

increases with increasing field amplitude primarily due to the redshift of the hybridized 2p exciton state. Consequently, the third-order nonlinearity is faintly enhanced via the intraband excitation, i.e., $p^{(3)}(\mathbf{k}) \propto \mathbf{E}_{opt}(t) \cdot \nabla_{\mathbf{k}} p^{(2)}(\mathbf{k})$. This explains why the maximum of the THG occurs at $E_{dc} = 0.2\ MV/cm$ in the third-order results.

The difference of the THG yields between the full calculation and the perturbative third-order results at low static fields gets larger with increasing optical field amplitude, which is attributed to higher-order corrections of the excitonic THG. The transition to the continuum is achieved via a four-photon excitation since $\hbar\omega_0 = 0.419\ eV$ is just larger than E_{bind}. Within a perturbative description, the components of the fifth- and higher-odd-order nonlinearities representing the transitions from the continuum to the 1s exciton state contribute to the excitonic third harmonic. In the process of these transitions, due to the optical field induced intraband oscillation in the continuum, the intermediate continuum state does not exactly have the energy $n\hbar\omega_0$ ($n \geq 4$) but actually contributes within an energy window. The shift of the wave vector induced by the optical field is $0.7\% \sim 2.6\%$ of the BZ for the considered excitation conditions, which is at a rather low level to induce a significant modification on the THG. Figure 5.9 shows the THG yield computed with no static field as a function of the optical field amplitude which is normalized to the case of $E_{opt} = 0.6\ MV/cm$. It is well fitted by a function in terms of the $3rd$, $5th$, and $7th$ powers of the optical field amplitude with the fitting parameters $\alpha = 4.7044\ cm^3/(MV)^3$, $\beta = -0.1383\ cm^5/(MV)^5$, and $\gamma = -0.0395\ cm^7/(MV)^7$, respectively. This implies that the fifth- and seventh-order nonlinearities reduce the third harmonic. The sign of γ is inconsistent with the simple prediction of the parity and sign by the relation, i.e., $p^{(m)}(\mathbf{k}) \propto$

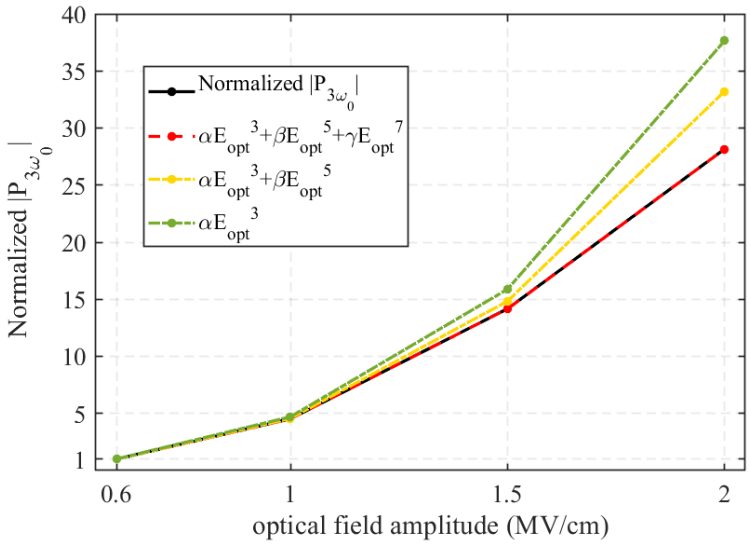

Figure 5.9: THG yield as a function of the optical field amplitude normalized to that at $E_{opt} = 0.6\ MV/cm$ (black line) and the fitting functions in terms of third, fifth, and seventh order powers of the optical field amplitude.

$\mathbf{E}_{opt}\nabla_{\mathbf{k}}p^{(m-1)}(\mathbf{k})$ $(m > 1)$. This is possibly linked to the time-varying energy due to the intraband oscillation along the dispersive bands when solving the SBE which influences the $\mathbf{k}$-dependent $p^{(m)}(\mathbf{k})$ $(m \geq 4)$. Particularly, the excitation to more dispersive regions of the band structure possibly makes the sign of higher-order contributions at the third harmonic flip. In the following, we analyze the static field dependence in the perturbative approximation where the dominant higher-order corrections, i.e., the fourth and fifth-order nonlinearities are considered which account for the bound-to-continuum-to-bound transitions near the band edge. The influence of the intraband oscillation induced by the optical field on the $\mathbf{k}$-dependent $p^{(m)}(\mathbf{k})$ $(m \leq 5)$ is negligible.

We extend the perturbative expansion of the SBE to the fifth order for $E_{opt} = 1.5\ MV/cm$. The resulting $\mathbf{k}$-resolved $P^{(3)}(\mathbf{k})$, $P^{(4)}(\mathbf{k})$, and $P^{(5)}(\mathbf{k})$ $(P^{(m)}(\mathbf{k}) = Re[d(\mathbf{k})p^{(m)}(\mathbf{k})])$ at a particular time point where the $P^{(3)}(\mathbf{k})$ is maximal in the central optical cycle are shown in Figure 5.10. The corresponding $\mathbf{k}$-resolved and $\mathbf{k}$-integrated results in the frequency domain are shown in Figure 5.11. Since the real-space extent of the exciton wave functions is much larger than the size of the unit cell, the $\mathbf{k}$-resolved polarizations near the 1s exciton resonance are tightly localized in the K valley of bilayer TMDC [99, 100]. Looking at the spectra around the third harmonic, the modulus of the fifth-order nonlinearity $|P^{(5)}(3\omega_0)|$ is significant and thus contributes to the THG. The magnitude of $P(3\omega_0) = P^{(3)}(3\omega_0) + P^{(5)}(3\omega_0)$ is close to the computed THG in the full calculation with a slight deviation due to the omission of even higher-order corrections. Adding the fifth-order nonlinearities leads to $|P(3\omega_0)| < |P^{(3)}(3\omega_0)|$ at $E_{dc} = 0$ and $|P(3\omega_0)| > |P^{(3)}(3\omega_0)|$ at $E_{dc} = 0.4\ MV/cm$, which are the same as in the full calculation for $E_{opt} = 1.5\ MV/cm$.

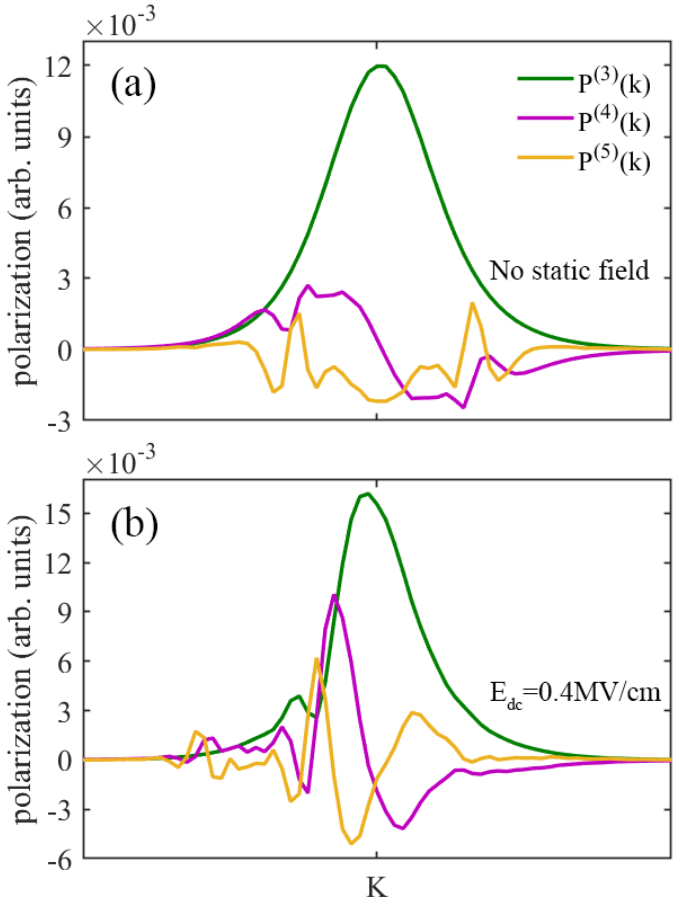

Figure 5.10: **K**-resolved $P^{(3)}(\mathbf{k})$ (green curves), $P^{(4)}(\mathbf{k})$ (purple curves), and $P^{(5)}(\mathbf{k})$ (yellow curves) in a portion of the BZ (17.5%) for a 1D k-path along the zigzag direction passing through the K point for $E_{dc} = 0$ in (a) and $E_{dc} = 0.4\ MV/cm$ in (b) with the optical field amplitude $E_{opt} = 1.5\ MV/cm$ at the time instant where $P^{(3)}(\mathbf{k})$ is maximal in the central optical cycle.

To better compare the cases $E_{dc} = 0$ and $E_{dc} = 0.4\ MV/cm$ in the frequency domain, $P^{(3)}(\mathbf{k}, \omega)$ and $P^{(5)}(\mathbf{k}, \omega)$ around $3\omega_0$ shown in Figure 5.11 are rotated by a same phase to ensure $Im[P^{(3)}(\mathbf{k}, \omega)] + Im[P^{(5)}(\mathbf{k}, \omega)] = 0$ so that the contribution of the fifth-order nonlinearity on the THG can be analyzed by focusing on the real part.

As shown in Figure 5.10(a), without the static electric field, $P^{(3)}(\mathbf{k})$ in the time domain has a peak at the K point with a Lorentz-like envelope in $\mathbf{k}$ space since the 1s exciton is excited resonantly. $P^{(4)}(\mathbf{k})$ is anti-symmetric with respect to $\mathbf{k}$ and $P^{(5)}(\mathbf{k})$ has a peak at the center with a negative sign and two side peaks with positive signs. The parities and signs of $P^{(4)}(\mathbf{k})$ and $P^{(5)}(\mathbf{k})$ are consistent with the simple prediction based on $p^{(m)}(\mathbf{k}) \propto \mathbf{E}_{opt} \cdot \nabla_{\mathbf{k}} p^{(m-1)}(\mathbf{k})$ $(m > 1)$. The perturbative $P^{(3)}(\mathbf{k})$ and $P^{(5)}(\mathbf{k})$ are of opposite signs near the K point (see Figure 5.11(a)), which implies a destructive interference

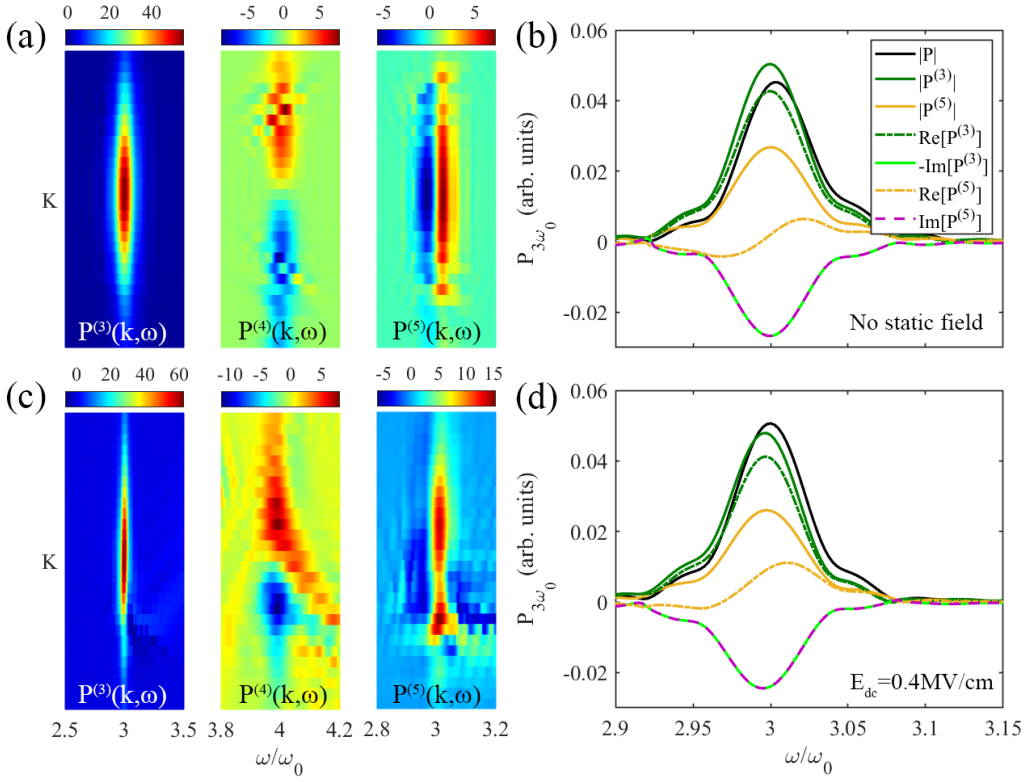

Figure 5.11: Real part of the k-resolved perturbative $P^{(3)}(k, 3\omega_0)$, $P^{(4)}(k, 4\omega_0)$, and $P^{(5)}(k, 3\omega_0)$ obtained by Fourier transforming the time-dependent polarization in a portion of the BZ (7.5%) centered at the valley K for (a) $E_{dc} = 0$ and (c) $E_{dc} = 0.4\ MV/cm$ for an optical field amplitude $E_{opt} = 1.5\ MV/cm$. (b) (d) The corresponding k-integrated polarization by the full calculation (black curve) and the perturbative $P^{(3)}(3\omega_0)$ and $P^{(5)}(3\omega_0)$ with the absolute, real and imaginary values shown.

between these two components. At $E_{dc} = 0.4\ MV/cm$ where the THG yield is maximal, the envelope of $P^{(3)}(\mathbf{k})$ remains basically unchanged due to the mainly unchanged exciton resonance. The slightly reduced width and the minor distortion of $P^{(3)}(\mathbf{k})$ away from the K point arises from the static field induced hybridization of the 1s exciton and higher exciton states [177, 209]. However, $P^{(4)}(\mathbf{k})$ and $P^{(5)}(\mathbf{k})$ are strongly modulated (see Figure 5.10(b)). The static field induces intraband acceleration in the continuum which makes $P^{(4)}(\mathbf{k})$ oscillating with a broader range of frequency near $4\omega_0$ (see Figure 5.11(c)). The wave functions of the unbound electrons and holes thereby acquire a dynamical phase shift which is a time integral over the change of energy [56]. The modification of $P^{(5)}(\mathbf{k})$ is almost synchronized with $P^{(4)}(\mathbf{k})$ without other remarkable changes induced by the static field. Importantly, one side peak with a positive sign of $P^{(5)}(\mathbf{k})$ seen at $E_{dc} = 0$ shifts towards the K point. This leads to constructive interference between $P^{(3)}(\mathbf{k})$ and $P^{(5)}(\mathbf{k})$ near the K point which predominantly influences the excitonic response. In the frequency domain, $Re[P^{(5)}(\mathbf{k}, 3\omega_0)]$ relative to $Re[P^{(3)}(\mathbf{k}, 3\omega_0)]$ is larger at $E_{dc} = 0.4\ MV/cm$ than at

$E_{dc} = 0$. As a result, compared to $|P^{(3)}(3\omega_0)|$, $|P(3\omega_0)|$ is reduced at $E_{dc} = 0$ but enhanced at $E_{dc} = 0.4\ MV/cm$.

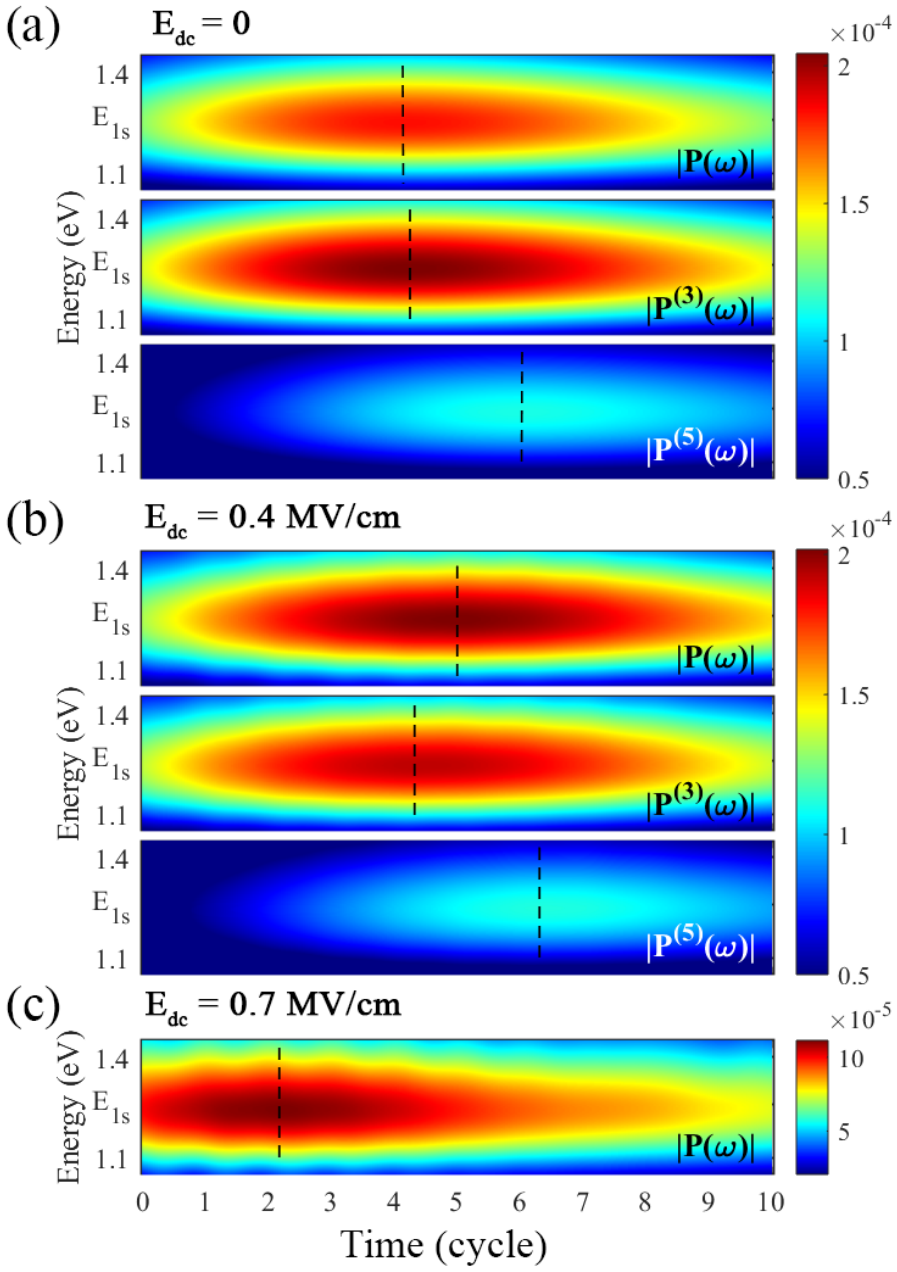

Figure 5.12: Time-energy map for the THG obtained from the perturbative expansion for (a) $E_{dc} = 0$, (b) $E_{dc} = 0.4\ MV/cm$, and (c) $E_{dc} = 0.7\ MV/cm$ for an optical field amplitude $E_{opt} = 1.5\ MV/cm$. The dashed lines denote the temporal peaks of the spectra.

Thus, the enhancement of the THG by the static field is well understood within the

perturbative approximation. With increasing optical field, the higher-order nonlinearities rise and therefore contribute to the lower harmonics. The static field mainly modifies the nonlinearities in the continuum in the fourth order and correspondingly the higher-order contributions near the excitonic resonance. The interference between the third- and the higher-order excitations continuously shifts from destructive towards constructive with increasing static field amplitude. A turning to a destructive interference may occur at even higher static fields but at some point the process of the exciton ionization prevails which sharply decreases the THG yield. It can be expected that the transitions between the exciton and continuum states become intricate at even higher optical fields as higher orders of the excitations are involved and nonperturbative effects may come into play.

Figure 5.12 presents a timing analysis of the THG for the cases discussed above with the dashed lines marking the time position of the signal maxima. The peaks of the signals at the excitonic resonance are several cycles retarded with respect to the field crest ($t = 0$), which is the result of the long exciton dephasing time (the duration of the pulse is $\frac{t_{FWHM}}{T_{opt}} \approx 10$). This is distinctly different from instantaneous non-resonant optical nonlinearities when exciting below the bandgap. Without significant exciton ionization (see Figs. 5.12 (a) and (b)), the global temporal profile of the perturbative $|P^{(3)}(3\omega_0)|$ is nearly unaffected by the static field with the peaks around four cycles delayed with respect to the field crest. The peaks of $|P^{(5)}(3\omega_0)|$ are around two cycles delayed with respect to the peaks of $|P^{(3)}(3\omega_0)|$. This is commonly understood as that integrating $\mathbf{E}_{opt}(t) \cdot \nabla_{\mathbf{k}} p^{(m)}(\mathbf{k}, t)$ over time leads to the delay in the temporal envelope of higher-order polarizations compared to that of lower orders. In addition, $|P^{(5)}(3\omega_0)|$ is more delayed in the presence of the static field. As discussed above, the static field induces hybridization of the exciton states which slightly modifies $P^{(3)}(\mathbf{k})$ and drives intraband acceleration in the continuum which modifies the $\mathbf{k}$-resolved $P^{(4)}(\mathbf{k})$. As shown in Figure 5.10, in spite of the significant change in the $\mathbf{k}$-dependent amplitude, $P^{(4)}(\mathbf{k})$ and $P^{(5)}(\mathbf{k})$ exhibit a prominent shift in $\mathbf{k}$ space for $E_{dc} = 0.4\ MV/cm$. From a perspective of field-driven ionization, acceleration, and recombination of excitonic electron-hole pairs [26, 172], this $\mathbf{k}$ shift prolongs the time of the acceleration and therefore retards the recombination or the continuum-to-bound transition. The delay of $P^{(5)}(3\omega_0)$ at $E_{dc} = 0.4\ MV/cm$ further leads to a slight temporal shift of $|P(3\omega_0)|$ as it is determined by the interference between $P^{(3)}(3\omega_0)$ and $P^{(5)}(3\omega_0)$. At $E_{dc} = 0.7\ MV/cm$, the coherence is significantly reduced as exciton ionization dominates which converts excitons into unbound electrons and holes.

5.4 Conclusions

In this chapter, we numerically and theoretically investigate excitonic effects in the linear optical response and in THG from bilayer MoS_2. The linear absorption spectrum clearly reveals the Stark shifts of the exciton transition energies, hybridization of exciton states, and exciton ionization induced by a static in-plane field. Within the framework of the perturbative expansion of the SBE, the intraband excitation dominates over the interband excitation beyond the first order and gives rise to unique features of the THG in the

low intensity regime. The fourth-, fifth-, and higher-order intraband excitations representing the transitions between the continuum and exciton bound states are relevant for determining the efficiency of the third harmonic emission. We show that the fifth-order nonlinearity destructively interferes with the third-order excitation near the excitonic resonance and thus primarily leads to the lower yield of the THG compared to the perturbative third-order results. The interference is related to the **k**-dependence of the third- and fifth-order polarizations which is associated with the intraband excitations. Applying a static in-plane electric field characteristically modifies the **k**-resolved fourth- and higher-order nonlinearities and accordingly the interference with the third-order excitations near the excitonic resonance. An intensity-dependent enhancement of the THG yield with increasing static field amplitude is observed which arises from the shift from a destructive to a constructive interference between the third- and higher-odd-order excitations near the excitonic resonance. A sufficiently strong static in-plane field induces exciton ionization which is expected to lead to a decrease of the THG. Therefore, exciton ionization and the interference between lower- and higher-order nonlinearities compete which results in a non-monotonic dependence of the THG yield on the static field amplitude. Our results complement the understanding of the underlying process of excitonic harmonic generation and may potentially provide optical control over the efficiency of the excitonic response.

Conclusions 6

In this thesis, we theoretically studied the nonlinear optical response of bulk and two-dimensional semiconductor structures based on a full quantum-mechanical theory, i.e., the semiconductor Bloch equations and a semiclassical three-step model. We explored the harmonic generation in strong and weak excitation regimes where putting our emphasis on the nonperturbative subcycle field-driven dynamics of charge carriers and excitonic many-body effects.

High harmonic generation is a strong-field process and the coupled interband transitions and coherent intraband transport determine the high harmonic emission in solids. We investigated high harmonic generation induced by intense electric fields with frequencies much lower than the band gap in bulk MgO and ZnO materials and analyzed the features of the harmonic emission above the bandgap based on a semiclassical electron-hole recollision model. In our first theoretical and numerical investigation of high harmonic generation, Chapter 3, we focus on the experimental observations of the orientation-dependent high harmonic generation in MgO and provide a theoretical explanation for the origin of the anisotropy of the high harmonic emission. Within the semiclassical electron-hole recollision model which is proposed for the emission of the interband polarization, we revealed that the collisions of electrons and holes with neighboring atoms lead to an additional channel for the solid-state high harmonic generation besides the field-driven recombination of electron-hole pairs. We show that the electron and its associated hole experience backward- or forward-scattering upon the collisions with neighboring atoms when their wavelength approaches the atomic size. This can facilitate or impede the recombination of the electron with its left-behind hole and directly influences the efficiency of the high harmonic emission. Our results reveal that the electron/hole backward (forward) scattering occurs when the momentum-space trajectory passes Van Hove singularities (critical lines) in the band structure. Our findings build a mapping between the band structure and the harmonic spectrum and suggest a possibility to probe the characteristics of the electronic band structure via high harmonic spectroscopy.

In our second theoretical and numerical investigation of high harmonic generation, Chapter 4, we proposed a quantum trajectory model in which the quantum process of the tunneling ionization is included based on a complex saddle-point analysis. We provide a picture of tunneling ionization in the process of solid-state HHG where the properties of electrons and holes at the tunnel exit manifesting the adiabaticity of the tunneling are important for the subsequent classical evolution and the harmonic emission. According to the Keldysh theory, the adiabaticity of the tunneling ionization depends on the laser parameters, i.e., peak field amplitude and frequency, and the bandgap of the materials. Our results show that for high harmonic emission from ZnO under a strong excitation, adiabatic tunneling

occurs in which the initial velocities are nearly zero and the initial displacement between the electron and hole is close to the ratio between the bandgap and the Bloch energy. Under weaker excitation, nonzero initial velocities and a reduced initial displacement arising from nonadiabatic tunneling are revealed. This quantum trajectory analysis allows for precisely predicting the real-time high harmonic emission in ZnO. Furthermore, we demonstrate that the high harmonic interferometry enables us to establish a link between the experimental measurements of real-time high harmonic emission and the tunneling characters. Our findings provide fundamental insights into the nonadiabatic tunneling dynamics in solids and have direct implications for measuring optical tunneling in solid-state systems on the attosecond time scale.

In the last part of this thesis, Chapter 5, we focus on excitonic effects in third harmonic generation from bilayer MoS_2 arising from the strong Coulomb interaction in a rather weak excitation regime. Based on a perturbative expansion of semiconductor Bloch equations, we highlight the importance of intraband excitations in connecting the continuum and bound exciton states and the influence of a static field on the excitonic third harmonic generation. With increasing optical field amplitude, the fifth-order excitation representing the continuum-to-exciton transition increasingly contributes to the third harmonic generation via destructive interference with the third-order contribution. Applying a static in-plane field characteristically modifies the $\mathbf{k}$-resolved fourth- and fifth-order excitations and consequently shifts the interference towards a more constructive one near the excitonic resonance, leading to an increase of the third harmonic generation. At the same time, static field induced exciton ionization occurs and dominantly reduces the excitonic third harmonic generation for higher static fields. Our results indicate that even higher-order nonlinearities could influence the behavior of the excitonic third harmonic generation at higher optical intensities.

The results presented in this thesis offer fundamental insights into the microscopic processes that govern harmonic generation in solid-state systems. Our predictive theoretical work complements the basis of probing material properties and ultrafast atomic-scale dynamics using spectroscopy of solid-state systems. Further advancing our understanding of the coherent light-matter interaction is of great importance for the future light-driven manipulation of material properties.

Bibliography 7

[1] R. W. Boyd, *Nonlinear Optics*, 3rd ed. (Academic Press, San Diego, 2008).

[2] U. Keller, Recent developments in compact ultrafast lasers, Nature **424**, 831–838 (2003).

[3] F. W. Wise, Femtosecond fiber lasers based on dissipative processes for nonlinear microscopy, IEEE Journal of Selected Topics in Quantum Electronics **18**, 1412–1421 (2012).

[4] M. Chergui, M. Beye, S. Mukamel, C. Svetina, and C. Masciovecchio, Progress and prospects in nonlinear extreme-ultraviolet and X-ray optics and spectroscopy, Nature Reviews Physics **5**, 578–596 (2023).

[5] E. Fresch, F. V. A. Camargo, Q. Shen, C. C. Bellora, T. Pullerits, G. S. Engel, G. Cerullo, and E. Collini, Two-dimensional electronic spectroscopy, Nature Reviews Methods Primers **3**, 84 (2023).

[6] P. J. Campagnola and L. M. Loew, Second-harmonic imaging microscopy for visualizing biomolecular arrays in cells, tissues and organisms, Nature Biotechnology **21**, 1356–1360 (2003).

[7] X.-B. Bian and A. D. Bandrauk, Attosecond time-resolved imaging of molecular structure by photoelectron holography, Physical Review Letters **108**, 263003 (2012).

[8] P. Peng, C. Marceau, and D. M. Villeneuve, Attosecond imaging of molecules using high harmonic spectroscopy, Nature Reviews Physics **1**, 144–155 (2023).

[9] P. A. Franken, A. E. Hill, C. W. Peters, and G. Weinreich, Generation of optical harmonics, Physical Review Letters **7**, 118 (1961).

[10] J. A. Armstrong, N. Bloembergen, J. Ducuing, and P. S. Pershan, Interactions between light waves in a nonlinear dielectric, Physical Review **127**, 1918 (1962).

[11] G. H. C. New and J. F. Ward, Optical third-harmonic generation in gases, Physical Review Letters **19**, 556 (1967).

[12] T. H. Maiman, Stimulated optical radiation in Ruby, Nature Photonics **187**, 493–494 (1960).

[13] M. Wegener, *Extreme nonlinear optics* (Springer, Berlin, Heidelberg, 2005).

[14] M. Chini, K. Zhao, and Z. Chang, The generation, characterization and applications of broadband isolated attosecond pulses, Nature Photonics **8**, 178–186 (2014).

[15] D. Castelvecchi and K. Sanderson, Physicists who built ultrafast 'attosecond' lasers win Nobel Prize, Nature **622**, 225–227 (2023).

[16] A. McPherson, G. Gibson, H. Jara, U. Johann, T. S. Luk, I. A. McIntyre, K. Boyer, and C. K. Rhodes, Studies of multiphoton production of vacuum-ultraviolet radiation in the rare gases, Journal of the Optical Society of America B **4**, 595–601 (1987).

[17] X. F. Li, A. L'Huillier, M. Ferray, L. A. Lompré, and G. Mainfray, Multiple-harmonic generation in rare gases at high laser intensity, Physical Review A **39**, 5751 (1989).

[18] K. Midorikawa, Progress on table-top isolated attosecond light sources, Nature Photonics **16**, 267–278 (2022).

[19] P. B. Corkum and F. Krausz, Attosecond science, Nature Physics **3**, 381–387 (2007).

[20] T. Popmintchev, M.-C. Chen, P. Arpin, M. M. Murnane, and H. C. Kapteyn, The attosecond nonlinear optics of bright coherent X-ray generation, Nature Photonics **4**, 822–832 (2010).

[21] P. B. Corkum, Plasma perspective on strong field multiphoton ionization, Physical Review Letters **71**, 1994 (1993).

[22] P. B. Corkum, Recollision physics, Reviews of Modern Physics **64**, 36–41 (2011).

[23] K. J. Schafer, B. Yang, L. F. DiMauro, and K. C. Kulander, Above threshold ionization beyond the high harmonic cutoff, Physical Review Letters **70**, 1599 (1993).

[24] S. Ghimire, A. D. DiChiara, E. Sistrunk, P. Agostini, L. F. DiMauro, and D. A. Reis, Observation of high-order harmonic generation in a bulk crystal, Nature Physics **7**, 138–141 (2011).

[25] O. Schubert, M. Hohenleutner, F. Langer, B. Urbanek, C. Lange, U. Huttner, D. Golde, T. Meier, M. Kira, S. W. Koch, and R. Huber, Sub-cycle control of terahertz high-harmonic generation by dynamical Bloch oscillations, Nature Photonics **8**, 119–123 (2014).

[26] F. Langer, M. Hohenleutner, C. P. Schmid, C. Poellmann, P. Nagler, T. Korn, C. Schöller, M. S. Sherwin, U. Huttner, J. T. Steiner, S. W. Koch, M. Kira, and R. Huber, Lightwave-driven quasiparticle collisions on a subcycle timescale, Nature **533**, 225–229 (2016).

[27] Y. S. You, Y. Yin, Y. Wu, A. Chew, X. Ren, F. Zhuang, S. Gholam-Mirzaei, M. Chini, Z. Chang, and S. Ghimire, High-harmonic generation in amorphous solids, Nature Communications **8**, 724 (2017).

[28] G. Vampa, T. J. Hammond, N. Thiré, B. E. Schmidt, F. Légaré, C. R. McDonald, T. Brabec, and P. B. Corkum, Linking high harmonics from gases and solids, Nature **522**, 462–464 (2015).

[29] S. Han, H. Kim, Y. W. Kim, Y.-J. Kim, S. Kim, I.-Y. Park, and S.-W. Kim, High-harmonic generation by field enhanced femtosecond pulses in metal-sapphire nanostructure, Nature Communication **7**, 13105 (2016).

[30] T. T. Luu, M. Garg, S. Y. Kruchinin, A. Moulet, M. T. Hassan, and E. Goulielmakis, Extreme ultraviolet high-harmonic spectroscopy of solids, Nature **521**, 498–502 (2015).

[31] Á. Jiménez-Galán, C. Bossaer, G. Ernotte, A. M. Parks, R. E. F. Silva, D. M. Villeneuve, A. Staudte, T. Brabec, A. Luican-Mayer, and G. Vampa, Orbital perspective on high-harmonic generation from solids, Nature **14**, 8421 (2023).

[32] F. Langer, M. Hohenleutner, U. Huttner, S. W. Koch, M. Kira, and R. Huber, Symmetry-controlled temporal structure of high-harmonic carrier fields from a bulk crystal, Nature Photonics **11**, 227–231 (2017).

[33] S. Han, L. Ortmann, H. Kim, Y. W. Kim, T. Oka, A. Chacon, B. Doran, M. Ciappina, M. Lewenstein, S.-W. Kim, S. Kim, and A. S. Landsman, Extraction of higher-order nonlinear electronic response in solids using high harmonic generation, Nature Communications **10**, 3272 (2019).

[34] P. Jürgens, B. Liewehr, B. Kruse, C. Peltz, D. Engel, A. Husakou, T. Witting, M. Ivanov, M. J. J. Vrakking, T. Fennel, and A. Mermillod-Blondin, Origin of strong-field-induced low-order harmonic generation in amorphous quartz, Nature Physics **16**, 1035–1039 (2020).

[35] H. Liu, Y. Li, Y. S. You, S. Ghimire, T. F. Heinz, and D. A. Reis, High-harmonic generation from an atomically thin semiconductor, Nature Physics **13**, 262–265 (2017).

[36] N. Yoshikawa, T. Tamaya, and K. Tanaka, High-harmonic generation in graphene enhanced by elliptically polarized light excitation, Science **356**, 736–738 (2017).

[37] H. Liu, C. Guo, G. Vampa, J. L. Zhang, T. Sarmiento, M. Xiao, P. H. Bucksbaum, J. Vukovic, S. Fan, and D. A. Reis, Enhanced high-harmonic generation from an all-dielectric metasurface, Nature Physics **14**, 1006–1010 (2018).

[38] M. Sivis, M. Taucer, G. Vampa, K. Johnston Johnston, A. Staudte, A. Y. Naumov, D. M. Villeneuve, C. Ropers, and P. B. Corkum, Tailored semiconductors for high-harmonic optoelectronics, Science **357**, 303–306 (2017).

[39] G. Vampa, B. G. Ghamsari, S. Siadat Mousavi, T. J. Hammond, A. Olivieri, E. Lisicka-Skrek, A. Y. Naumov, D. M. Villeneuve, A. Staudte, P. Berini, and P. B. Corkum, Plasmon-enhanced high-harmonic generation from silicon, Nature Physics **13**, 659–662 (2017).

[40] G. Vampa, S. Vasilyev, H. Liu, M. Mirov, P. H. Bucksbaum, and D. A. Reis, Characterization of high-harmonic emission from ZnO up to 11 eV pumped with a Cr:ZnS high-repetition-rate source, Optics Letters **44**, 259–262 (2019).

[41] M. Garg, M. Zhan, T. T. Luu, H. Lakhotia, T. Klostermann, A. Guggenmos, and E. Goulielmakis, Multi-petahertz electronic metrology, Nature **538**, 359–363 (2016).

[42] S. Ghimire and D. A. Reis, High-harmonic generation from solids, Nature Physics **15**, 10–16 (2019).

[43] E. Goulielmakis and T. Brabec, High harmonic generation in condensed matter, Nat. Photon. **16**, 411–421 (2022).

[44] C. Heide, Y. Kobayashi, S. R. U. Haque, and S. Ghimire, Ultrafast high-harmonic spectroscopy of solids, Nature **20**, 1546–1557 (2024).

[45] G. Vampa, T. J. Hammond, N. Thiré, B. E. Schmidt, F. Légaré, C. R. McDonald, T. Brabec, D. D. Klug, and P. B. Corkum, All-optical reconstruction of crystal band structure, Physical Review Letters **115**, 193603 (2015).

[46] M. Hohenleutner, F. Langer, O. Schubert, M. Knorr, U. Huttner, S. W. Koch, M. Kira, and R. Huber, Real-time observation of interfering crystal electrons in high-harmonic generation, Nature **523**, 572–575 (2015).

[47] H. Lakhotia, H. Y. Kim, M. Zhan, S. Hu, S. Meng, and E. Goulielmakis, Laser picoscopy of valence electrons in solids, Nature **583**, 55–59 (2020).

[48] T. T. Luu and H. J. Wörner, Measurement of the Berry curvature of solids using high-harmonic spectroscopy, Nature Communications **9**, 916 (2018).

[49] J. Alcal*à*, U. Bhattacharya, J. Biegert, M. Ciappina, U. Elu, T. Grass, P. T. Grochowski, M. Lewenstein, A. Palau, T. P. H. Sidiropoulos, T. Steinle, and T. Igor, High-harmonic spectroscopy of quantum phase transitions in a high-Tc superconductor, Proc. Natl Acad. Sci. USA **119**, e2207766119 (2022).

[50] A. J. Uzan-Narovlansky, L. Faeyrman, G. G. Brown, S. Shames, V. Narovlansky, J. Xiao, T. Arusi-Parpar, O. Kneller, B. D. Bruner, O. Smirnova, R. E. F. Silva, B. Yan, Á. Jiménez-Galán, M. Ivanov, and N. Dudovich, Observation of interband Berry phase in laser-driven crystals, Nature **626**, 66–71 (2024).

[51] M. Wu, S. Ghimire, D. A. Reis, K. J. Schafer, and M. B. Gaarde, High-harmonic generation from Bloch electrons in solids, Physical Review A **91**, 043839 (2015).

[52] Z. Guan, X.-X. Zhou, and X.-B. Bian, High-order-harmonic generation from periodic potentials driven by few-cycle laser pulses, Physical Review A **93**, 033852 (2016).

[53] N. Tancogne-Dejean, O. D. Mücke, F. X. Kärtner, and A. Rubio, Impact of the electronic band structure in high-harmonic generation spectra of solids, Physical Review Letters **118**, 087403 (2016).

[54] D. Bauer and K. K. Hansen, High-harmonic generation in solids with and without topological edge states, Physical Review Letters **120**, 177401 (2018).

[55] D. Golde, T. Meier, and S. W. Koch, High harmonics generated in semiconductor nanostructures by the coupled dynamics of optical inter- and intraband excitations, Physical Review B **77**, 075330 (2008).

[56] G. Vampa, C. R. McDonald, G. Orlando, D. D. Klug, P. B. Corkum, and T. Brabec, Theoretical analysis of highharmonic generation in solids, Physical Review Letters **113**, 073901 (2014).

[57] T. Higuchi, M. I. Stockman, and P. Hommelhoff, Strong-field perspective on high-harmonic radiation from bulk solids, Physical Review Letters **113**, 143902 (2014).

[58] E. N. Osika, A. Chacón, L. Ortmann, N. Suárez, J. A. Pérez-Hernández, B. Szafran, M. F. Ciappina, F. Sols, A. S. Landsman, and M. Lewenstein, Wannier-Bloch approach to localization in high-harmonics generation in solids, Physical Review X **7**, 021017 (2017).

[59] F. Catoire, H. Bachau, Z. Wang, C. Blaga, P. Agostini, and L. F. DiMauro, Wannier representation of intraband high-order harmonic generation, Physical Review Letters **121**, 143902 (2018).

[60] A. M. Parks, G. Ernotte, A. Thorpe, C. R. McDonald, P. B. Corkum, M. Taucer, and T. Brabec, Wannier quasiclassical approach to high harmonic generation in semiconductors, Optica **7**, 1764–1772 (2020).

[61] G. Vampa, C. McDonals, R. G. Orlando, P. B. Corkum, and T. Brabec, Semiclassical analysis of high harmonic generation in bulk crystals, Physical Review B **91**, 064302 (2015).

[62] K. F. Mak, C. Lee, J. Hone, J. Shan, and T. F. Heinz, Atomically thin MoS_2: A new direct-gap semiconductor, Physical Review Letters **105**, 136805 (2010).

[63] K. He, N. Kumar, L. Zhao, Z. Wang, K. F. Mak, H. Zhao, and J. Shan, Tightly bound excitons in monolayer WSe_2, Physical Review Letters **113**, 026803 (2014).

[64] M. M. Ugeda, A. J. Bradley, S.-F. Shi, J. F. H. da, Y. Zhang, D. Y. Qiu, W. Ruan, S.-K. Mo, Z. Hussain, Z.-X. Shen, F. Wang, S. G. Louie, and M. F. Crommie, Giant bandgap renormalization and excitonic effects in a monolayer transition metal dichalcogenide semiconductor, Nature Materials **12**, 1091–1095 (2014).

[65] L. M. Malard, T. V. Alencar, A. P. M. Barboza, K. F. Mak, and A. M. d. Paula, Observation of intense second harmonic generation from MoS_2 atomic crystals, Physical Review B **87**, 201401 (2013).

[66] G. Wang, X. Marie, I. Gerber, T. Amand, D. Lagarde, L. Bouet, M. Vidal, A. Balocchi, and B. Urbaszek, Giant enhancement of the optical second-harmonic emission of WSe_2 monolayers by laser excitation at exciton resonances, Physical Review Letters **114**, 097403 (2015).

[67] J. Zhang, W. Zhao, P. Yu, G. Yang, and Z. Liu, Second harmonic generation in 2D layered materials, 2D Materials **7**, 042002 (2020).

[68] C. Qian, V. Villafane, P. Soubelet, P. Ji, A. V. Stier, and J. J. Finley, Probing dark excitons in monolayer MoS_2 by nonlinear two-photon spectroscopy, Physical Review Letters **133**, 086902 (2024).

[69] N. Yoshikawa, K. Nagai, K. Uchida, Y. Takaguchi, S. Sasaki, Y. Miyata, and K. Tanaka, Interband resonant high-harmonic generation by valley polarized electron-hole pairs, Nature Communications **10**, 3709 (2019).

[70] A. Trautmann, R. Zuo, G. Wang, W.-R. Hannes, S. Yang, L. H. Thong, C. Ngo, J. T. Steiner, M. Ciappina, M. Reichelt, H. T. Duc, X. Song, W. Yang, and T. Meier, Microscopic simulations of high harmonic generation from semiconductors, Proc. SPIE **11999**, 1199909 (2022).

[71] J. Hader, J. Neuhaus, J. V. Moloney, and S. W. Koch, Coulomb enhancement of high harmonic generation in monolayer transition metal dichalcogenides, Optics Letters **48**, 2094–2097 (2023).

[72] V. C. Lee, L. Yue, M. B. Gaarde, Y. Chan, and D. Y. Qiu, Many-body enhancement of high-harmonic generation in monolayer MoS_2, Nature Communications **15**, 6228 (2024).

[73] H. Haug and S. W. Koch, *Quantum Theory of the Optical and Electronic Properties of Semiconductors*, 5th ed. (World Scientific, Singapore, 2009).

[74] U. Huttner, M. Kira, and S. W. Koch, Ultrahigh off-resonant field effects in semiconductors, Laser Photonics Reviews **11**, 1700049 (2017).

[75] M. Kira and K. S. W., Many-body correlations and excitonic effects in semiconductor spectroscopy, Progress in Quantum Electronics **30**, 155–296 (2006).

[76] H. Liu, J. Zhao, Y.-X. Huang, X. Feng, C. Xiao, W. Wu, S. Lai, W.-B. Gao, and S. A. Yang, Berry connection polarizability tensor and third-order Hall effect, Physical Review B **105**, 045118 (2022).

[77] L. Yue and M. B. Gaarde, Structure gauges and laser gauges for the semiconductor Bloch equations in high-order harmonic generation in solids, Physical Review A **101**, 053411 (2020).

[78] A. M. Parks, J. V. Moloney, and T. Brabec, Gauge invariant formulation of the semiconductor Bloch equations, Physical Review Letters **131**, 236902 (2023).

[79] K. S. Virk and J. E. Sipe, Semiconductor optics in length gauge: A general numerical approach, Physical Review B **76**, 035213 (2007).

[80] L. H. Thong, C. Ngo, H. T. Duc, X. Song, and T. Meier, Microscopic analysis of high harmonic generation in semiconductors with degenerate bands, Physical Review B **103**, 085201 (2021).

[81] P. Földi, Gauge invariance and interpretation of interband and intraband processes in high-order harmonic generation from bulk solids, Physical Review B **96**, 035112 (2017).

[82] D. Vanderbilt, *Berry phase in electronic structure theory: electric polarization, orbital magnetization and topological insulators* (Cambridge University Press, Cambridge, 2018).

[83] J. Li, X. Zhang, S. Fu, Y. Feng, B. Hu, and H. Du, Phase invariance of the semiconductor Bloch equations, Physical Review A **100**, 043404 (2019).

[84] C. Ngo, S. Priyadarshi, H. T. Duc, M. Bieler, and T. Meier, Excitonic anomalous currents in semiconductor quantum wells, Physical Review B **108**, 165302 (2023).

[85] N. Marzari, A. A. Mostofi, J. R. Yates, I. Souza, and D. Vanderbilt, Maximally localized Wannier functions: Theory and applications, Reviews of Modern Physics **84**, 1419 (2011).

[86] S. Y. Kruchinin, F. Krausz, and V. S. Yakovlev, Strong-field phenomena in periodic systems, Review of Modern Physics **90**, 021002 (2018).

[87] A. J. Uzan, G. Orenstein, Á. Jiménez-Galán, C. McDonald, R. E. F. Silva, B. D. Bruner, N. D. Klimkin, V. Blanchet, T. Arusi-Parpar, M. Krüger, A. N. Rubtsov, O. Smirnova, M. Ivanov, B. Yan, T. Brabec, and N. Dudovich, Attosecond spectral singularities in solid-state high-harmonic generation, Nature Photonics **14**, 183–187 (2020).

[88] G. Ndabashimiye, S. Ghimire, M. Wu, D. A. Browne, K. J. Schafer, M. B. Gaarde, and D. A. Rei, Solid-state harmonics beyond the atomic limit, Nature **534**, 520–523 (2016).

[89] M. Wu, D. A. Browne, K. J. Schafer, and M. B. Gaarde, Multilevel perspective on high-order harmonic generation in solids, Physical Review A **94**, 063403 (2016).

[90] T. Ikemachi, Y. Shinohara, T. Sato, J. Yumoto, M. Kuwata-Gonokami, and K. L. Ishikawa, Trajectory analysis of high-order-harmonic generation from periodic crystals, Physical Review A **95**, 043416 (2017).

[91] L. Yue and M. B. Gaarde, Imperfect recollisions in high harmonic generation in solids, Physical Review B **124**, 153204 (2020).

[92] Y. S. You, D. A. Reis, and S. Ghimire, Anisotropic high harmonic generation in bulk crystals, Nature Physics **13**, 345–349 (2017).

[93] N. Tancogne-Dejean, O. D. Mücke, F. X. Kärtner, and A. Rubio, Ellipticity dependence of high-harmonic generation in solids originating from coupled intraband and interband dynamics, Nature Communications **8**, 745 (2017).

[94] C. Heide, Y. Kobayashi, D. R. Baykusheva, D. Jain, J. A. Sobota, M. Hashimoto, P. S. Kirchmann, S. Oh, T. F. Heinz, D. A. Reis, and S. Ghimire, Probing topological phase transitions using high-harmonic generation, Nature **16**, 620–624 (2022).

[95] T. J. Hammond, G. G. Brown, K. T. Kim, D. M. Villeneuve, and P. B. Corkum, Attosecond pulses measured from the attosecond lighthouse, Nature Photonics **10**, 171–175 (2016).

[96] J. Li, J. Lu, A. Chew, S. Han, J. Li, Y. Wu, H. Wang, S. Ghimire, and Z. Chang, Attosecond science based on high harmonic generation from gases and solids, Nature Communications **11**, 2748 (2020).

[97] S. W. Koch, M. Kira, G. Khitrova, and H. M. Gibbs, Semiconductor excitons in new light, Nature Materials **5**, 523–531 (2006).

[98] A. Chernikov, T. C. Berkelbach, H. M. Hill, A. Rigosi, Y. Li, B. Aslan, D. R. Reichman, M. S. Hybertsen, and T. F. Heinz, Exciton binding energy and nonhydrogenic Rydberg series in monolayer WS_2, Physical Review Letters **113**, 076802 (2014).

[99] G. Wang, A. Chernikov, M. M. Glazov, T. F. Heinz, X. Marie, T. Amand, and B. Urbaszek, Colloquium: Excitons in atomically thin transition metal dichalcogenides, Reviews of Modern Physics **90**, 021001 (2018).

[100] Z. Ye, T. Cao, K. O'Brien, H. Zhu, X. Yin, Y. Wang, S. G. Louie, and X. Zhang, Probing excitonic dark states in single-layer tungsten disulphide, Nature **513**, 214–218 (2014).

[101] D. Erben, A. Steinhoff, C. Gies, G. Schönhoff, T. O. Wehling, and F. Jahnke, Excitation-induced transition to indirect band gaps in atomically thin transition-metal dichalcogenide semiconductors, Physical Review B **98**, 035434 (2018).

[102] Q. H. Wang, K. Kalantar-Zadeh, A. Kis, J. N. Coleman, and M. S. Strano, Electronics and optoelectronics of two-dimensional transition metal dichalcogenides, Nature Nanotechnology **7**, 699–712 (2012).

[103] F. Xia, H. Wang, D. Xiao, M. Dubey, and A. Ramasubramaniam, Two-dimensional material nanophotonics, Nature Photonics **8**, 899–907 (2014).

[104] K. F. Mak, K. He, J. Shan, and T. F. Heinz, Control of valley polarization in monolayer MoS_2 by optical helicity, Nature Nanotechnology **7**, 494–498 (2012).

[105] T. LaMountain, J. Nelson, E. J. Lenferink, S. H. Amsterdam, A. A. Murthy, H. Zeng, T. J. Marks, V. P. Dravid, M. C. Hersam, and N. P. Stern, Valley-selective optical Stark effect of exciton-polaritons in a monolayer semiconductor, Nature Communications **12**, 4530 (2021).

[106] D. Xiao, G.-B. Liu, W. Feng, X. Xu, and W. Yao, Coupled spin and valley physics in monolayers of MoS_2 and other group-VI dichalcogenides, Physical Review Letters **108**, 196802 (2012).

[107] J. Lee, K. F. Mak, and J. Shan, Electrical control of the valley Hall effect in bilayer MoS_2 transistors, Nature Nanotechnology **11**, 421–425 (2016).

[108] N. Lundt, L. Dusanowski, E. Sedov, P. Stepanov, M. M. Glazov, S. Klembt, M. Klaas, J. Beierlein, Y. Qin, S. Tongay, M. Richard, A. V. Kavokin, S. Höfling, and C. Schneider, Optical valley Hall effect for highly valley-coherent exciton-polaritons in an atomically thin semiconductor, Nature Nanotechnology **14**, 770–775 (2019).

[109] S. Manzeli, D. Ovchinnikov, D. Pasquier, O. V. Yazyev, and A. Kis, 2D transition metal dichalcogenides, Nature Reviews Materials **2**, 17033 (2017).

[110] K. F. Mak, D. Xiao, and J. Shan, Light-valley interactions in 2D semiconductors, Nature Photonics **12**, 451–460 (2018).

[111] X. Chen, Z. Lian, Y. Meng, L. Ma, and S.-F. Shi, Excitonic complexes in two-dimensional transition metal dichalcogenides, Nature Communication **14**, 8233 (2023).

[112] N. Nagaosa, J. Sinova, S. Onoda, A. H. MacDonald, and N. P. Ong, Anomalous Hall effect, Reviews of Modern Physics **82**, 1539 (2010).

[113] O. Neufeld, D. Ayuso, P. Decleva, M. Y. Ivanov, O. Smirnova, and O. Cohen, Ultrasensitive chiral spectroscopy by dynamical symmetry breaking in high harmonic generation, Physical Review X **9**, 031002 (2019).

[114] A. J. Uzan-Narovlansky, G. Orenstein, S. Shames, M. E. Tzur, O. Kneller, B. D. Bruner, T. Arusi-Parpar, O. Cohen, and N. Dudovich, Revealing the interplay between strong field selection rules and crystal symmetries, Physical Review Letters **131**, 223802 (2023).

[115] T. T. Luu and H. J. Wörner, Observing broken inversion symmetry in solids using two-color high-order harmonic spectroscopy, Physical Review A **98**, 041802 (2018).

[116] A. J. Uzan-Narovlansky, Á. Jiménez-Galán, G. Orenstein, R. E. F. Silva, T. Arusi-Parpar, S. Shames, B. D. Bruner, B. Yan, O. Smirnova, M. Ivanov, and N. Dudovich, Observation of light-driven band structure via multiband high-harmonic spectroscopy, Nature Photonics **16**, 428–432 (2022).

[117] F. Sekiguchi, M. Sakamoto, K. Nakagawa, H. Tahara, S. A. Sato, H. Hirori, and Y. Kanemitsu, Enhancing high harmonic generation in GaAs by elliptically polarized light excitation, Physical Review B **108**, 205201 (2023).

[118] Y. Sanari, T. Otobe, Y. Kanemitsu, and H. Hirori, Modifying angular and polarization selection rules of high-order harmonics by controlling electron trajectories in k-space, Nature Communications **11**, 3069 (2020).

[119] R. Zuo, A. Trautmann, G. Wang, W.-R. Hannes, S. Yang, X. Song, T. Meier, M. Ciappina, T. D. Huynh, and W. Yang, Neighboring atom collisions in solid-state high harmonic generation, Ultrafast Science **2021**, 9861923 (2021).

[120] G. Vampa and T. Brabec, Merge of high harmonic generation from gases and solids and its implications for attosecond science, J. Phys. B: At. Mol. Opt. Phys. **50**, 083001 (2017).

[121] M. Lewenstein, P. Balcou, M. Y. Ivanov, A. L'Huillier, and P. B. Corkum, Theory of high-harmonic generation by low-frequency laser fields, Physical Review A **49**, 2117 (1994).

[122] A. Nayak, M. Dumergue, S. Kühn, S. Mondal, T. Csizmadia, N. Harshitha, M. Füle, M. U. Kahaly, B. Farkas, B. Major, V. Szaszkó-Bogár, P. Földi, S. Majorosi, N. Tsatrafyllis, E. Skantzakis, L. Neoričić, M. Shirozhan, G. Vampa, K. Varjú, S. Paraskevas Tzallas, Giuseppe, D. Charalambidis, and S. Kahaly, Saddle point approaches in strong field physics and generation of attosecond pulses, Physics Reports **833**, 1–52 (2019).

[123] O. Pedatzur, G. Orenstein, V. Serbinenko, H. Soifer, B. D. Bruner, A. J. Uzan, D. S. Brambila, A. G. Harvey, L. Torlina, F. Morales, O. Smirnova, and N. Dudovich, Attosecond tunnelling interferometry, Nature Physics **11**, 815–819 (2015).

[124] G. Vampa, J. Lu, Y. S. You, D. R. Baykusheva, M. Wu, H. Liu, K. J. Schafer, M. B. Gaarde, D. A. Reis, and S. Ghimire, Attosecond synchronization of extremely ultraviolet high harmonic from crystals, J. Physics. B: At. Mol. Opt. Phys. **53**, 144003 (2020).

[125] O. Kneller, D. Azoury, Y. Federman, M. Krüger, A. J. Uzan, G. Orenstein, B. D. Bruner, O. Smirnova, S. Patchkovskii, M. Ivanov, and N. Dudovich, A look under the tunnelling barrier via attosecond-gated interferometry, Nature Photonics **16**, 304–310 (2022).

[126] `http://elk.sourceforge.net/`.

[127] X. Chai, X. Ropagnol, S. M. Raeis-Zadeh, M. Reid, S. Safavi-Naeini, and T. Ozaki, Subcycle terahertz nonlinear optics, Physical Review Letters **121**, 143901 (2018).

[128] M. T. Hassan, T. T. Luu, A. Moulet, O. Raskazovskaya, P. Zhokhov, M. Garg, N. Karpowicz, A. M. Zheltikov, V. Pervak, F. Krausz, and E. Goulielmakis, Optical attosecond pulses and tracking the nonlinear response of bound electrons, Nature **530**, 66–70 (2016).

[129] H. Liang, P. Krogen, Z. Wang, H. Park, T. Kroh, K. Zawilski, P. Schunemann, J. Moses, L. F. DiMauro, F. X. Kärtner, and K.-H. Hong, High-energy mid-infrared sub-cycle pulse synthesis from a parametric amplifier, Nature Communications **8**, 141 (2017).

[130] *Real-time evolution of the trajectory starting at* $t = -0.13T_0$ *for* $\theta = 0°$ *in MgO (Supplementary Movie 1)*, `https://spj.science.org/doi/10.34133/2021/9861923#supplementary-materials`.

[131] L. V. Hove, The occurrence of singularities in the elastic frequency distribution of a crystal, Physical Review **89**, 1189–1193 (1953).

[132] D. Brust, J. C. Phillips, and F. Bassani, Critical points and ultraviolet reflectivity of semiconductors, Physical Review Letters **9**, 94–97 (1962).

[133] *Real-time evolution of the trajectory starting at* $t = 0.13T_0$ *for* $\theta = 27°$ *in MgO (Supplementary Movie 5)*, https://spj.science.org/doi/10.34133/2021/9861923#supplementary-materials.

[134] *Real-time evolution of the trajectory starting at* $t = -0.18T_0$ *for* $\theta = 45°$ *in MgO (Supplementary Movie 2)*, https://spj.science.org/doi/10.34133/2021/9861923#supplementary-materials.

[135] *Real-time evolution of the trajectory starting at* $t = 0.13T_0$ *for* $\theta = 0°$ *in MgO (Supplementary Movie 3)*, https://spj.science.org/doi/10.34133/2021/9861923#supplementary-materials.

[136] *Real-time evolution of the trajectory starting at* $t = -0.046T_0$ *for the laser polarization along* $\Gamma - M$ *in ZnO (Supplementary Movie 4)*, https://spj.science.org/doi/10.34133/2021/9861923#supplementary-materials.

[137] *Real-time evolution of the trajectory starting at* $t = 0.015T_0$ *when driven by an elliptically polarized laser field with* $\varepsilon = 0.65$ *in MgO (Supplementary Movie 6)*, https://spj.science.org/doi/10.34133/2021/9861923#supplementary-materials.

[138] *Real-time evolution of the trajectory starting at* $t = -0.105T_0$ *when driven by an circularly polarized laser field in MgO (Supplementary Movie 7)*, https://spj.science.org/doi/10.34133/2021/9861923#supplementary-materials.

[139] M. Hentschel, R. Kienberger, C. Spielmann, G. A. Reider, N. Milosevic, T. Brabec, P. Corkum, U. Heinzmann, M. Drescher, and F. Krausz, Attosecond metrology, Nature **414**, 509–513 (2001).

[140] M. Meckel, D. Comtois, D. Zeidler, A. Staudte, D. Pavii, H. C. Bandulet, H. Pépin, J. C. Kieffer, R. Dörner, D. M. Villeneuve, and P. B. Corkum, Laser-induced electron tunneling and diffraction, Science **320**, 1478–1482 (2008).

[141] Y. Huismans, A. Rouzée, A. Gijsbertsen, J. H. Jungmann, A. S. Smolkowska, P. S. W. M. Logman, F. Lépine, C. Cauchy, S. Zamith, T. Marchenko, J. M. Bakker, G. Berden, B. Redlich, A. F. G. v. d. Meer, H. G. Muller, W. Vermin, K. J. Schafer, M. Spanner, M. Y. Ivanov, O. Smirnova, D. Bauer, S. V. Popruzhenko, and M. J. J. Vrakking, Time-resolved holography with photoelectron waves, Science **331**, 61–64 (2011).

[142] O. Smirnova, Y. Mairesse, S. Patchkovskii, N. Dudovich, D. Villeneuve, P. Corkum, and M. Y. Ivanov, High harmonic interferometry of multi-electron dynamics in molecules, Nature **460**, 972–977 (2009).

[143] F. Krausz and M. Ivanov, Attosecond physics, Reviews of Modern Physics **81**, 163–234 (2009).

[144] M. Nisoli and G. Sansone, New frontiers in attosecond science, Progress in Quantum Electronics **33**, 17–59 (2009).

[145] D. Shafir, H. Soifer, B. D. Bruner, M. Dagan, Y. Mairesse, S. Patchkovskii, M. Y. Ivanov, O. Smirnova, and N. Dudovich, Resolving the time when an electron exits a tunnelling barrier, Nature **485**, 343–346 (2012).

[146] J. M. Dahlström, A. L'Huillier, and J. Mauritsson, Quantum mechanical approach to probing the birth of attosecond pulses using a two-colour field, J. Phys. B: At. Mol. Opt. Phys. **44**, 095602 (2011).

[147] J. Zhao and M. Lein, Determination of ionization and tunneling times in high-order harmonic generation, Physical Review Letters **111**, 043901 (2013).

[148] L. V. Keldysh, Ionization in the field of a strong electromagnetic wave, SOVIET PHYSICS JETP **20**, 1307–1314 (1965).

[149] C. Zhu and H. Nakamura, The two-state linear curve crossing problems revisited. II. Analytical approximations for the Stokes constant and scattering matrix: the Landau-Zener case, J. Chem. Phys. **97**, 8497–8514 (1992).

[150] G. L. Yudin and M. Y. Ivanov, Nonadiabatic tunnel ionization: Looking inside a laser cycle, Physical Review A **64**, 013409 (2001).

[151] O. Smirnova, M. Spanner, and M. Y. Ivanov, Coulomb and polarization effects in sub-cycle dynamics of strong-field ionization, J. Phys. B: At. Mol. Opt. Phys. **39**, S307 (2006).

[152] R. Zuo, X. Song, S. Ben, T. Meier, and W. Yang, Revealing the nonadiabatic tunneling dynamics in solid-state high harmonic generation, Physical Review Research **5**, L022040 (2023).

[153] D. Trabert, N. Anders, S. Brennecke, M. S. Schöffler, T. Jahnke, L. P. H. Schmidt, M. Kunitski, M. Lein, R. Dörner, and S. Eckart, Nonadiabatic strong field ionization of atomic hydrogen, Physical Review Letters **127**, 273201 (2021).

[154] J. Tong, X. Liu, W. Dong, W. Jiang, M. Zhu, Y. Xu, Z. Zuo, P. Lu, X. Gong, X. Song, W. Yang, and J. Wu, Probing resonant photoionization time delay by self-referenced molecular attoclock, Physical Review Letters **129**, 173201 (2022).

[155] M. Li, J.-W. Geng, M. Han, M.-M. Liu, L.-Y. Peng, Q. Gong, and Y. Liu, Subcycle nonadiabatic strong-field tunneling ionization, Physical Review A **93**, 013402 (2016).

[156] R. Boge, C. Cirelli, A. S. Landsman, S. Heuser, A. Ludwig, J. Maurer, M. Weger, L. Gallmann, and U. Keller, Probing nonadiabatic effects in strong-field tunnel ionization, Physical Review Letters **111**, 103003 (2013).

[157] M. Klaiber, K. Z. Hatsagortsyan, and K. C. H., Tunneling dynamics in multiphoton ionization and attoclock calibration, Physical Review Letters **114**, 083001 (2015).

[158] L. Li, P. Lan, X. Zhu, and P. Lu, Huygens-fresnel picture for high harmonic generation in solids, Physical Review Letters **127**, 223201 (2021).

[159] N. Dudovich, O. Smirnova, J. Levesque, Y. Mairesse, M. Y. Ivanov, D. M. Villeneuve, and P. B. Corkum, Measuring and controlling the birth of attosecond XUV pulses, Nature Physics **2**, 781–786 (2006).

[160] O. Smirnova and M. Y. Ivanov, *Multielectron high harmonic generation: Simple man on a complex plane, in attosecond and XUV physics* (Wiley, New York, 2014) Chap. 7, pp. 201–256.

[161] V. Gruson, L. Barreau, Á. Jiménez-Galan, F. Risoud, J. Caillat, A. Maquet, B. Carré, F. Lepetit, J.-F. Hergott, T. Ruchon, L. Argenti, R. Taïeb, F. Martén, and P. Salires, Attosecond dynamics through a Fano resonance: Monitoring the birth of a photoelectron, Science **354**, 734–738 (2016).

[162] A. Ciarrocchi, F. Tagarelli, A. Avsar, and A. Kis, Excitonic devices with van der waals heterostructures: valleytronics meets twistronics, Nature Reviews Materials **7**, 449–464 (2022).

[163] A. Manchon, H. C. Koo, J. Nitta, S. M. Frolov, and R. A. Duine, New perspectives for Rashba spin-orbit coupling, Nature Materials **14**, 871–882 (2015).

[164] X. Xu, W. Yao, D. Xiao, and T. F. Heinz, Spin and pseudospins in layered transition metal dichalcogenides, Nature Physics **10**, 343–350 (2014).

[165] R. Ribeiro-Palau, C. Zhang, K. Watanabe, T. Taniguchi, J. Hone, and C. R. Dean, Twistable electronics with dynamically rotatable heterostructures, Science **361**, 690–693 (2018).

[166] S. Chichibu, T. Azuhata, T. Sota, and S. Nakamura, Spontaneous emission of localized excitons in InGaN single and multiquantum well structures, Applied Physics Letters **69**, 4188–4190 (1996).

[167] D. Y. Qiu, F. H. d. Jornada, and S. G. Louie, Optical spectrum of MoS_2: Many-body effects and diversity of exciton states, Physical Review Letters **111**, 216805 (2013).

[168] H. M. Hill, A. F. Rigosi, C. Roquelet, A. Chernikov, T. C. Berkelbach, D. R. Reichman, M. S. Hybertsen, L. E. Brus, and T. F. Heinz, Observation of excitonic Rydberg states in monolayer MoS_2 and WS_2 by photoluminescence excitation spectroscopy, Nano Letters **15**, 2992–2997 (2015).

[169] X.-X. Zhang, T. Cao, Z. Lu, Y.-C. Lin, F. Zhang, Y. Wang, Z. Li, J. C. Hone, A. Joshua Robinson, D. Smirnov, S. G. Louie, and T. F. Heinz, Magnetic brightening and control of dark excitons in monolayer WSe_2, Nature Nanotechnology **12**, 883–888 (2017).

[170] S. Cha, J. H. Sung, S. Sim, J. Park, H. Heo, M.-H. Jo, and H. Choi, 1s-intraexcitonic dynamics in monolayer MoS_2 probed by ultrafast mid-infrared spectroscopy, Nature Communications **7**, 10768 (2016).

[171] C.-K. Yong, M. I. B. Utama, C. S. Ong, T. Cao, E. C. Regan, J. Horng, Y. Shen, H. Cai, K. Watanabe, T. Taniguchi, S. Tongay, H. Deng, A. Zettl, S. G. Louie, and F. Wang, Valley-dependent exciton fine structure and Autler-Townes doublets from Berry phases in monolayer $MoSe_2$, Nature Materials **18**, 1065–1070 (2019).

[172] B. Zaks, R. B. Liu, and S. Sherwin, Experimental observation of electron-hole recollisions, Nature **483**, 580–583 (2012).

[173] K. Uchida, T. Otobe, T. Mochizuki, C. Kim, M. Yoshita, K. Tanaka, H. Akiyama, L. N. Pfeiffer, K. W. West, and H. Hirori, Coherent detection of THz-induced sideband emission from excitons in the nonperturbative regime, Physical Review B **97**, 165122 (2018).

[174] J. Freudenstein, M. Borsch, M. Meierhofer, D. Afanasiev, C. P. Schmid, F. Sandner, M. Liebich, A. Girnghuber, M. Knorr, M. Kira, and R. Huber, Attosecond clocking of correlations between Bloch electrons, Nature **610**, 290–295 (2022).

[175] E. B. Molinero, B. Amorim, M. Malakhov, G. Cistaro, Á. Jiménez-Galán, A. Picón, P. San-José, M. Ivanov, and R. E. F. Silva, Subcycle dynamics of excitons under strong laser fields, Science Advances **10**, eadn6985 (2024).

[176] S. V. B. Jensen, L. B. Madsen, A. Rubio, and N. Tancogne-Dejean, High-harmonic spectroscopy of strongly bound excitons in solids, Physical Review A **109**, 063104 (2024).

[177] B. Zhu, K. Xiao, S. Yang, K. Watanabe, T. Taniguchi, and X. Cui, In-plane electric-field-induced orbital hybridization of excitonic states in monolayer WSe_2, Physical Review Letters **131**, 036901 (2023).

[178] L. D. Santis, M. E. Trusheim, K. C. Chen, and D. R. Englund, Investigation of the Stark effect on a centrosymmetric quantum emitter in diamond, Physical Review Letters **127**, 147402 (2021).

[179] T. G. Pedersen, Exciton Stark shift and electroabsorption in monolayer transition-metal dichalcogenides, Physical Review B **94**, 125424 (2016).

[180] H. C. Kamban and T. G. Pedersen, Efficient ionization of two-dimensional excitons by intense single-cycle terahertz pulses, Physical Review B **104**, 235305 (2021).

[181] M. Massicotte, F. Vialla, P. Schmidt, M. B. Lundeberg, S. Latini, S. Haastrup, M. Danovich, D. Davydovskaya, K. Watanabe, T. Taniguchi, V. I. Fal'ko, K. S. Thygesen, T. G. Pedersen, and F. H. Koppens, Dissociation of two-dimensional excitons in monolayer WSe_2, Nature Communications **9**, 1633 (2018).

[182] D. Brunne, M. Lafrentz, V. V. Pavlov, R. V. Pisarev, A. V. Rodina, D. R. Yakovlev, and M. Bayer, Electric field effect on optical harmonic generation at the exciton resonances in GaAs, Physical Review B **92**, 085202 (2015).

[183] F. Schlaepfer, M. Lucchini, S. A. Sato, M. Volkov, L. Kasmi, N. Hartmann, A. Rubio, L. Gallmann, and U. Keller, Attosecond optical-field-enhanced carrier injection into the GaAs conduction band, Nature Physics **14**, 560–564 (2018).

[184] K. Nakagawa, H. Hirori, S. A. Sato, H. Tahara, F. Sekiguchi, G. Yumoto, M. Saruyama, R. Sato, T. Teranishi, and Y. Kanemitsu, Size-controlled quantum dots reveal the impact of intraband transitions on high-order harmonic generation in solids, Nature Physics **18**, 874–878 (2022).

[185] R. Huber, B. A. Schmid, Y. R. Shen, D. S. Chemla, and R. A. Kaindl, Stimulated terahertz emission from intraexcitonic transitions in Cu_2O, Physical Review Letters **96**, 017402 (2006).

[186] G. Berghäuser, P. Steinleitner, P. Merkl, R. Huber, A. Knorr, and E. Malic, Mapping of the dark exciton landscape in transition metal dichalcogenides, Physical Review B **98**, 020301 (2018).

[187] S. C. Kuhn, A. Knorr, and M. Richter, All-optical approach to determine the spatial shape of nanoscale electron wave functions using intraband spectroscopy, Physical Review B **89**, 201414(R) (2014).

[188] S. C. Kuhn and M. Richter, Excitonic effects in intraband quantum dot spectroscopy: Formation of bound continuum excitons, Physical Review B **90**, 125308 (2014).

[189] C. Aversa and J. E. Sipe, Nonlinear optical susceptibilities of semiconductors: Results with a length-gauge analysis, Physical Review B **52**, 14636 (1995).

[190] W.-R. Hannes and T. Meier, Higher-order contributions and nonperturbative effects in the nondegenerate nonlinear optical absorption of semiconductors using a two-band model, Physical Review B **99**, 125301 (2019).

[191] A. Kormányos, V. Zólyomi, V. I. Fal'ko, and G. Burkard, Tunable Berry curvature and valley and spin Hall effect in bilayer MoS_2, Physical Review B **98**, 035408 (2018).

[192] Z. Gong, G.-B. Liu, H. Yu, D. Xiao, X. Cui, X. Xu, and W. Yao, Magnetoelectric effects and valley-controlled spin quantum gates in transition metal dichalcogenide bilayers, Nature Communications **4**, 2053 (2013).

[193] S. Wu, J. S. Ross, G.-B. Liu, G. Aivazian, A. Jones, Z. Fei, W. Zhu, D. Xiao, W. Yao, D. Cobden, and X. Xu, Magnetoelectric effects and valley-controlled spin quantum gates in transition metal dichalcogenide bilayers, Nature Physics **9**, 149–153 (2013).

[194] L. Meckbach, T. Stroucken, and S. W. Koch, Influence of the effective layer thickness on the ground-state and excitonic properties of transition-metal dichalcogenide systems, Physical Review B **97**, 035425 (2018).

[195] M. Selig, G. Berghäuser, A. Raja, P. Nagler, C. Schüller, T. F. Heinz, T. Korn, A. Chernikov, E. Malic, and A. Knorr, Excitonic linewidth and coherence lifetime in monolayer transition metal dichalcogenides, Nature Communications **7**, 13279 (2016).

[196] C. Trovatello, F. Katsch, N. J. Borys, M. Selig, K. Yao, R. Borrego-Varillas, F. Scotognella, I. Kriegel, A. Yan, A. Zettl, P. J. Schuck, A. Knorr, G. Cerullo, and S. D. Conte, The ultrafast onset of exciton formation in 2D semiconductors, Nature Communications **11**, 5277 (2020).

[197] P. Borlido, J. Schmidt, A. W. Huran, F. Tran, M. A. L. Marques, and S. Botti, Exchange-correlation functionals for band gaps of solids: benchmark, reparametrization and machine learning, npj Computational Materials **6**, 96 (2020).

[198] A. O'Hara, T. N. Nunley, A. B. Posadas, S. Zollner, and A. A. Demkov, Electronic and optical properties of NbO_2, Journal of Applied Physics **116**, 213705 (2014).

[199] P.-L. Ardelt, K. Gawarecki, K. Müller, A. M. Waeber, A. Bechtold, K. Oberhofer, J. M. Daniels, F. Klotz, M. Bichler, T. Kuhn, H. J. Krenner, P. Machnikowski, and J. J. Finley,

Coulomb mediated hybridization of excitons in coupled quantum dots, Physical Review Letters **116**, 077401 (2016).

[200] J. Stark, Observation of the separation of spectral lines by an electric field, Nature **92**, 401 (1913).

[201] D. M. Bishop, Polarizability and hyperpolarizability of atoms and ions, Physical Review Letters **6**, 129–146 (1999).

[202] L. S. R. Cavalcante, D. R. d. Costa, G. A. Farias, D. R. Reichmanand, and A. Chaves, Stark shift of excitons and trions in two-dimensional materials, Physical Review B **98**, 245309 (2018).

[203] B. Scharf, T. Frank, M. Gmitra, J. Fabian, I. Žutić, and V. Perebeinos, Excitonic Stark effect in MoS_2 monolayers, Physical Review B **94**, 245434 (2016).

[204] T. Y. Latychevskaia, A. Renn, and U. Wild, Higher-order Stark effect on single-molecules, Proc. SPIE **282**, 109–119 (2002).

[205] A. M. Fox, D. A. B. Miller, J. E. Cunningham, W. Y. Jan, C. Y. P. Chao, and S. L. Chuang, Suppression of the observation of stark ladders in optical measurements on superlattices by excitonic effects, Physical Review B **46**, 15365 (1992).

[206] N. Linder, Excitons in superlattices: absorption asymmetry, dimensionality transition, and exciton localization, Physical Review B **55**, 13664 (1996).

[207] A. Thorpe, N. Boroumand, A. M. Parks, E. Goulielmakis, and T. Brabec, High harmonic generation in solids: Real versus virtual transition channels, Physical Review B **107**, 075135 (2023).

[208] T. G. Pedersen, Intraband effects in excitonic second-harmonic generation, Physical Review B **92**, 235432 (2015).

[209] Y. Kobayashi, C. Heide, A. C. Johnson, V. Tiwari, F. Liu, D. A. Reis, T. F. Heinz, and S. Ghimire, Floquet engineering of strongly driven excitons in monolayer tungsten disulfide, Nature Physics **19**, 171–176 (2023).

Danksagung

In writing this thesis, I would like to express my gratitude to everybody who has supported me during my PhD study. Without their guidance and help, I cannot accomplish this PhD work.

First and foremost, I would like to thank my supervisor Prof. Dr. Torsten Meier, who allowed me to pursue a PhD with time spent on the Sonderforschungsbereich transregio142 A10 project. It was a great pleasure and luck for me to work here in an excellent team where I received invaluable advice and physical insights from my supervisor and my colleagues. I would also like to thank very much Prof. Dr. Torsten Meier for allowing me to visit an international school, conferences, and workshops, during which I have learned a lot from many excellent researchers.

I would like to thank Prof. Dr. Xiaohong Song and Prof. Dr. Weifeng Yang (Hainan University) for their consideration of my career, for providing me with opportunities to participate in international collaboration, and for guidance and support in research work.

I would like to thank my current and former colleagues, Dr. Shidong Yang, Guifang Wang, Dr. Alexander Trautmann, Cong Thanh Ngo, and Dr. Matthias Reichelt for teaching me programming skills, for helping me solve various numerical problems during my research work, and for sharing insightful ideas and collaborating to advance research work together. Besides, I would like to thank Dr. Hendrik Rose, who offered me lots of assistance beyond academics when I just came to Paderborn University.

Furthermore, I would like to thank Ms. Simone Lange, the group's secretary, for her kindness and constant support with administrative work, which made my work and life in Paderborn much smoother and easier.

I would like to thank my friends, Yeye Zhang, Xunqing Huo, Ying Pan, and Kaihong Luo for their support and encouragement in all the good and bad days.

Finally, I would like to thank my parents and my brother for supporting me to do anything I want with enough freedom.